N O T I C E

THIS DOCUMENT HAS BEEN REPRODUCED FROM MICROFICHE. ALTHOUGH IT IS RECOGNIZED THAT CERTAIN PORTIONS ARE ILLEGIBLE, IT IS BEING RELEASED IN THE INTEREST OF MAKING AVAILABLE AS MUCH INFORMATION AS POSSIBLE

NASA Contractor Report 163092

(NASA-CR-163092) SPACE SHUTTLE ORBITER FLOW VISUALIZATION STUDY (Northrop Corp.) 68 p HC A04/MF A01 CSCL 22B

N80-31438

Unclas
G3/16 17528

SPACE SHUTTLE ORBITER FLOW VISUALIZATION STUDY

Dale J. Lorincz

Contract NAS4-2616
February 1980

NASA

NASA Contractor Report 163092

SPACE SHUTTLE ORBITER FLOW VISUALIZATION STUDY

Dale J. Lorincz
Northrop Corporation
Hawthorne, California

ORIGINAL CONTAINS
COLOR ILLUSTRATIONS

Prepared for
Dryden Flight Research Center
under Contract NAS4-2616

National Aeronautics and
Space Administration

1980

CONTENTS

PAGE BLANK NOT FILMED

SPACE SHUTTLE ORBITER

FLOW VISUALIZATION STUDY

By Dale J. Lorincz
Northrop Corporation, Aircraft Group
Hawthorne, California

SUMMARY

Water tunnel studies have been performed to qualitatively define the flow field of the Space Shuttle Orbiter. Particular emphasis was placed on defining the vortex flows generated at subsonic speed during the final portion of atmospheric reentry. The flow visualization tests were conducted in the Northrop diagnostic water tunnel using a 0.01-scale model of the Orbiter. Flow visualization photographs were obtained over an angle-of-attack range to 40° and sideslip angles up to 10°.

The Orbiter model was investigated to determine, in detail, the vortex flow field development, vortex path, and vortex breakdown characteristics as a function of angle of attack at zero sideslip. Vortex flows were found to develop on the highly swept glove, on the wing, and on the upper surface of the fuselage. The mapping of these vortex flows was done to identify any aerodynamic asymmetries that might occur at zero sideslip. No significant asymmetries were observed in the water tunnel tests.

Additional tests were performed to determine the sensitivity of the upper surface vortex flow fields to variations in sideslip angle. The vortex formed on the glove remained very stable in position above the wing up through the 10° of sideslip tested. There was a change in the vortex lifts under sideslip due to effective changes in leading-edge sweep angles. Asymmetric flow separation occurred on the upper surface of the fuselage at small sideslip angles. The influence of vortex flow fields in sideslip on the lateral/directional characteristics of the Orbiter is discussed.

INTRODUCTION

The aerodynamic design of the Space Shuttle Orbiter was based on an extensive wind tunnel testing program and analysis effort. The recently completed Approach and Landing Tests (ALT) of the Orbiter were conducted to verify the subsonic aerodynamic performance predictions. Several areas of concern to NASA have been noted from the analysis of experimental data obtained from the tests in the various wind tunnel facilities and the recent ALT. These areas are the existence of regions of nonlinear aerodynamic characteristics, and cases of disagreement between data obtained in the various facilities. A flow visualization study was undertaken to investigate the possible aerodynamic sources of these irregularities.

The wing planform of the Shuttle Orbiter is a double-delta design. The main wing has a leading-edge sweep of 45° while the long, slender glove has a leading-edge sweep of 81° (Reference 1). The flow field around this wing planform and the Orbiter fuselage at moderate to high angles of attack consists of regions of separated, low-energy flow and concentrated vortex flows of high energy. From the results of past investigations (References 2, 3, and 4), it is known that this complex flow field can produce aerodynamic characteristics which are nonlinear in angle of attack and/or sideslip. A better understanding of the fluid flow phenomena present and their effects can be obtained through flow visualization.

Studies done at Northrop using a water tunnel have provided excellent visualization of vortex flows on wings and fuselage forebodies. The water tunnel has been used to qualitatively define the vortex flow fields on many aircraft configurations. Changes in angle of attack, sideslip, and model configuration can be made quickly and inexpensively using small scale models. The flow visualization results discussed in this report were obtained using a 0.01-scale model of the Space Shuttle Orbiter. All testing was done in the Northrop diagnostic water tunnel which has a test section of 0.41 by 0.61 m (16 by 24 in.)

The primary purpose of these tests was to define the vortex flow fields generated above the wing, the glove, and on the fuselage. The sensitivity of the vortex flows to changes in angle of attack and sideslip was determined. Wherever possible, the water tunnel results are compared to Rockwell wind tunnel model surface oil flow data and to NASA Ames 40 x 80-foot low-speed wind-tunnel data on a 0.36-scale Orbiter model.

SYMBOLS

b	wing span
C_L	lift coefficient
C_ℓ	rolling moment coefficient
C_{n_β}	directional stability coefficient (per degree)
C_Y	side force coefficient
FS	fuselage station
M_c	crossflow Mach number
M_∞	freestream Mach number
OMS	Orbital Maneuvering System
α	angle of attack
β	angle of sideslip

EXPERIMENTAL METHODS

Water Tunnel Facility

The Northrop diagnostic water tunnel is a closed return tunnel used for high quality flow visualization of complex three-dimensional flow fields. The water tunnel is shown schematically in Figure 1. The test section is 0.41 m (16 in.) by 0.61 m (24 in.) by 1.83 m (6 ft.) long and has walls made of transparent plexiglass. The test section is oriented in the vertical direction, which facilitates viewing the model from any angle. A model is shown installed in the test section in Figure 2. The model is accessed through the top of the tunnel by means of suspension cables connected to the model support system.

The model support system consists of a sting and sideslip arc which is capable of pitch angles from -10° to 70°, concurrent with a sideslip range of -20° to 20°. Either the pitch angle or the sideslip angle is fixed prior to the model installation. The remaining angle is then free to be manually adjusted from the side of the test section.

Test Procedure

The flow visualization in the water tunnel is obtained by injection of colored food dyes having the same density as water. The density of water is 800 times that of air, which gives the dye excellent light reflecting characteristics relative to using smoke in air. The dye is injected into the flow field through a remotely-controlled dye probe and through dye tubes internally or externally mounted to the model.

The water tunnel is nominally operated at a test section velocity of 0.1 meters/second which has been found to produce the best flow visualization results. This velocity corresponds to a Reynolds number of 1×10^5/meter. It has been shown empirically (References 5, 6, and 7) that vortex flows on thin, swept wings are properly modeled at this low Reynolds number. Surface flows at low angles of attack that are not vortex dominated can be more sensitive to Reynolds number effects.

For the case of a thick, swept wing having a blunt leading edge, such as the Space Shuttle Orbiter, the onset of boundary layer separation is a function of the Reynolds number. The rounded leading edge delays the boundary layer separation and the vortex formation to a higher angle of attack in flight with a turbulent boundary layer compared to in the water tunnel with laminar separation. At the higher Reynolds number, a vortex will form on a thick, swept wing but at a higher angle of attack. A wind tunnel test at low Reynolds number could give too large a vortex lift with the early laminar separation and early vortex formation.

MODEL DESCRIPTION

The water tunnel flow visualization studies were conducted with a 0.01-scale model of the Space Shuttle Orbiter. The model was supplied by NASA. A three-view drawing of the model is shown in Figure 3. The model configuration tested was with the landing gear up and all primary control surfaces at zero deflection. The rocket engine nozzles at the aft end of the fuselage were omitted from the model. These nozzles do not extend into the freestream. The orbital maneuvering system (OMS) pods were complete in detail as was the body flap on the lower aft end of the fuselage.

In order to visualize the flow field, the model was equipped with dye orifices. Great care was taken in locating the dye orifices to insure that the dye being injected would be entrained into the vortices. A remotely-controlled dye probe was used to survey the model to find the exact location for each orifice. The dye orfices were installed flush with the surface whenever possible. The dye lines running to the right and left orifices at the same fuselage station were supplied from a plenum within the model to insure a symmetrical dye flow rate.

A grid was layed out on the wings of the model to aid in documenting the path of the vortices and for measuring the location of the vortex breakdown. The grid begins at fuselage station 600 for the full-scale vehicle, which is just aft of the apex of the glove. The grid has divisions of 254 cm (100 in.) full scale or 2.54 cm (1 in.) apart on the model. A line was drawn in the chordwise direction on the model at 0.25 b (5.95 cm).

RESULTS AND DISCUSSION

The experimental results that were obtained consist of a set of photographs documenting the water tunnel flow visualization studies. Selected results are referred to in the text and are given at the end of this report. The water tunnel results are compared to the results of oil flow studies done by Rockwell International on a 0.0405-scale Orbiter model. Whenever possible, comparisons are made between the water tunnel flow visualization results and force and moment data obtained in the NASA Ames Research Center 40 x 80-foot wind tunnel using a 0.36-scale model.

Wing-Glove Flow Field Characteristics

The wing-glove flow field at zero sideslip is presented in Figure 4 with both plan and profile views. The dye orifices in the leading edges of the wing and glove are located such that the dye from them would be entrained into the vortices. At 0° angle of attack, however, the flow is fully attached on the upper surface. The dye being ejected at the apex of the glove is within the boundary layer and Figure 4(b) shows that the surface flow is in the streamwise direction, aft along the side of the fuselage. As the dye nears the OMS pods, it is deflected downward and onto the wing. This dye, being in the boundary layer, is at a lower velocity than flow above the surface and so undergoes a larger deflection.

As seen in Figure 4(a) at 2° angle of attack, the dye from the leading edge of the wing and glove moves in the chordwise direction but with some spanwise spreading. Beneath the dye coming from the leading edge there was a stronger spanwise flow near the wing trailing edge. This strong spanwise flow close to the surface of the wing is due to a thickening of the boundary layer over the aft portion of the wing. It is thought that this would not occur under flight conditions. The more chordwise flow direction of the dye coming from the leading edge is more representative of flight.

Also at 2° angle of attack, the dye being injected at the wing-glove intersection on the left side appears on the upper surface of the wing, while it remains

on the lower surface of the right wing. The locations of the dye orifices were checked and found to be symmetric. There apparently is a slight difference in model geometry between the right and left sides at the wing-glove intersection.

A vortex is first formed on the glove at 8° angle of attack. In the profile view, Figure 4 (b), it can be seen that the dye from the apex of the glove no longer flows along the side of the fuselage but is instead entrained into the vortex. A second pair of vortices begins to form above the wing and outboard of the glove vortices at 10° angle of attack. These vortices begin to roll up where the leading-edge sweep angle changes at the start of the glove-wing intersection. By 12° angle of attack, this vortex above the wing is well formed and is seen in the profile view, Figure 4 (b), to pass up and over the glove vortex.

The wing vortex exhibited increased rotational velocity with increasing angle of attack to 15°, but is still much weaker than the glove vortex. The wing vortex rides up and over the glove vortex but then drops below the height of the glove vortex. As the wing vortex begins to pass beneath the glove vortex, both vortices break down aft of the trailing edge of the wing. This wrapping of two vortices around each other was investigated in Reference 8. The wing and glove vortices are an example of two vortices of unequal circulation strength, same circulation direction, and with a vortex core separation distance small enough for interaction to occur. In this case, the two vortices will rotate about an axis that is located between the vortices and closer to the larger strength vortex.

With the increase in flow separation over the outer wing panel at 18°, the weaker wing vortex begins to merge with the glove vortex. The wing vortex continues to merge with the glove vortex at 20° angle of attack on the right wing of the Orbiter model but not on the left. On the left side the wing vortex follows a different path, closer to the wing leading edge. As was mentioned before, a difference between the right and left glove-wing intersections was found at 2° angle of attack. The formation and path of the wing vortex at the higher angles of attack is apparently sensitive to small differences in model geometry.

The breakdown of the glove vortex reaches the trailing edge of the wing at 20° angle of attack. By 25°, the burst point of the glove vortex has progressed inboard and forward onto the wing. The wing vortex is seen to be completely broken down at 30° angle of attack while the burst point of the glove vortex has reached the glove-wing intersection. A separated flow field exists

across the wing at 30°. Regions of reversed flow were seen within the turbulent wake behind the wing. With further increases in angle of attack, the burst point of the glove vortex continues forward above the glove itself. At 40° angle of attack, the highest angle tested, the burst point had not yet reached the apex of the glove.

Figure 5 presents the progression of the burst point of the glove vortex as a function of angle of attack. At 20° angle of attack, the burst point was above the trailing edge of the wing at Fuselage Station 1460 (FS 1460). The location of the vortex breakdown is measured in the profile view along a line normal to the surface. Note that the forward progression of the burst point is more gradual after FS 1000. This increase in the slope of the curve at 30° corresponds to the breakdown occurring above the more highly swept glove.

The influence of Reynolds number on the vortex breakdown position has been investigated at Northrop and by others. In the Northrop studies (Reference 5), the angle of attack at which vortex breakdown occurred at the trailing edge was observed on delta wings having leading-edge sweep angles of 55° to 85°. Figure 6, which is taken from Reference 5, shows that the results obtained in the Northrop water tunnels fall within the range of angles of attack observed by others. The data shown include results from other water tunnels as well as wind tunnels and covers the Reynolds number range of 10^4 to 10^6, based on root chord. Note that the variation in the data due to Reynods number is no greater than the variation associated with different facilities and different flow visualization techniques at the same Reynolds number. All of the data follow the same trend of increasing angle of attack for vortex breakdown at the trailing edge as the leading-edge sweep angle is increased.

The lift curve of the Orbiter is given in Figure 7. This curve was obtained from data on a 0.36-scale model tested in the NASA Ames 40 x 80-foot wind tunnel at a Reynolds number of 4 x 10^6/meter. As indicated in Figure 7, there is an increase in lift curve slope at 8° angle of attack. Below this angle of attack, the lift develops linearly, and the slope of the lift curve is constant. The development of nonlinear lift above 8° angle of attack is consistent with the formation of the glove vortex. A reduction in the lift curve slope begins above 20° angle of attack. This corresponds to the breakdown of the glove vortex passing the trailing edge of the wing and moving over the wing for angles of attack above 20°.

Wing-Glove Flow Field in Sideslip

The sensitivity of the wing-glove flow field to changes in angle of sideslip was first studied at 8° angle of attack as the angle of sideslip was varied from 0° to 10°. Photographs of the wing-glove flow field in sideslip at 8° angle of attack are presented in Figure 8. This is the angle of attack where the glove vortex was formed.

In a sideslip attitude, the leeward wing and glove have an effectively higher sweep angle. This higher sweep increases the axial velocity within the core of the glove vortex at the expense of the rotational velocity. Evidence of the increase in axial velocity can be seen in the leeward profile views of Figure 8(c). At zero sideslip, the dye injected at the apex of the glove spreads over the upper surface of the glove. As the sideslip angle is increased, this dye is pulled directly into the high velocity, low pressure core of the vortex.

At 8° angle of attack there is no evidence of the vortex which will form on the wing at higher angles of attack. A vortex has, however, formed on the more highly swept glove. The windward wing and glove are at an effectively lower sweep angle in sideslip. As the effective sweep is reduced on the windward side, the flow becomes attached on the windward glove. With the reduced leading-edge sweep, a higher angle of attack is required for the vortex to form.

At 15° angle of attack, the glove vortex on the leeward side, seen in Figure 9, undergoes changes in sideslip that are similar to those at 8°. On the leeward side the axial velocity within the core of the glove vortex increases relative to the rotational velocity which is seen to be reduced. This results in an increase in vortex stability. With its increased stability, the leeward glove vortex bursts further downstream in sideslip. The leeward wing vortex also becomes more stable in sideslip.

The leeward wing vortex shifts outboard with increasing sideslip. The windward wing vortex shifts inboard and merges with the glove vortex as the sideslip angle increases. Both the windward and leeward glove vortices are very stable in position with almost no observable shift due to sideslip. The Orbiter planform exhibits comparatively little vortex asymmetry in sideslip, especially when compared to the aircraft configurations shown in Figure 10.

The flow field on the windward wing and glove in sideslip at 15° angle of attack is very different from that seen at 8°. The windward glove vortex is now well defined in sideslip. On the windward side, the leading-edge sweep angle has been effectively reduced. This increases the strength of the glove vortex as seen in the increased rotational velocity. The velocity normal to the wing quarter chord is greater on the windward wing and less on the leeward side. This increases the lift on the windward side while reducing the lift on the leeward side. The windward wing is also at a higher angle of attack than the leeward because of the 3.5° of positive dihedral in the wing. This higher angle of attack in sideslip increases the vortex strength which increases the vortex lift on the windward wing. The increased lift on the windward wing contributes to a stable rolling moment in sideslip. Figure 11 shows the increased rolling moments due to sideslip generated at 15° angle of attack as compared to 8°. At the lower angles of attack, approximately half of the rolling moment in sideslip is due to the large vertical tail of the Orbiter. The side force produced by the vertical tail in sideslip acts through a vertical moment arm to produce a stable rolling moment.

The wing-glove flow field in sideslip at 20° angle of attack is presented in Figure 12. At this angle of attack, the burst point of the glove vortex is located at the wing trailing edge for zero sideslip conditions. Varying the sideslip angle changes the chordwise burst point of the vortices. For increasing sideslip, the leeward side, with its effective increase in leading-edge sweep, shows the burst point to move downstream, beyond the trailing edge. The lower effective sweep of the windward glove decreases the stability of the windward glove vortex causing it to burst above the wing. The breakdown of the windward vortex reduces the lift on that wing and causes a reduction in the stable rolling moment. Figure 11 shows that for sideslip angles greater than 6°, the stable rolling moment is less at 20° angle of attack than at 15°.

The glove vortices remain stable in location above the wing in sideslip at 20° angle of attack. At the highest slideslip angles tested there is more of a shift in position than was seen at 15°, but it is still small. For increasing sideslip, the leeward wing vortex becomes more stable and continues to interact with the glove vortex. The windward wing vortex is shifted closer to the strong glove vortex and merges with it. Figure 12 also shows plan views of the model for positive sideslip angles. These are presented because of the asymmetry, due to

model geometry, in the wing vortices at 20° angle of attack. For positive sideslip angles of 5° and higher, a stable, well defined vortex is formed at the left wing-glove intersection. At these sideslip angles, the left wing vortex closely resembles the vortex seen on the right wing under symmetric conditions.

Fuselage Flow Field Characteristics

The flow field of the fuselage of the Orbiter at zero sideslip is presented in both plan and profile views in Figure 13. The dye injection orifices in the fuselage are located on the lower surface of the fuselage nose, on the vertical side walls of the fuselage aft of the canopy, and just ahead of the OMS pods. At low angles of attack, the dye from the fuselage nose remains on the lower surface.

For small negative angles of attack, such as -2°, a vortex is formed in the corner formed by the upper fuselage and the front of the OMS pods. This vortex rolls up as the flow coming aft toward the pods is turned downward toward the upper surface of the fuselage. In the corner, the flow is turned back forward and upward, which completes the roll up of the vortex. A weak vortex is still formed ahead of the pods at 0° angle of attack. The profile view in Figure 13 shows that the vortex and the dye ahead of the pod is turned sharply downward toward the wing. The flow turns back to the freestream direction once it is beneath the pod. This flow does not reach the upper surface of the wing.

As the angle of attack is increased to positive values, the vortex is no longer formed ahead of the pod. A region of separated, reversed flow is seen ahead of the pods at 5° angle of attack. Also at 5°, the dye being injected on the lower surface of the forward fuselage has moved upward on to the upper surface of the left glove but not on the right. This flow asymmetry is due to either asymmetries in model geometry on the lower surface or to slight differences in the location of the dye injection orifices on the right and left sides of the lower surface. Within an additional 1° angle of attack, the dye had reached the upper surface of the glove on both sides.

Between 8° and 10° angle of attack, a pair of vortices begins to form on the upper fuselage. The boundary layer separates from the upper fuselage aft of the canopy and along the upper corner of the cargo bay doors. Figure 13

shows that at 10° angle of attack the region of separated flow beneath the fuselage vortex and ahead of the pod extends further forward on the upper surface. Figure 14 shows a close-up of the aft portion of the fuselage at 10° angle of attack. The flow reversal ahead of the pod is evident in the forward movement of the dye. The fuselage vortex impinges on the OMS pods and breaks down.

With further increases in angle of attack, the fuselage vortex increases in strength. This was evident from the vortex becoming better defined, more tightly rolled up, and from observed increases in the rotational velocity of the vortex. The fuselage vortex also begins to rise above the surface of the fuselage as the angle between the vortex and the fuselage increases. By 15° angle of attack, the fuselage vortex almost clears the OMS pods but still breaks down above them as shown in Figure 14. There is also increased unsteadiness in the flow ahead of the pods at 15° compared to the lower angles. At 20° angle of attack, the angle between the fuselage vortex and the surface has increased to where the vortices pass above the pods, as seen in Figures 13 and 14. The vortices continue downstream past the vertical tail before breaking down. The plan view in Figure 13 shows no asymmetries between the flow on the right and left sides at 20° angle of attack and zero sideslip.

Between 25° and 30° angle of attack, a change occurs in the flow upstream of the OMS pods. At 25° angle of attack. Figure 13, there is still the reversed flow that has been seen at the lower angles of attack. At 30°, however, the flow is spanwise and outboard ahead of the pods. As the angle of attack has been increased, the rotational velocity of the vortex and so its strength has continued to increase. The fuselage vortices generate a pressure gradient on the upper surface which accelerates the boundary layer in the lateral direction. Also at 30° angle of attack, the dye from ahead of the pods moves outboard onto the wing, as well as moving aft. From Figure 5 it is known that at 30° the burst point of the glove vortex has reached the glove-wing intersection. Separated flow is present over the aft portion of the wing.

The fuselage vortices break down just aft of the pods at 35° angle of attack. At 40° angle of attack, the burst point of the fuselage vortex has moved to above the pods. The plan view in Figure 13 shows a slight asymmetry in the forebody vortices. The left vortex is shifted outboard and breaks down further forward. There is no apparent displacement in height, only the shift in lateral position.

The most notable flow asymmetry seen on the orbiter fuselage was in the 5° to 6° angle of attack range. It is attributed to lack of symmetry in the model or in the location of the dye orifices. At higher angles of attack, the flow is very symmetric. There was considerable unsteadiness in the flow ahead of the OMS pods, and hence the right and left sides are generally similar but not identical. Figure 15 presents the side forces at zero sideslip measured on a 0.36-scale Orbiter model in the NASA Ames 40 x 80-foot wind tunnel at a Mach number of 0.18. Up through 26° angle of attack, the measured asymmetries are of a very low level. This level of asymmetry should present no problems for control of the Orbiter.

At 40° angle of attack, an asymmetry was observed in the fuselage vortices. The Orbiter will be flown at 40° angle of attack but only under conditions of low dynamic pressures and high Mach number during entry (Reference 1). Experimental studies (References 9 and 10) have shown that in supersonic flow fields the side forces produced by asymmetric vortices are reduced to almost zero. A symmetric pattern of shock waves develops which inhibits the influence of the asymmetric vortices from reaching the body.

A comparison is shown in Figure 16 of the surface flow on Orbiter models in the Rockwell NAAL low-speed tunnel and in the Northrop water tunnel. Both the 0.0405-scale wind tunnel model and the 0.01-scale water tunnel model were tested at 18° angle of attack and zero sideslip. The oil flow visualization was obtained at a Reynolds number of approximately 6×10^6/meter. The water tunnel flow visualization was performed at a Reynolds number of 0.1×10^6/meter. The direction of the surface flow across the fuselage of the water tunnel model in Figure 16 is at an upward angle greater than the freestream direction. This can also be seen in Figure 13 at 12° and 15°. After leaving the flat side wall of the fuselage, the flow angle becomes progressively less until it runs parallel to the upper corner of the cargo bay doors. The flow on the forward part of the fuselage separates from the surface at this upper corner and forms the feeding sheet to the vortex.

The wind tunnel oil flow shows the same flow directions on the fuselage as shown by the dye used in the water tunnel. Near the upper corner of the fuselage, the crossflow angle reduces progressively to where the boundary layer streamlines converge and run parallel to the fuselage. This boundary layer flow

pattern is also very similar to the flow field associated with the boundary layer separation and the formation of vortices on a cone as described in Reference 11.

On the upper surface of the fuselage, the oil flow indicates an aft and outboard flow direction. This outward movement of the boundary layer flow is due to the pressure gradient caused by the fuselage vortices. The vortices inducing the outboard flow on the fuselage are seen in the water tunnel photographs. The strong downward movement of the flow ahead of the OMS pods is seen in both the oil flow and water tunnel visualization. The deflection of the flow begins well ahead of the pod. Between the pod and the upper surface of the wing, the flow turns aft and parallel to the wing on both models.

Fuselage Flow Field in Sideslip

Photographs of the fuselage flow field in sideslip at 8° angle of attack are presented in Figure 17. This is the angle of attack where the glove vortex was formed. Flow separation does occur at the upper corners of the fuselage, but a vortex has not yet formed there.

At 0° sideslip, the area of flow separation in front of the OMS pods is symmetrical. For sideslip angles as small as 1°, differences between the separated regions in front of the right and left OMS pods can be seen. On the windward side the dye begins to pass over the top of the pod. The region of separated flow ahead of the windward pod extends further forward with increasing sideslip. By only 3° of sideslip, the separated region on the windward side of the upper surface has grown quite large.

The flow field on the aft portion of the fuselage is shown in Figure 18 at 8° angle of attack and -5° sideslip. The dye being injected ahead of the windward pod is spreading forward in a region of reversed flow. As the flow moves forward, it rises up off the surface, and is then blown aft where it passes over the top of the pod. This turbulent region extends to well above the pod. On the leeward side, at 5° sideslip the separation region has not moved forward. There is a shift in the direction of the flow ahead of the leeward pod as indicated by the dye. It no longer all moves outboard away from the centerline, as some is now drawn toward the center of the model.

The asymmetries become more pronounced for increasing sideslip angles. The separated region on the windward side extends further inboard with increasing sideslip. By 7° of sideslip, most of the dye in front of the leeward pod is being drawn toward the separated, reversed flow region. The flow angle on the leeward side is no longer away from the center of the fuselage as was the case at low angles of sideslip when the sidewash resulted from the sideslip angle. This local "adverse" sidewash at the higher angles of sideslip is often found on swept-wing aircraft when the flow has separated on the windward wing (Reference 2).

The fuselage flow field in sideslip at 15° angle of attack is presented in Figure 19. At this angle of attack and zero sideslip, the region of separated flow ahead of the OMS pods extends further forward than at 8° angle of attack. A vortex pair has now formed above the fuselage but the vortices are weak and not tightly rolled up. With increasing sideslip, both vortices are shifted away from the windward side. The effective sweep angle of the fuselage on the windward side is being reduced. This will reduce the stability of the windward vortex causing it to break down as the sideslip angle increases. With only 3° of sideslip, the windward fuselage vortex breaks down.

The flow separation ahead of the windward pod increases as the sideslip angle increases. The reversed flow does not extend as far forward on the upper surface of the fuselage as it did at 8° angle of attack. The flow is, however, more turbulent at the higher angle of attack. The adverse sidewash ahead of the vertical tail is delayed until higher sideslip angles. The flow ahead of the leeward pod is not drawn toward the fuselage centerline until around 5° of sideslip.

The fuselage vortices are better defined at 20° angle of attack as can be seen in Figure 20. At zero sideslip, they pass above the OMS pods without breaking down. For small sideslip angles, the windward vortex once again breaks down. The leeward fuselage vortex has increased stability and shifts toward the leeward edge of the fuselage. The asymmetry between the right and left fuselage vortices at -5° sideslip is shown in Figure 21. The adverse sidewash ahead of the vertical tail is not seen at 20° in Figure 20 until above 5° of sideslip. The reversed flow region in front of the windward pod does not extend as far forward as at 15°. The turbulent, separated region on the aft portion of the upper fuselage does extend to a greater height above the upper surface at 20° than at 15°.

More of the vertical tail becomes immersed in the low-velocity wake off the fuselage.

In the profile views of the leeward side of Figure 20 (c), it should be noted that the dye from the lower surface of the forward fuselage shows the flow to pass smoothly around the lower corner of the fuselage. The crossflow is then upward across the flat sided fuselage without separating until it reaches the upper fuselage corner. This occurs at 20° angle of attack for all sideslip angles tested from 0° to 10°.

Figure 22 illustrates the effects of Reynolds number and of testing in different facilities on the directional stability of the Orbiter. For angles of attack up to 16°, the Orbiter exhibits strong stability and there is little difference between the results at different Reynolds number. Near 20° angle of attack, there is a large variation in the directional stability measured in the different tests. The results from the tests in the 40 x 80-foot wind tunnel are at the highest Reynolds number and show a loss of directional stability.

In Reference 1 it was stated that the changes in directional stability with increasing Reynolds number were due to changes in the crossflow on the forward fuselage. The changes in the crossflow were thought to be similar to those that occur on a square-shaped cylinder with rounded corners at 90° angle of attack as described in Reference 12. For this square cylinder, the flow separates on the leeward side at subcritical Reynolds number but remains attached at supercritical Reynolds number. For the supercritical Reynolds number case, the side force on the cylinder is negative at positive sideslip, which acts through a moment arm to the center of gravity to produce a negative yawing moment and so reduce the directional stability. The reduction of directional stability of the Orbiter is hence attributed to the elimination of the flow separation on the leeward side of the nose with increased crossflow Reynolds number.

Recent experiments have shown that a different crossflow exists on the square cylinder at lower angles of attack that are closer to the 20° of the Orbiter. It was found, Reference 13, that at the lower angles of attack, the flow on the leeward side can remain attached even at low Reynolds number. At the lower angles of attack, vortices are formed above the upper surface whereas at 90° only a large separated wake region was present. The vortices organize the

highly disorganized wake that occurs near 90° and so effectively vents the separated region. This causes a more favorable pressure gradient which delays separation and results in attached flow on the leeward side at low Reynolds number.

In the water tunnel, vortices were seen to have formed above the fuselage of the Orbiter and in sideslip there was a vortex above the leeward side. Also, the dye from the forward fuselage showed the boundary layer flow to be attached on the leeward side until the second or upper corner was reached. If the boundary layer remained attached on leeward side in the water tunnel at its low Reynolds number, then it should do so in any of the wind tunnel tests which were run at higher Reynolds numbers. Some other mechanism must be responsible for the loss of directional stability measured in the 40 x 80-foot wind tunnel. Some decrease in directional stability can be expected with increasing angle of attack as the lower portion of the vertical tail becomes immersed in the low-velocity wake and adverse sidewash above the fuselage.

Effect of Mach Number

The tests reported on here were conducted in water, which is a nearly incompressible fluid. The compressibility effects found in air for high Mach number flight can not be properly modeled in the water tunnel. The presence of shock waves and shock induced separation can not be studied in a water tunnel. Keeping these limitations in mind, there are certain areas where the water tunnel can be used to gain understanding of separated flow fields on the leeward surface of vehicles in supersonic flight.

Both the leading-edge vortices formed on delta wings and the vortices formed on bodies of revolution at angle of attack have been found to still be present for freestream, supersonic Mach numbers. The leading-edge vortex flow will occur for subsonic leading edges where the Mach number components normal to the leading edges are less than one (References 14 and 15). Tests run on a delta wing of 75° leading-edge sweep in a water tunnel and at $M_\infty = 1.95$ found a similar vortex structure and showed good agreement in the position of the core of the vortex above the wing (Reference 16). Compressibility will begin to reduce the variations of velocity and pressure across the wing vortex core, making the core more diffuse. Also, the pronounced suction peak beneath the vortex

will be reduced as the Mach number is increased (Reference 17). When the component of the Mach number that is normal to the leading edge is greater than one, the leeside flow changes to a separation bubble with embedded shocks and finally shock induced separation (References 1, 14, and 15).

The location of the core of the vortex on bodies of revolution was measured in wind tunnels at both subsonic and supersonic freestream Mach numbers, as reported in Reference 18. The vortex core position was also measured in a water tunnel and compared to the higher Mach number results. The vertical position of the vortex measured in the water tunnel was in good agreement with the results from the wind tunnel tests for both subsonic and supersonic Mach numbers. The lateral position of the body vortex in the water tunnel was outboard of most of the vortex core locations measured in the wind tunnels.

The effect of Mach number on the vortices formed on bodies of revolution is dependent on the crossflow Mach number, $M_c = M_\infty \sin\alpha$. Changes in the vortex flow field due to compressibility begin at M_c of about 0.6 (Reference 19). Increases in the crossflow Mach number have been found to reduce the vortex-induced side force on bodies at zero sideslip. No significant vortex-induced side forces have been observed on cones or ogive cylinders at supersonic crossflow Mach numbers (References 9 and 10). A symmetric pattern of shock waves developes which inhibits the influence of the asymmetric vortices from reaching any side area of the body. In addition, the experimental results in Reference 20 indicate that compressibility effects will reduce the concentrated circulation in a body vortex, making it more diffuse. An asymmetry was observed in the Orbiter fuselage vortices at 40° angle of attack in the water tunnel. At this angle of attack during the reentry, the Mach number is high and the dynamic pressure is low. Under such conditions, no vortex-induced loads on the side of the fuselage should occur.

Despite the reduction in vortex-induced side force at zero sideslip with increasing Mach number, the fuselage vortices are still present to very high Mach numbers and can still influence the flow field near the OMS pods and the vertical tail. On blunt-nosed bodies, vortices were generated on the body aft of a bow shock and a shock wave in the nose region (Reference 21). Oil flow studies done at hypersonic speeds on the leeward side of delta-wing orbiter configurations (References 22 and 23) show the presence of a fuselage vortex pair, as was seen on the Orbiter in the water tunnel. The leeward fuselage vortex

flow was shown to be sensitive to sideslip angle, as seen in the asymmetry that occurred in the oil flow in sideslip.

In the water tunnel, the flow on the fuselage in sideslip was seen to be reversed ahead of the windward OMS pod. With increasing slideslip angle, a local adverse sidewash occurs ahead of the vertical tail. With increasing angle of attack, more of the vertical tail becomes immersed in the separated flow from the aft portion of the fuselage. Evidence of this kind of flow field at supersonic Mach numbers was found on an early delta-wing orbiter configuration with a single, centerline vertical tail as reported in Reference 23. On this configuration at $M_\infty = 2.5$ the incremental side force generated in sidelip by the speed brake in the vertical tail was found to reverse sign for angles of attack above 20°. A loss of vertical tail effectiveness at high angles of attack can be expected due to the wing-body shielding of the tail from the freestream conditions. The shielding effect, however, should not cause a reversal of the direction of the speed brake side force. The shielding can allow the local adverse sidewash to become dominant over the freestream conditions. The incremental speed brake side force was no longer reversed at the higher Mach number of 4.6, but it was reduced to near zero at high angles at attack.

CONCLUDING REMARKS

Flow visualization studies were conducted in the Northrop diagnostic water tunnel to provide qualitative definition of the vortex flow fields occurring on the Space Shuttle Orbiter at subsonic speeds. Details of the wing, glove, and fuselage vortex flow fields were obtained for up to 40° angle of attack and 10° sideslip. The documentation covered the vortex flow field development, vortex path, and vortex breakdown characteristics. Under zero sideslip conditions, no significant aerodynamic asymmetries were observed. The influence of the vortex flow fields in sideslip on the lateral/directional characteristics of the Orbiter was determined. The water tunnel flow visualization study aided in understanding the results of a wind tunnel oil flow study. A summary of the flow visualization results is given below and conclusions are made where appropriate:

1. A strong, stable vortex was formed on the highly swept glove. A weaker wing vortex was formed at the glove-wing intersection. No significant aerodynamic asymmetries were observed in the flow field of the glove and wing at zero sideslip. The wing vortex at the higher angles of attack was, however, sensitive to small geometric model asymmetries in the curved glove-wing intersection. Good agreement was found between the changes in the slope of the lift curve of the Orbiter and the formation and breakdown of the glove vortex above the wing.

2. The glove vortices remained very stable in position above the wing to 10° of sideslip. The weaker wing vortices shifted away from the windward side and interacted with the stronger glove vortices. The difference in lift between the wings in sideslip, with the windward wing having increased lift, contributes to a stable rolling moment. The asymmetric breakdown of the vortices in sideslip at around 20° angle of attack causes a reduction in roll stability.

3. A vortex pair formed on the upper fuselage surface aft of the canopy by 10°. A turbulent flow region was found on the upper fuselage surface in front of the OMS pods. No significant aerodynamic asymmetries were found in the fuselage flow field at zero sideslip.

4. The windward fuselage vortex broke down at low sideslip angles. At the same time, a large reversed flow region was found on the windward

side, ahead of the OMS pod. An adverse sidewash was found ahead of the vertical tail at the larger sideslip angles. The immersion of the lower portion of the vertical tail into the low-velocity wake and adverse sidewash above the fuselage in sideslip will decrease the directional stability.

5. The crossflow over the forward fuselage was found to remain attached on the leeward side of the fuselage in sideslip at 20° angle of attack. The vortex formed above the fuselage provides a favorable pressure gradient and so delays separation on the leeward side.

6. The fuselage vortex pair will become more diffuse with increasing crossflow Mach number. The formation of shock waves will limit the side area on which the fuselage vortices can act.

REFERENCES

1. Bornemann, W.E. and Surber, T.E., "Aerodynamics Design of the Space Shuttle Orbiter," High Angle of Attack Aerodynamics, AGARD CP-247-11, 1979.

2. Chambers, J.R. and Grafton, S.B., "Aerodynamic Characteristics of Airplanes at High Angles of Attack," NASA TM 74097, 1977.

3. Headley, J.W., "Analysis of Wind Tunnel Data Pertaining to High Angle-of-Attack Aerodynamics," AFFDL TR-78-94, Volume I, 1978.

4. Lorincz, D.J., "Water Tunnel Flow Visualization Study of the F-15," NASA CR-144878, 1978.

5. Erickson, G., "Water Tunnel Flow Visualization: Insight Into Complex Three-Dimensional Flow Fields," AIAA Paper 79-1530, 1979.

6. Poisson-Quinton, Ph. and Werlé, H., "Water Tunnel Visualization of Vortex Flow," Astronautics and Aeronautics, June 1967.

7. Werlé, H., "Hydrodynamic Flow Visualization," Annual Review of Fluid Mechanics, Volume 5, pp. 361-382, 1973.

8. Groenenboom, J. and Ievalts, J., "Wing Vortex Visualization and Vortex Interface Patterns," AIAA Paper 77-309, 1977.

9. Keener, E.R., Chapman, G.T., and Kruse, R.L., "Effects of Mach Number and Afterbody Length on Onset of Asymmetric Forces on Bodies at Zero Sideslip and High Angles of Attack," AIAA Paper 76-66, 1976.

10. Jorgensen, L.H. and Nelson, E.R., "Experimental Aerodynamic Characteristics for a Cylindrical Body of Revolution with Various Noses at Angles of Attack from 0° to 58° and Mach Numbers from 0.6 to 2.0," NASA TM X-3128, 1974.

11. Peake, D.J., Owen, F.K. and Higuchi, H., "Symmetrical and Asymmetrical Separations About a Yawed Cone," High Angle of Attack Aerodynamics, AGARD CP-247-16, 1979.

12. Polhamus, E.C., "Effect of Flow Incidence and Reynolds Number on Low Speed Aerodynamic Characteristics of Several Noncircular Cylinders with Application to Directional Stability and Spinning," NASA TR R-29, 1959.

13. Clarkson, M.H., Malcolm, G.N., and Chapman, G.T., "A Subsonic, High-Angle-of-Attack Flow Investigation at Several Reynolds Numbers," AIAA Journal, Vol. 16, No. 1, January 1978, pp. 53-60.

14. Szodruch, J. and Ganzer, U., "On the Lee-Side Flow Over Delta Wings at High Angle of Attack," High Angle of Attack Aerodynamics, AGARD CP-247-21, 1979.

15. Stanbrook, A. and Squire, L. C., "Possible Types of Flow at Swept Leading Edges," Aeronautical Quarterly, Vol. 15, 1960, pp. 72-82.

16. Monnerie, B. and Werlé, H., "Etude de l'Ecoulement Supersonique et Hypersonique Autour d'une Aile Elancee en Incidence," Hypersonic Boundary Layers & Flow Fields, AGARD CP-30-23, 1968.

17. Kiichemann, D., "The Aerodynamic Design of Aircraft," Pergamon Press Ltd., 1978, pp. 367-374.

18 Deane, J. R., "Wind and Water Tunnel Investigations of the Interaction of Body Vortices and the Wing Panels of a Missile Configuration," High Angle of Attack Aerodynamics. AGARD CP-247-21, 1979.

18. Thomson, K. D. and Morrison, D. F., "The Spacing, Position, and Strength of Vortices in the Wake of Slender Cylindrical Bodies at Large Incidence," J. Fluid Mech., Vol. 50, 1971, pp. 751-783.

20. Oberkampf, W. L. and Bartel, T. J., "Symmetric Body Vortex Wake Characteristics in Supersonic Flow," AIAA Paper 78-1337, 1978.

21. Hall, I. M., Rogers, E. W. E., and Davies, B. M., "Experiments with Inclined Blunt-Nosed Bodies at M = 2.45," ARC R&M 3128, 1957.

22. Hefner, J. N., "Lee-Surface Heating and Flow Phenomena on Space Shuttle Orbiters at Large Angles of Attack and Hypersonic Speeds," NASA TN D-7088, 1972.

23. Reding, J. P. and Ericsson, L. E., "Review of Delta Wing Space Shuttle Vehicle Dynamics," Space Shuttle Aerothermodynamics Technology Conference, Vol. III, NASA TM X-2508, 1972, pp. 861-931.

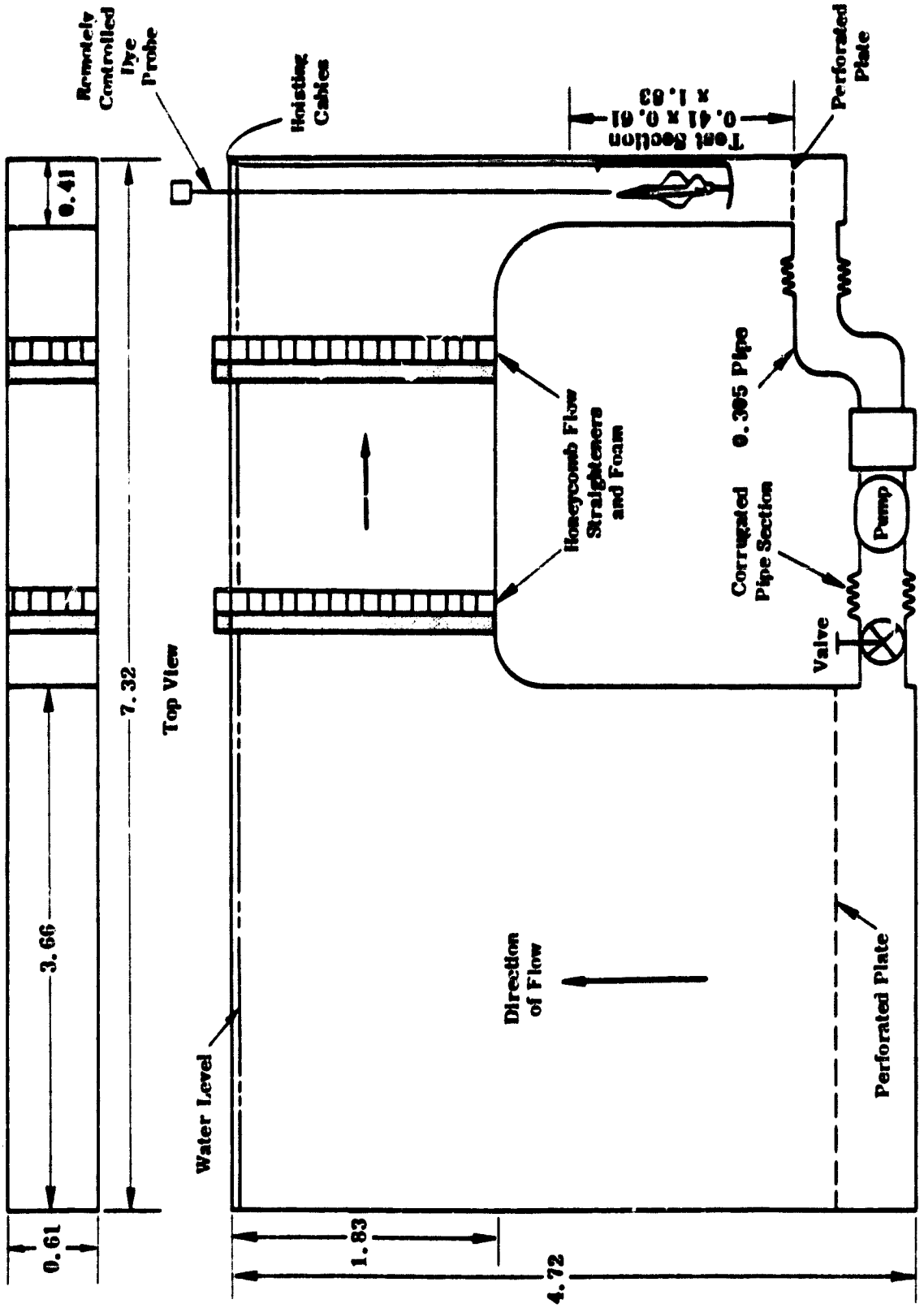

FIGURE 1. NORTHROP DIAGNOSTIC WATER TUNNEL (ALL DIMENSIONS IN M)

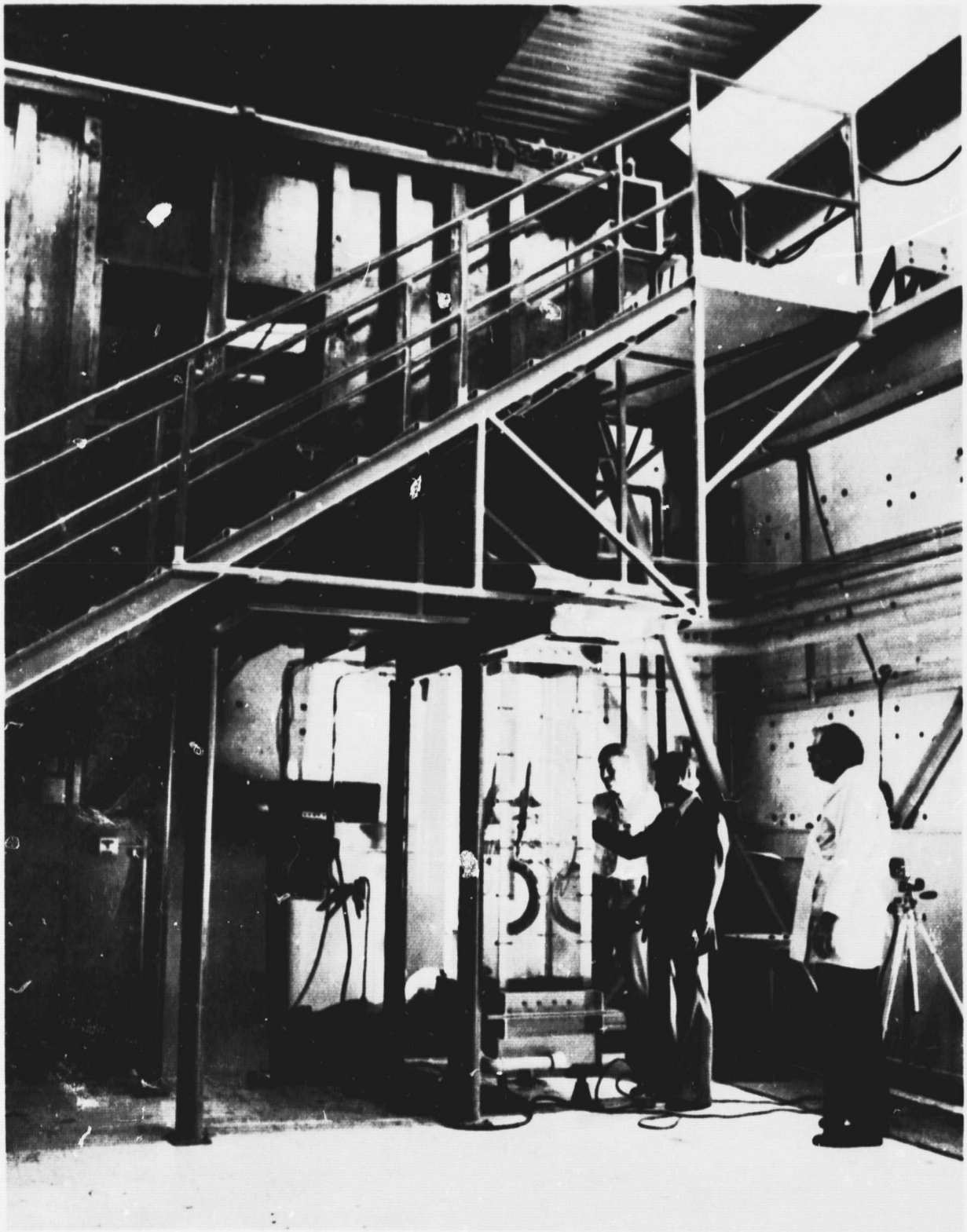

79-03669-7

FIGURE 2. MODEL INSTALLED IN WATER TUNNEL

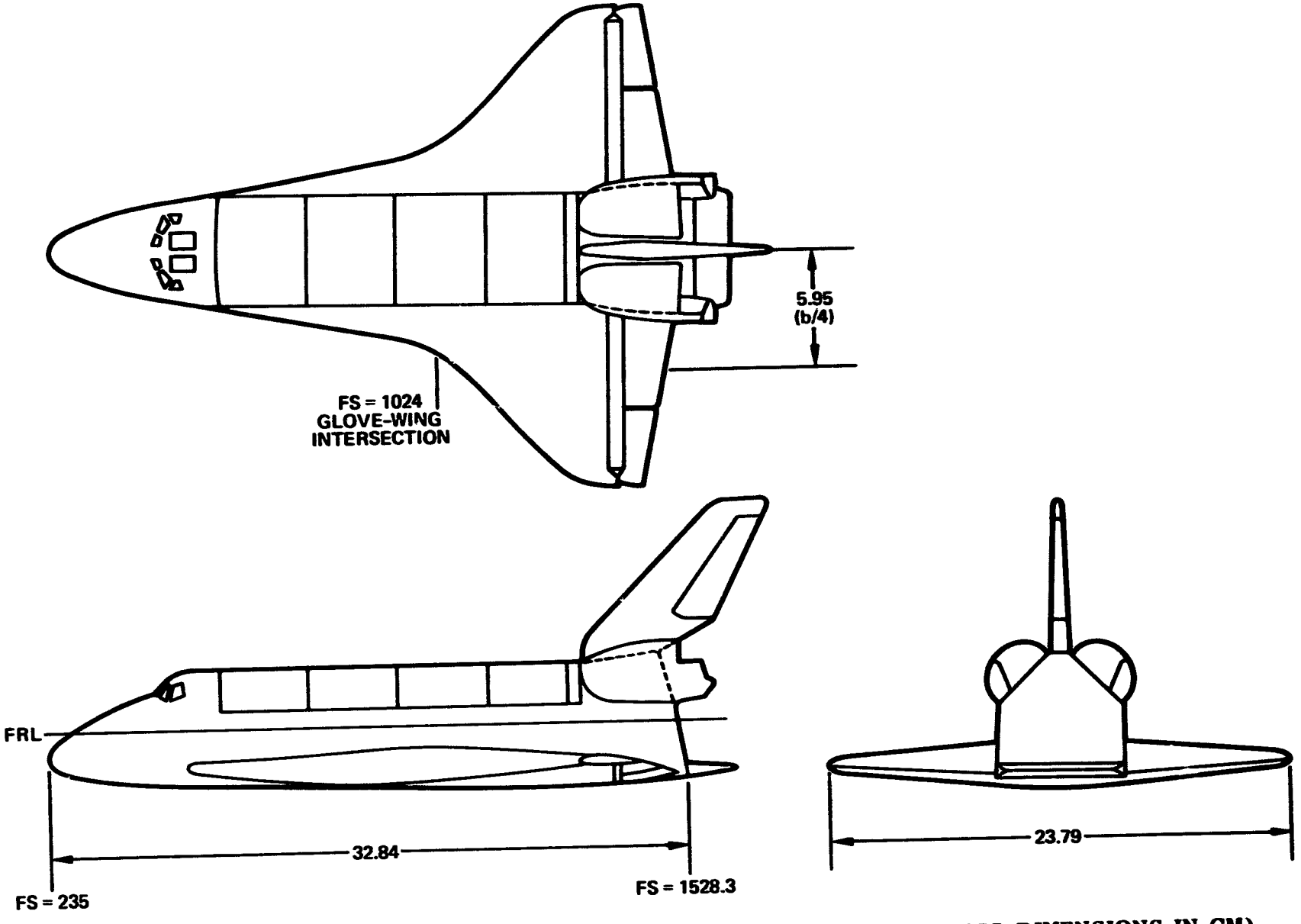

FIGURE 3. 0.01-SCALE SPACE SHUTTLE ORBITER THREE VIEW DRAWING (ALL DIMENSIONS IN CM)

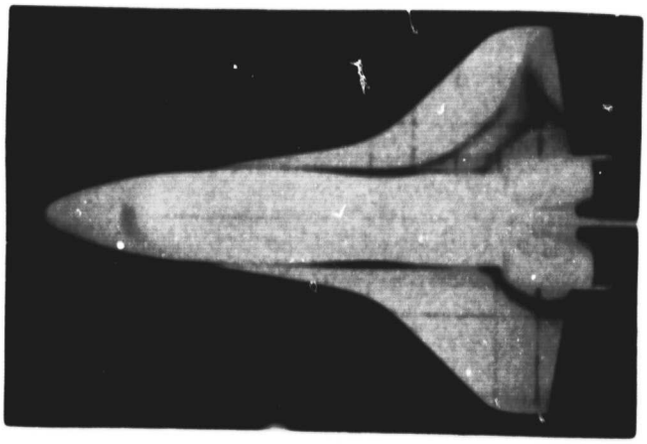

$\alpha = 0^{\circ}$

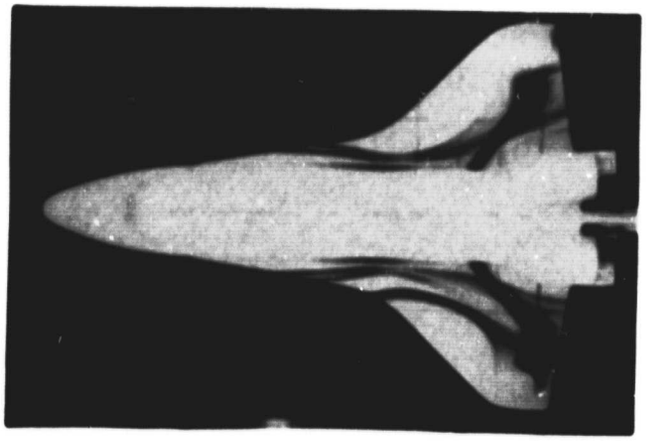

$\alpha = 2^{\circ}$

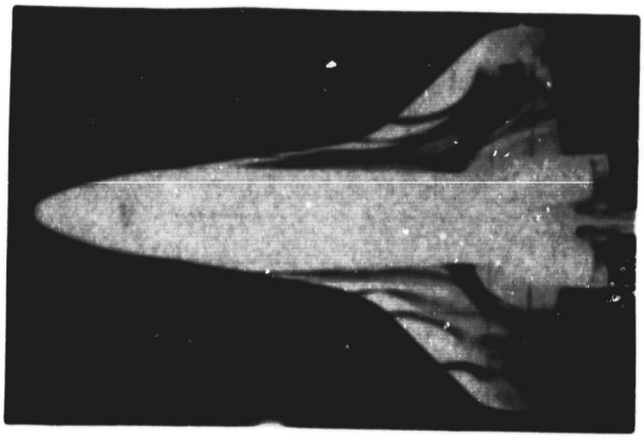

$\alpha = 5^{\circ}$

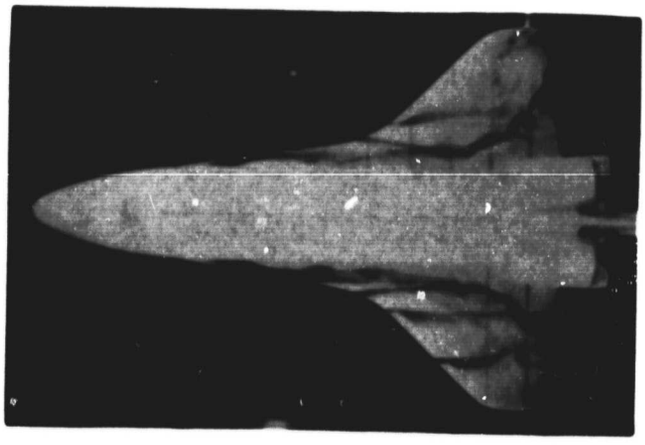

$\alpha = 8^{\circ}$

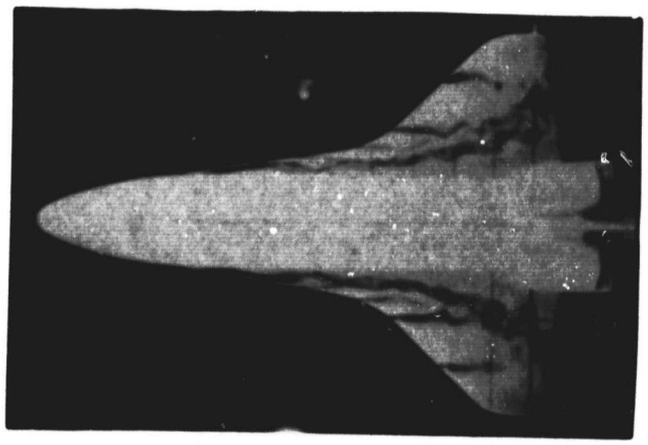

$\alpha = 10^{\circ}$

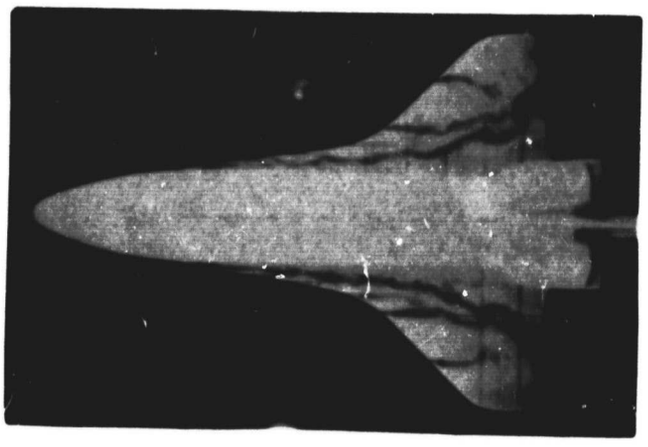

$\alpha = 12^{\circ}$

(a) PLAN VIEW

ORIGINAL PAGE IS OF POOR QUALITY

FIGURE 4. WING GLOVE FLOW FIELD FOR $\beta = 0^{\circ}$

ORIGINAL PAGE IS OF POOR QUALITY

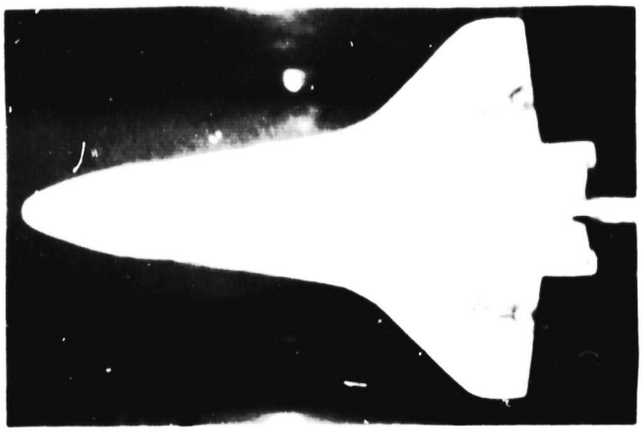

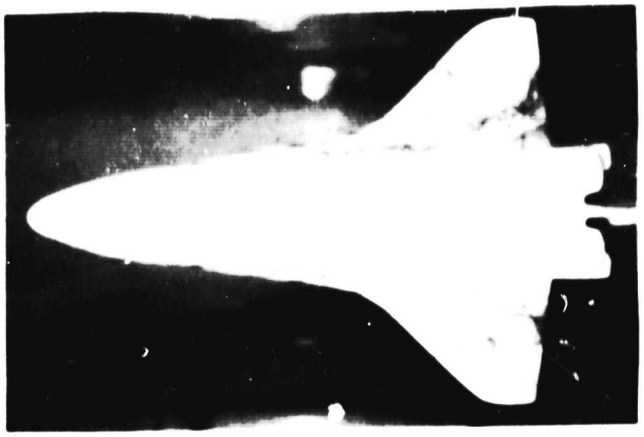

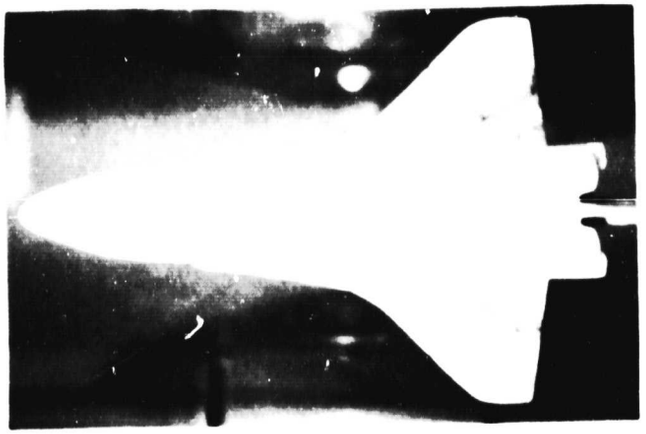

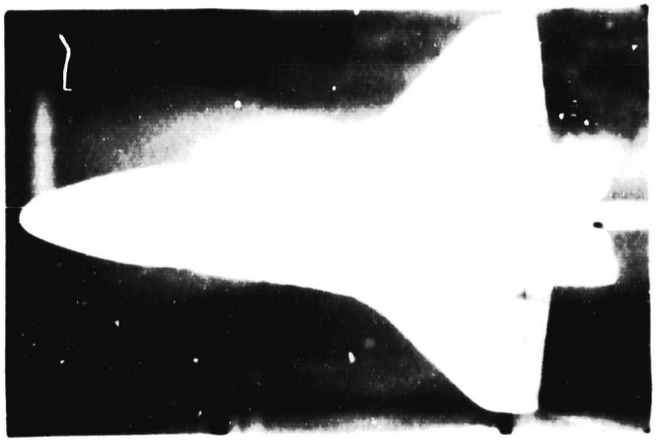

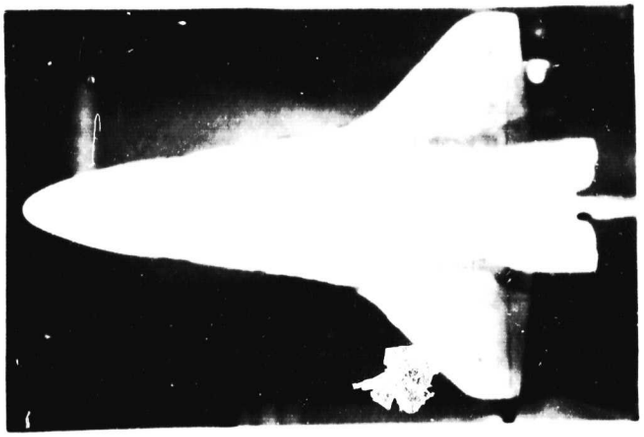

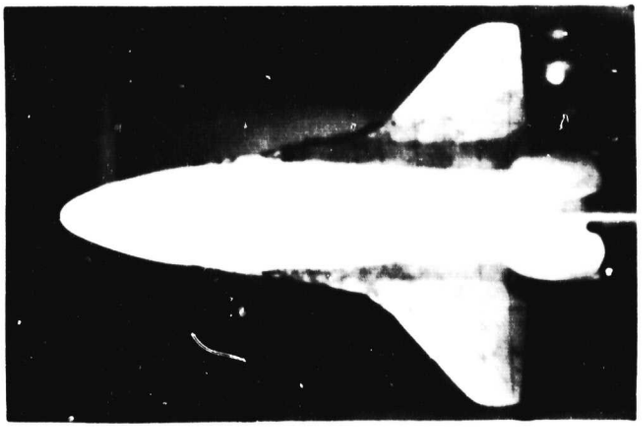

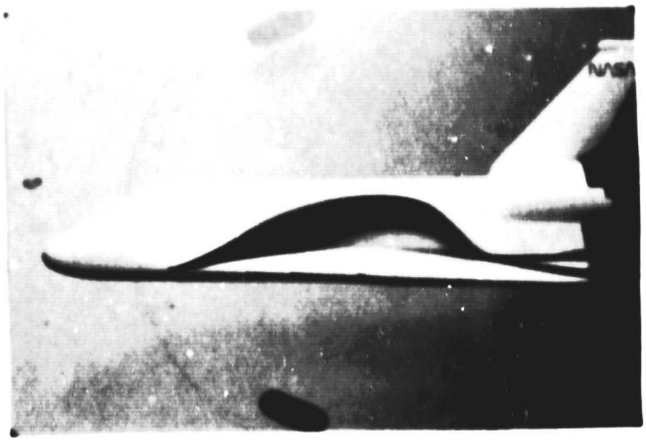

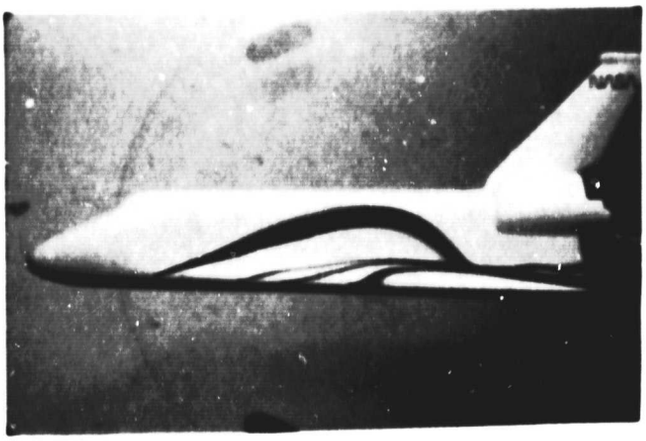

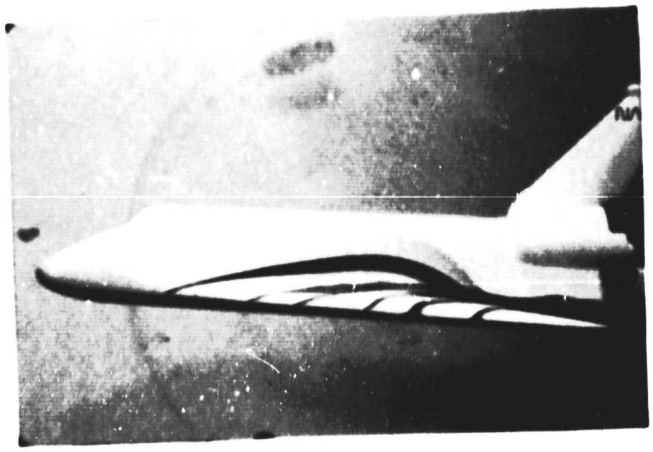

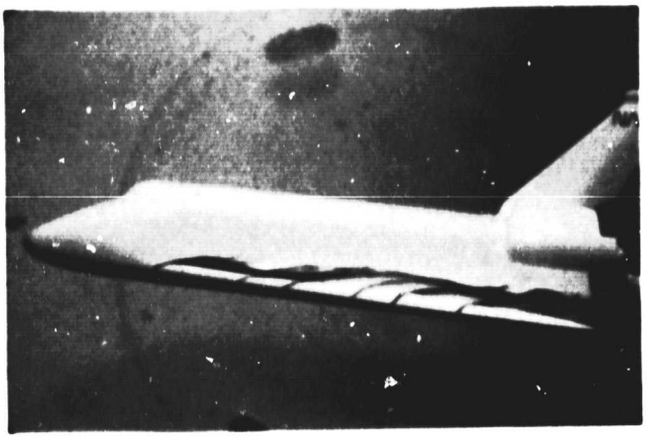

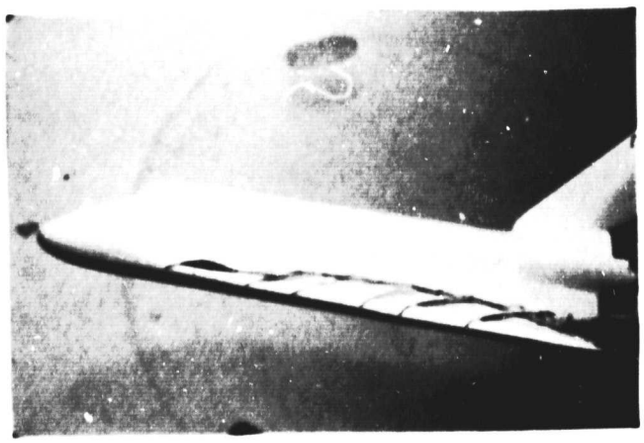

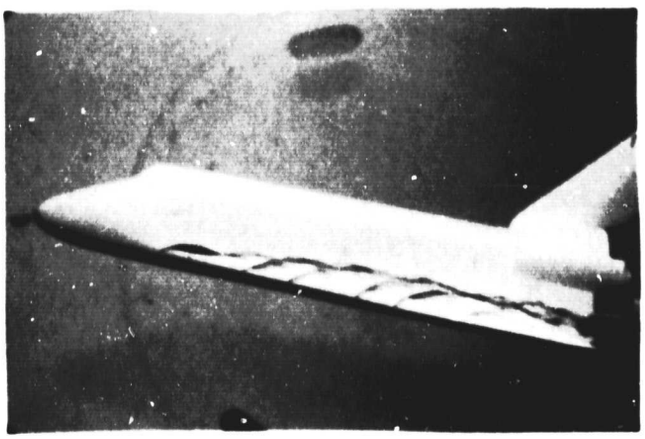

ORIGINAL PAGE IS
OF POOR QUALITY

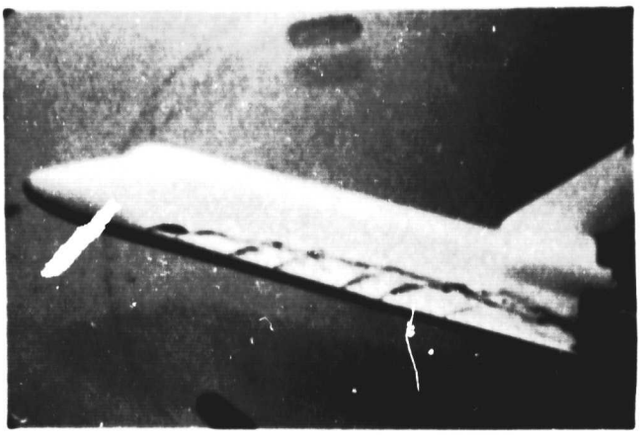

$\alpha = 15^\circ$

$\alpha = 18^\circ$

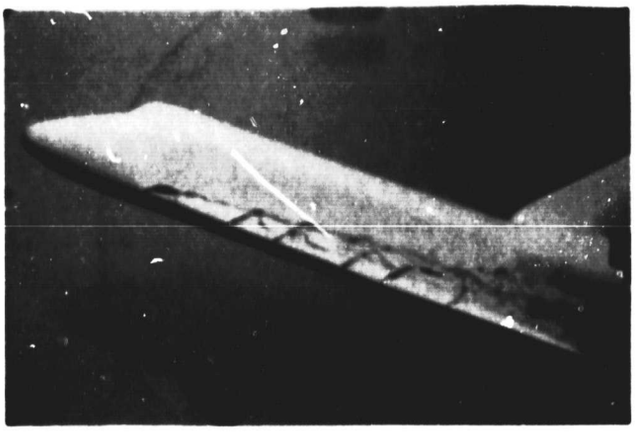

$\alpha = 20^\circ$

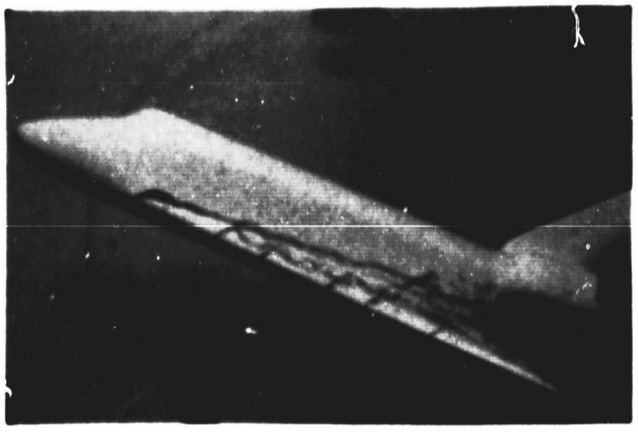

$\alpha = 25^\circ$

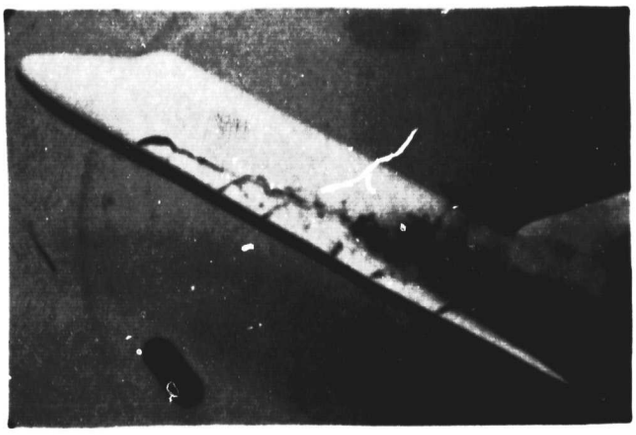

$\alpha = 30^\circ$

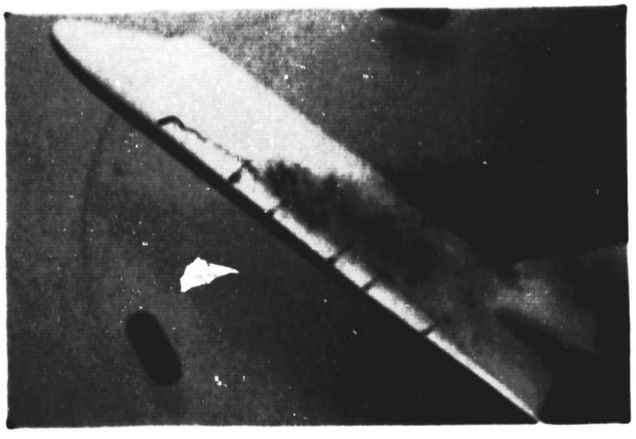

$\alpha = 40$

(B) PROFILE VIEW $\beta = 0^\circ$

FIGURE 4. WING GLOVE FLOW FIELD FOR $\beta = 0^\circ$ (CONCLUDED)

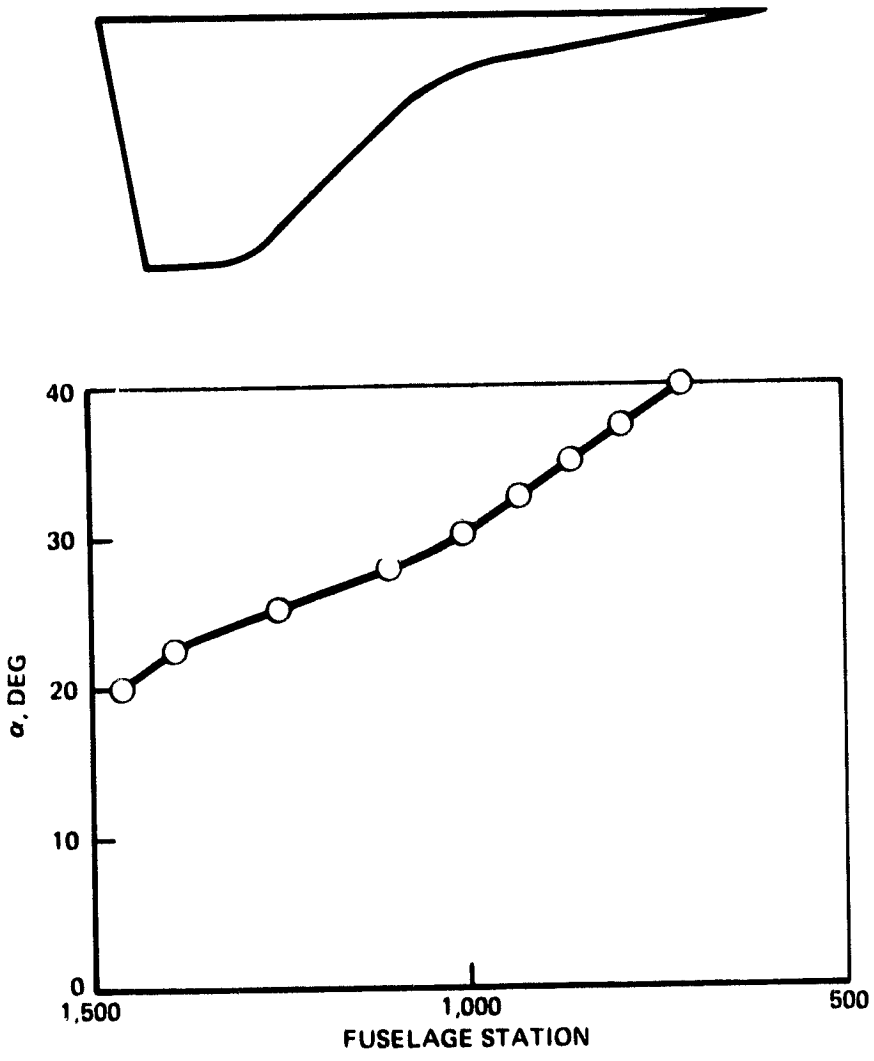

FIGURE 5. GLOVE VORTEX BREAKDOWN LOCATION

		Facility (Method)	Reynolds No.
○	Northrop 16 x 24 in.	Water Tunnel (Dye)	$2.0(10^4)$
●	Northrop 6 x 6 in.	Water Tunnel (Dye)	$1.5(10^4)$
□	Wentz	Wind Tunnel (Schlieren)	10^6 (approx.)
◇	Poisson-Quinton & Erlich	Water Tank (Dye; aluminum Particles)	$2(10^4)$ (approx.)
△	Chigier	Wind Tunnel (Laser anemometer)	$2(10^6)$ (approx.)
▽	Earnshaw and Lawford	Wind Tunnel (Tuft probe)	(10^6) (approx.)
▲	Hummel and Srinivasan	Wind Tunnel (Smoke)	(10^6) (approx.)
☆	Lowson	Water Tunnel (Dye)	$3(10^4)$

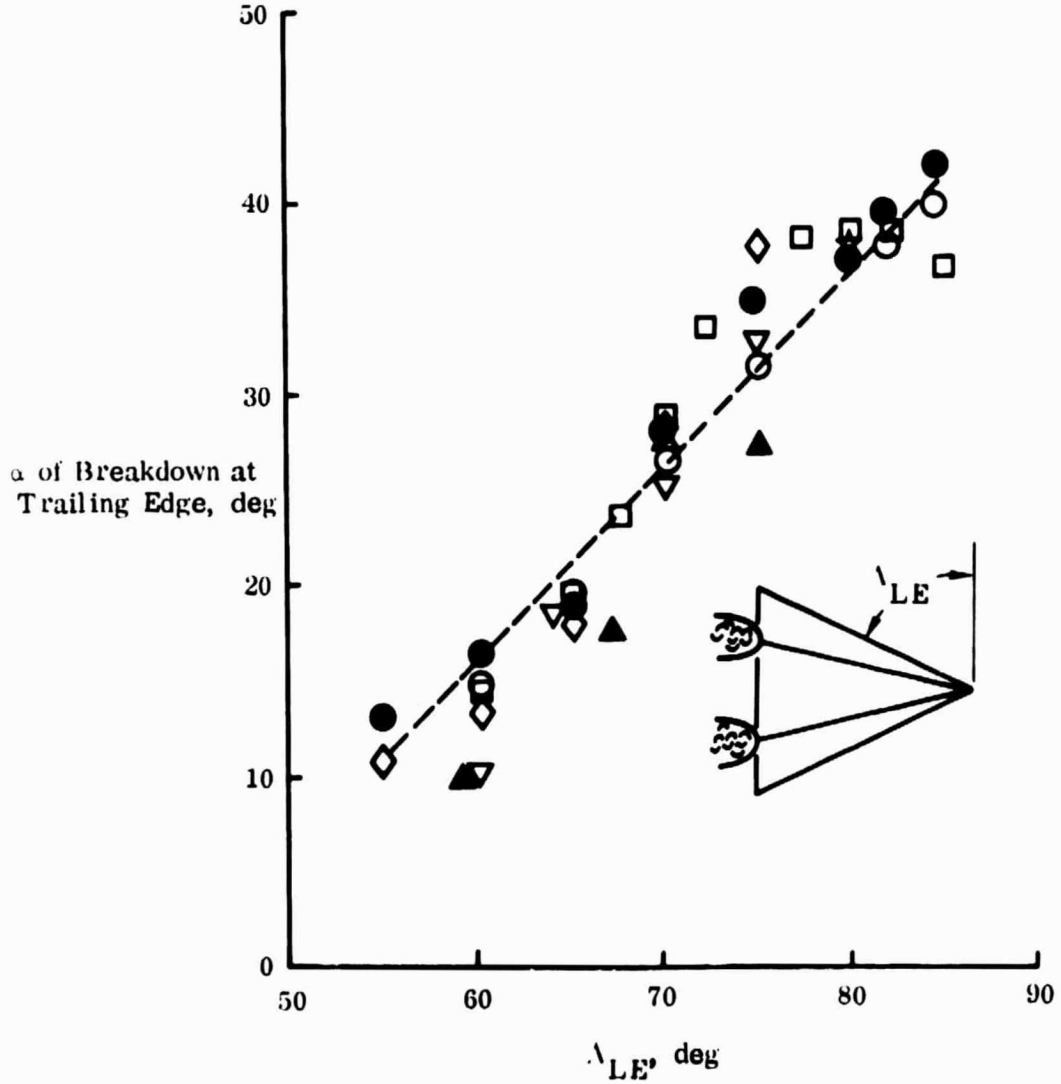

FIGURE 6. EFFECT OF LEADING-EDGE SWEEP ON THE ANGLE OF ATTACH OF VORTEX BREAKDOWN AT THE TRAILING EDGE OF DELTA WINGS (DATA FROM REFERENCE 5)

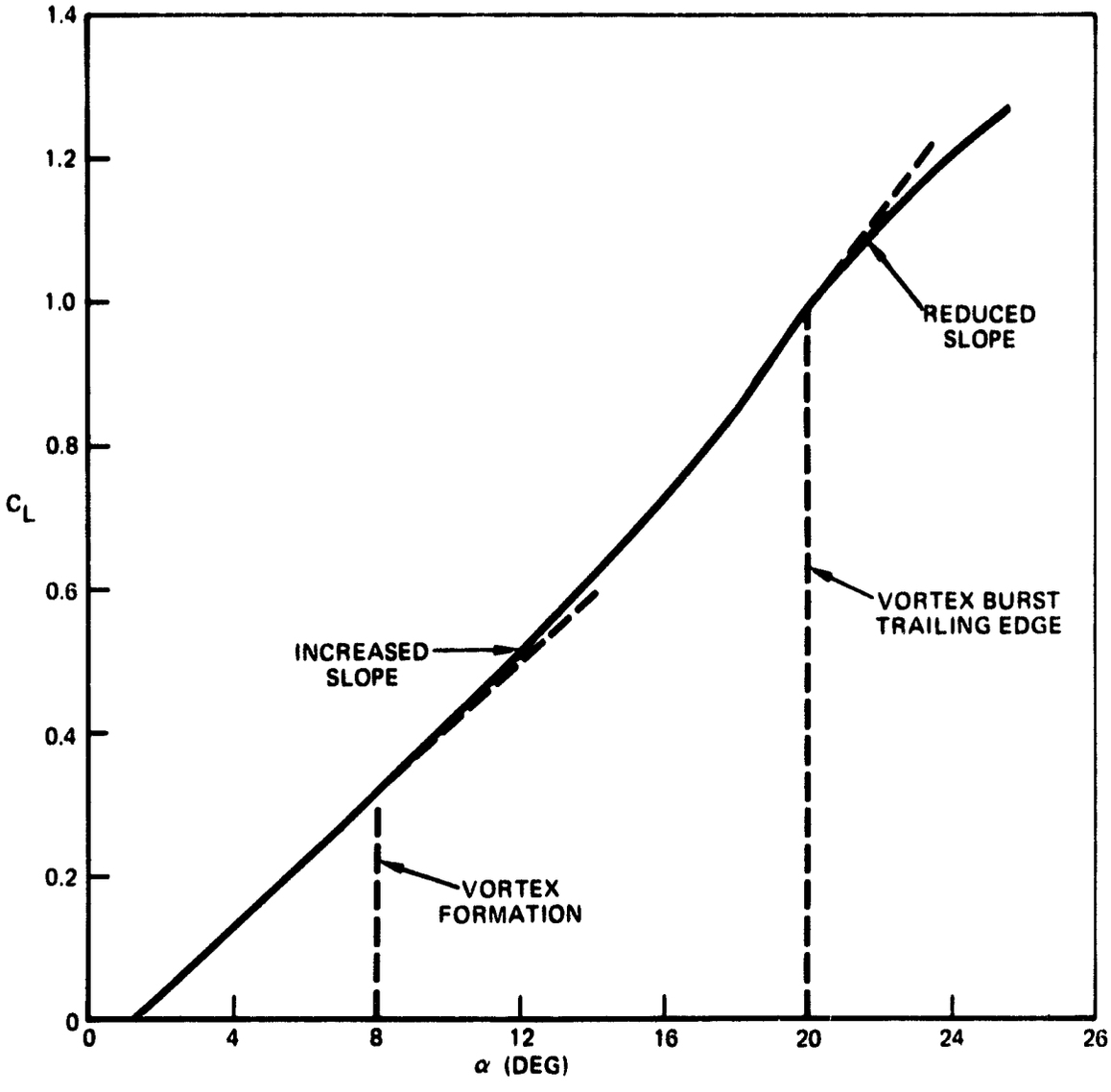

FIGURE 7. LIFT CHARACTERISTICS OF THE ORBITER

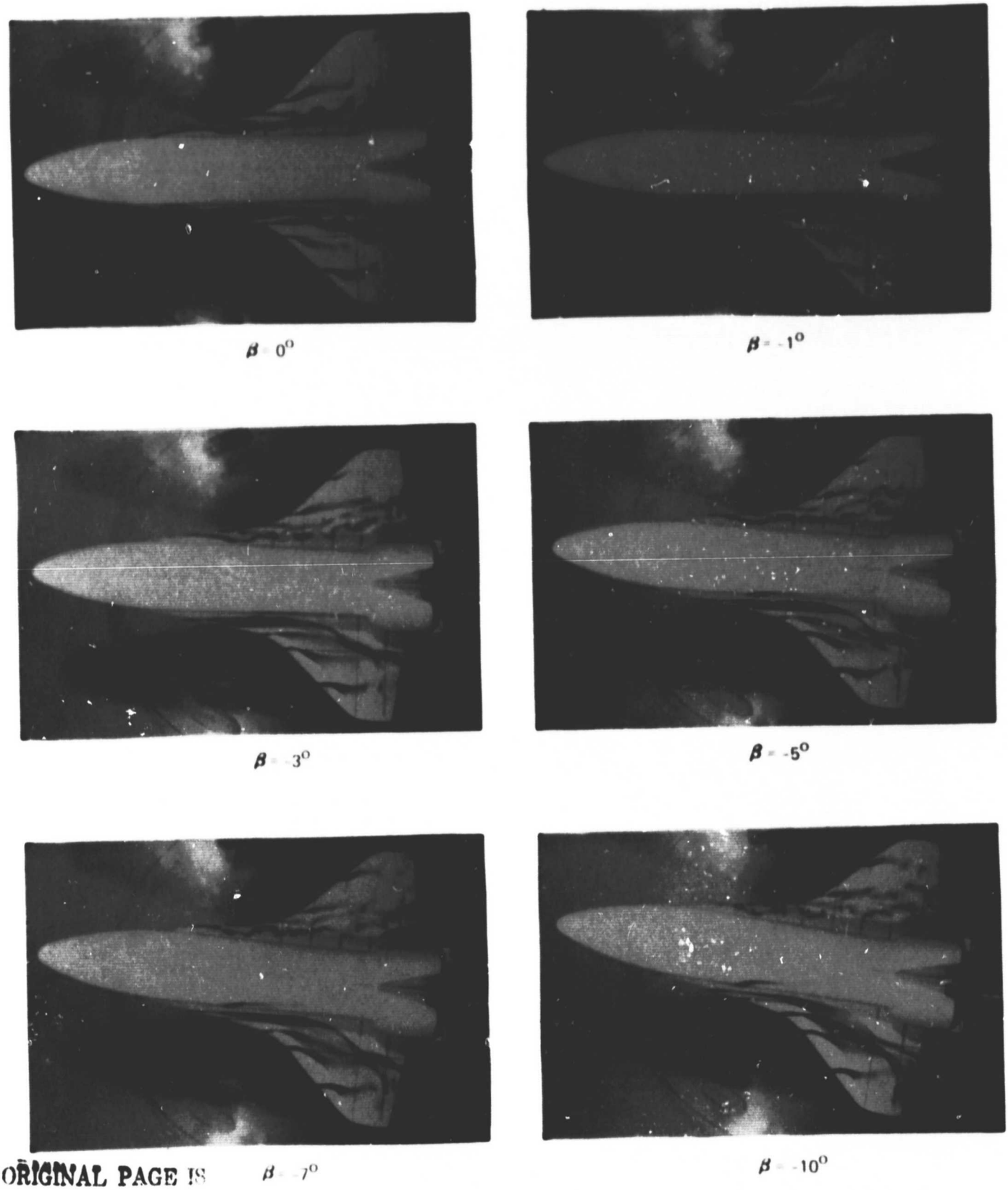

ORIGINAL PAGE IS
OF POOR QUALITY

(A) PLAN VIEW

FIGURE 8. WING-GLOVE FLOW FIELD IN SIDESLIP FOR $\alpha = 8°$

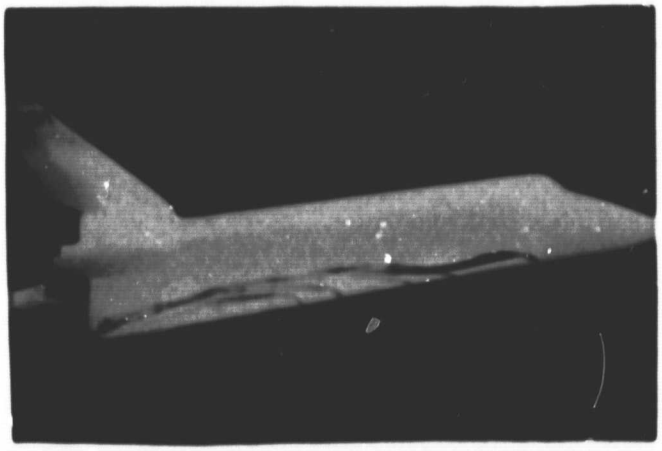

$\beta = 0^{o}$

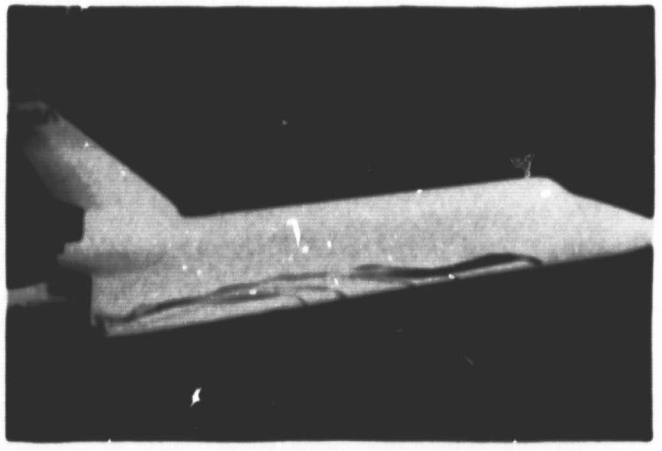

$\beta = 1^{o}$

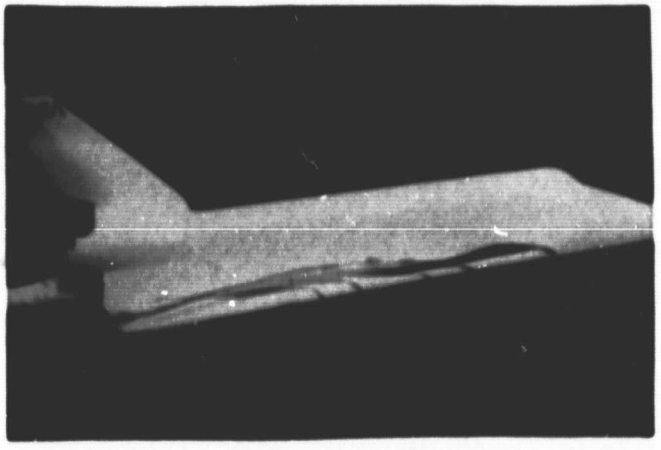

$\beta = 3^{o}$

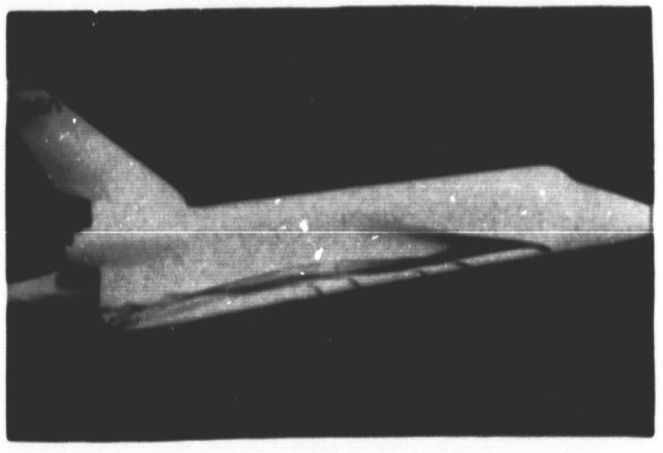

$\beta = 5^{o}$

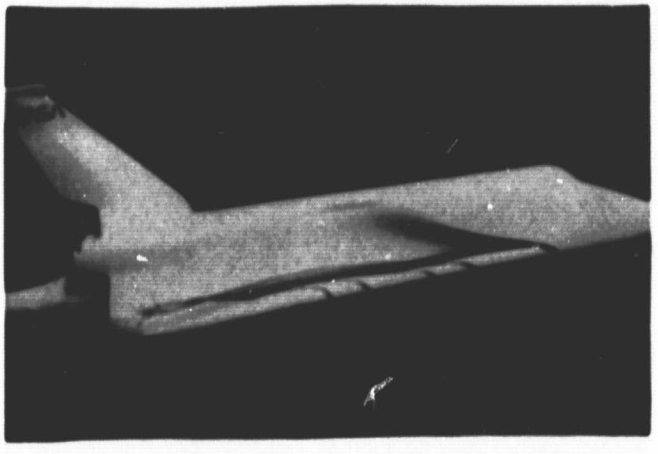

$\beta = 7^{o}$

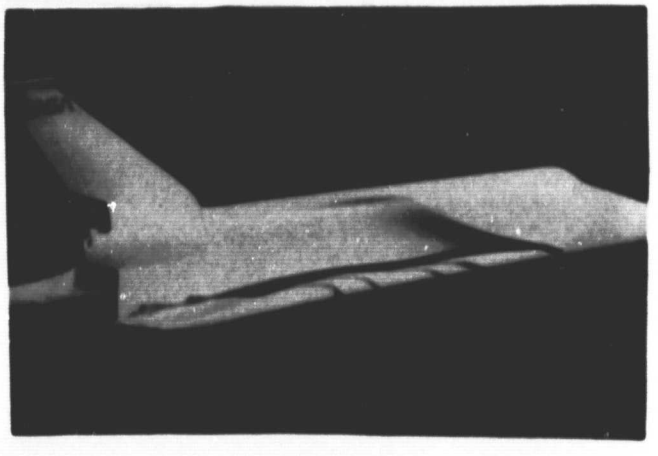

$\beta = 10^{o}$

(B) WINDWARD PROFILE VIEW, $\alpha = 8^{o}$

FIGURE 8. WING-GLOVE FLOW FIELD IN SIDESLIP FOR $\alpha = 8^{\circ}$ (Continued)

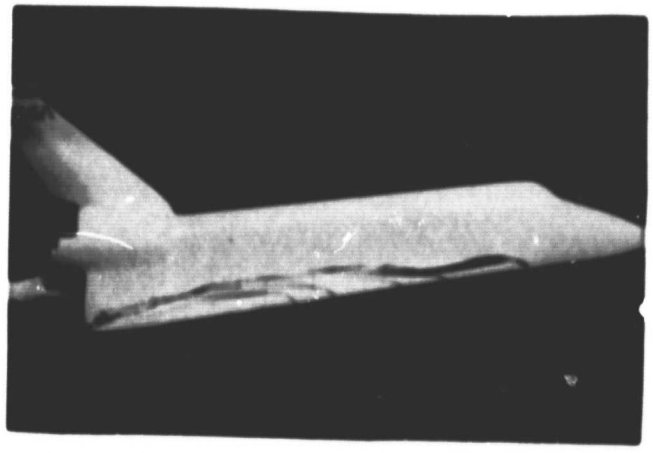

$\beta = 0^{\circ}$

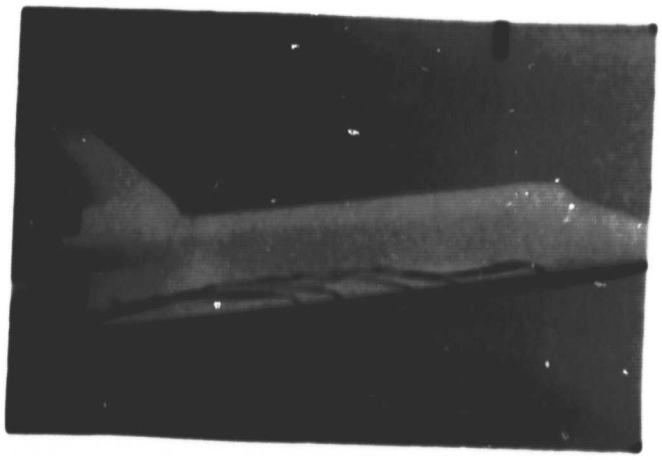

$\beta = -1^{\circ}$

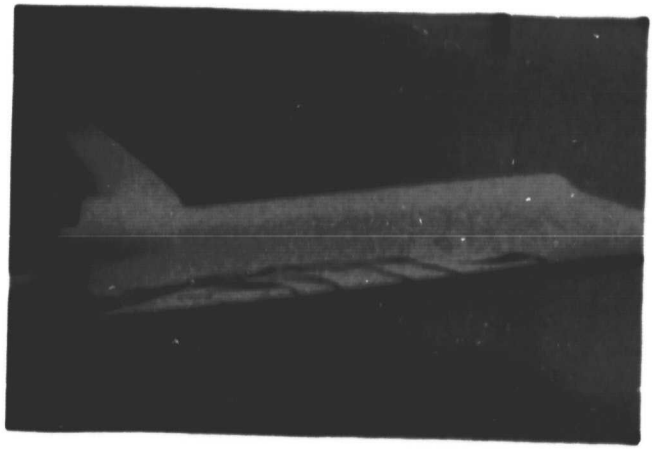

$\beta = 3^{\circ}$

$\beta = -5^{\circ}$

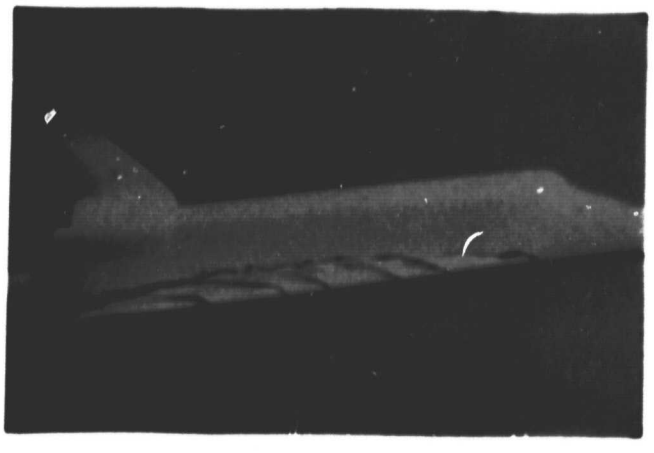

$\beta = 7^{\circ}$

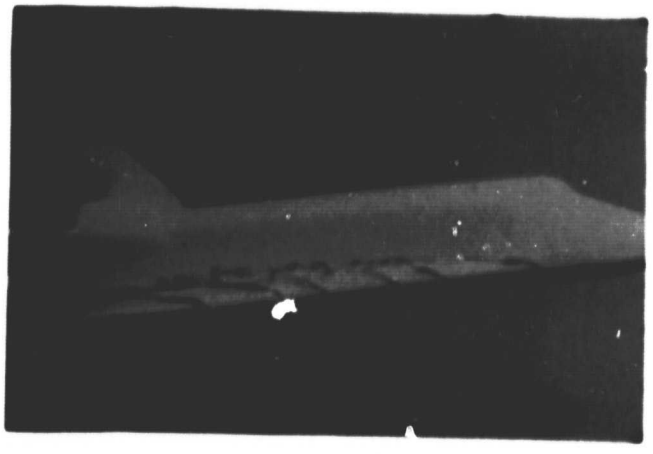

$\beta = -10^{\circ}$

(c) LEEWARD PROFILE VIEW $\alpha = 8^{\circ}$

FIGURE 8. WING GLOVE FLOW FIELD IN SIDESLIP FOR $\alpha = 8^{\circ}$ (Concluded)

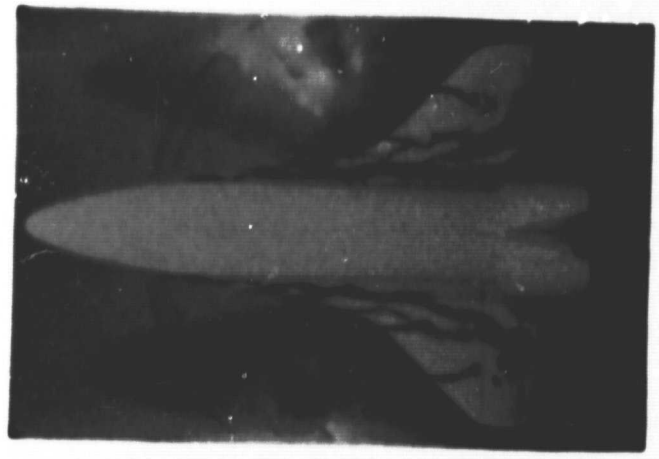

$\beta = 0^{o}$

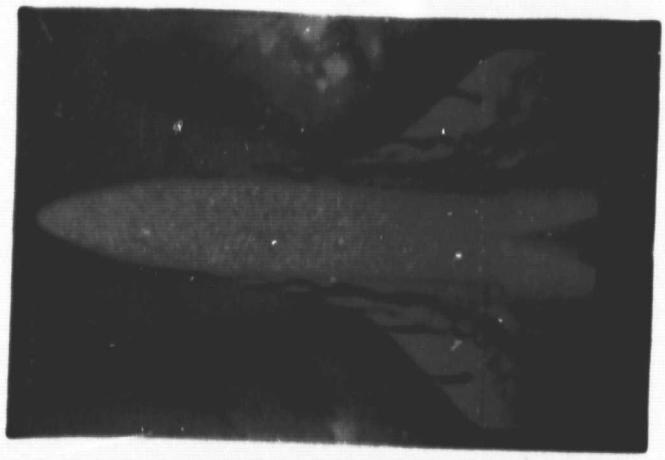

$\beta = -1^{o}$

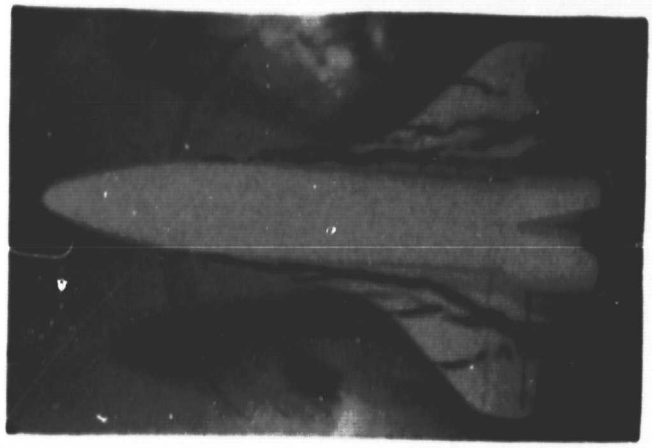

$\beta = -3^{o}$

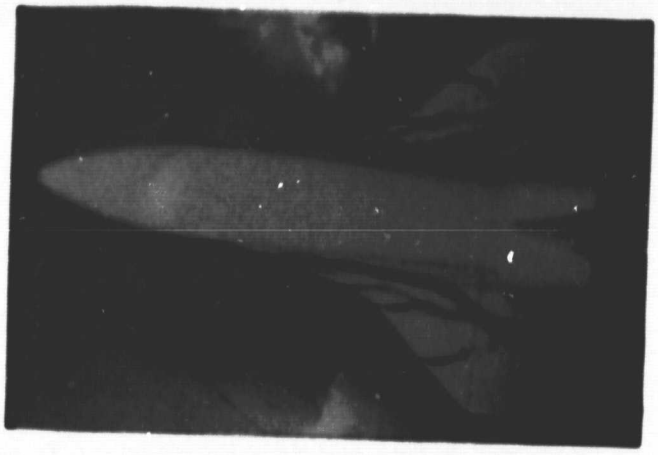

$\beta = -5^{o}$

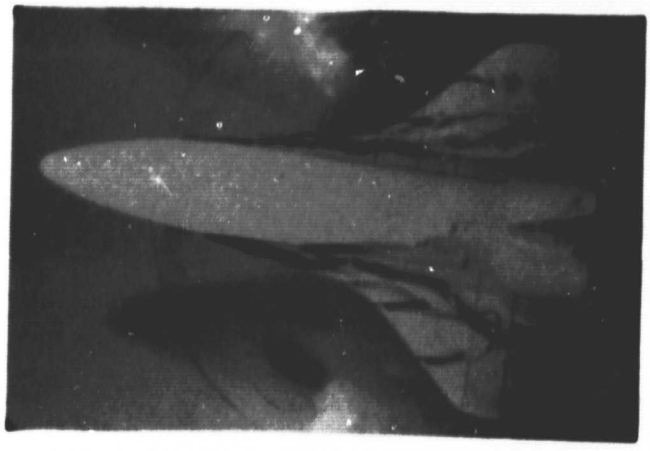

$\beta = -7^{o}$

$\beta = -10^{o}$

(A) PLAN VIEW

ORIGINAL PAGE IS
POOR QUALITY

FIGURE 9. WING GLOVE FLOW FIELD IN SIDESLIP FOR $\alpha = 15^{o}$

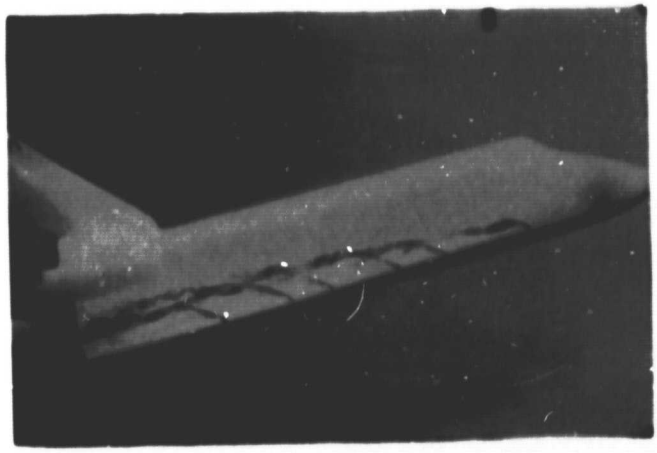

$\beta = 0^{o}$

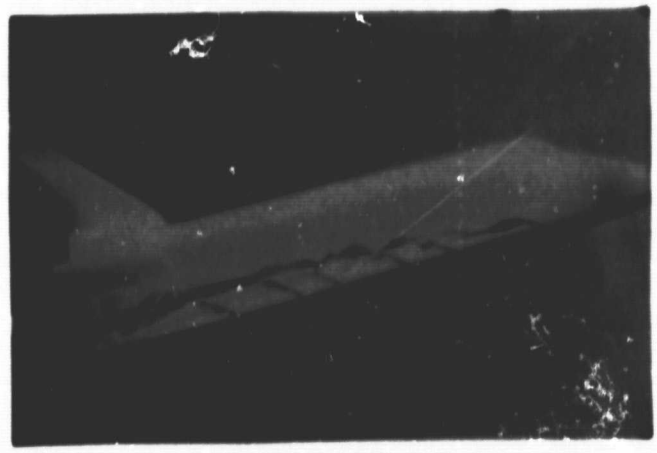

$\beta = 1^{o}$

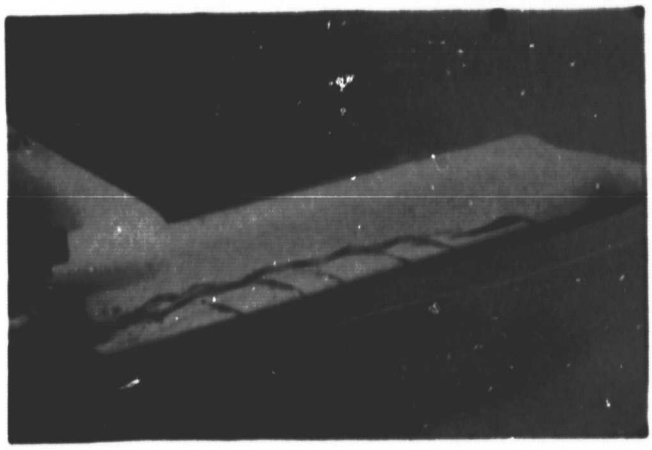

$\beta = 3^{o}$

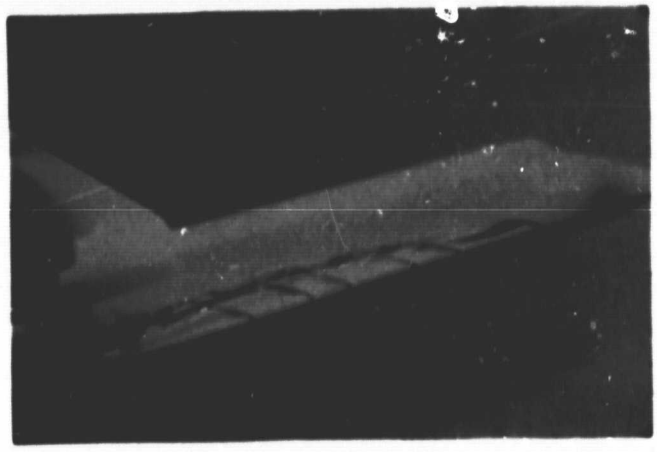

$\beta = 5^{o}$

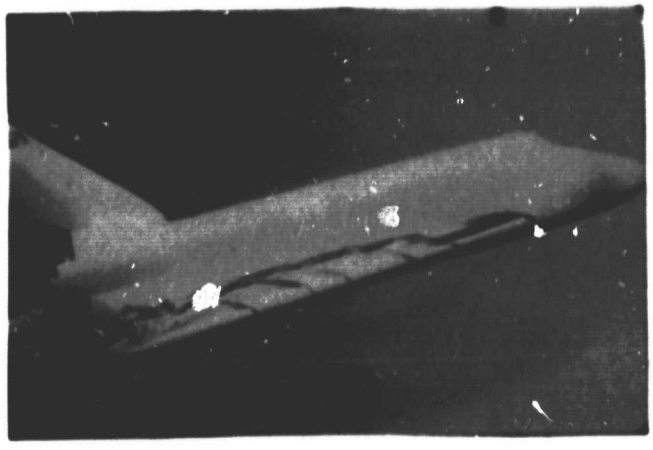

$\beta = 7^{o}$

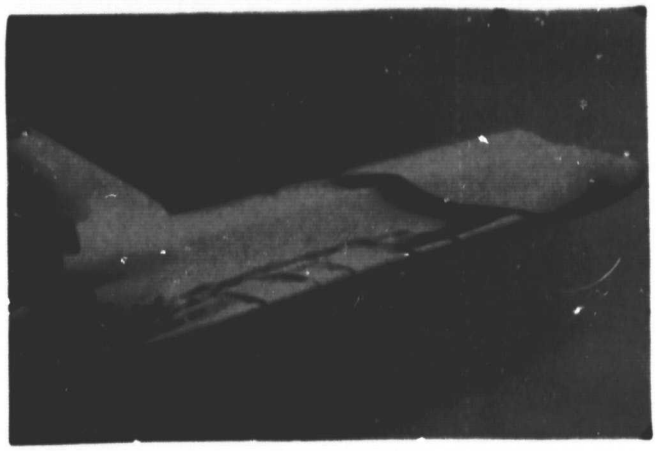

$\beta = 10^{o}$

(B) WINDWARD PROFILE VIEW, $\alpha = 15^{o}$

FIGURE 9. WING GLOVE FLOW FIELD IN SIDESLIP FOR $\alpha = 15^{o}$ (Continued)

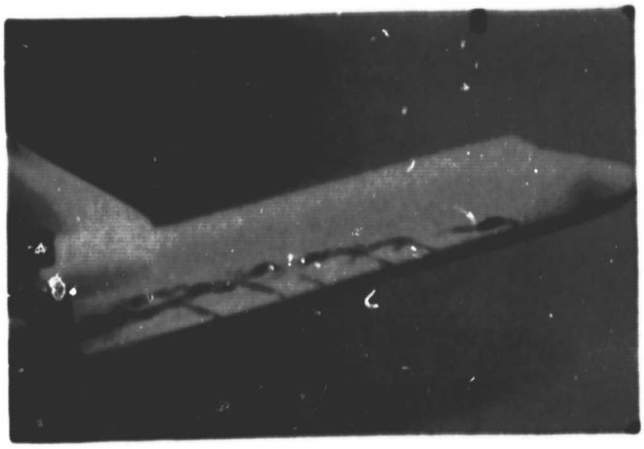

$\beta = 0^{\circ}$

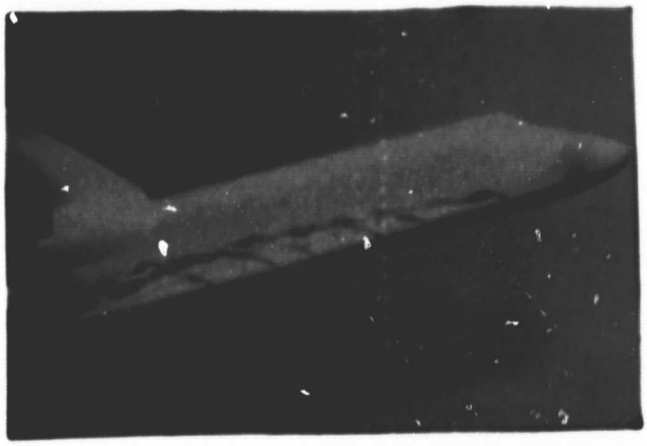

$\beta = -1^{\circ}$

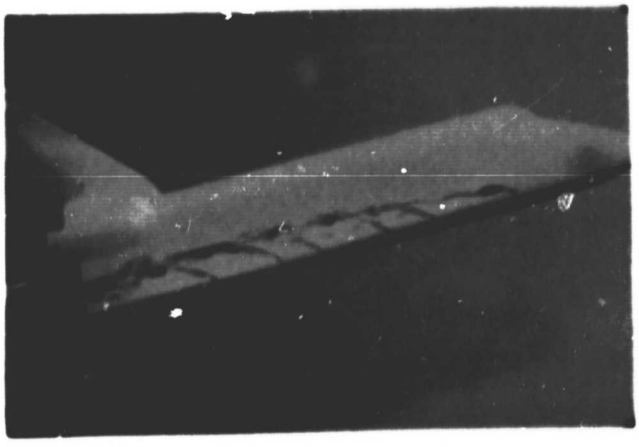

$\beta = -3^{\circ}$

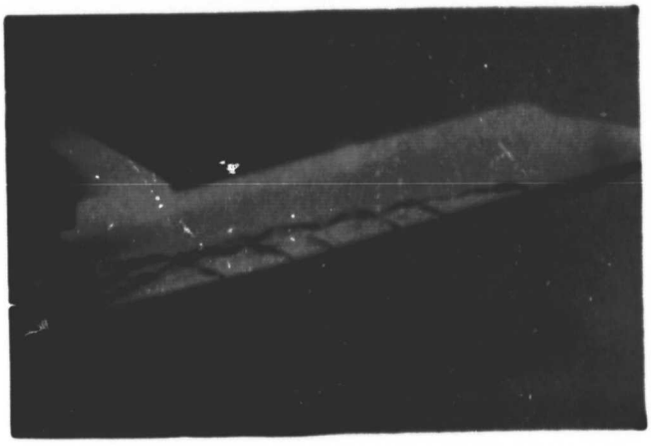

$\beta = -5^{\circ}$

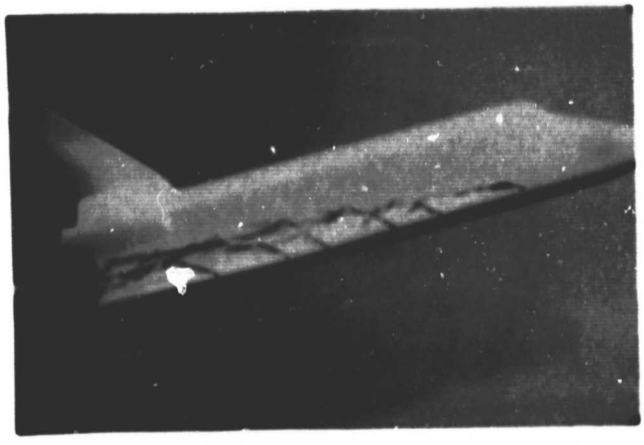

$\beta = -7^{\circ}$

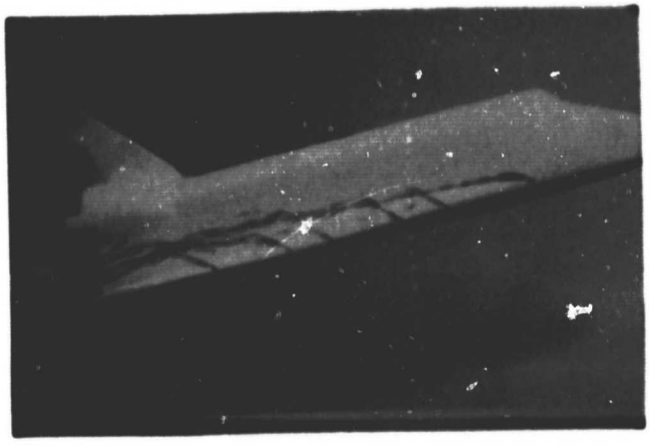

$\beta = -10^{\circ}$

(C) LEEWARD PROFILE VIEW $\delta = 15^{\circ}$

FIGURE 9. WING GLOVE FLOW FIELD IN SIDESLIP FOR $\delta = 15^{\circ}$ (Concluded)

ORIGINAL PAGE IS
OF POOR QUALITY

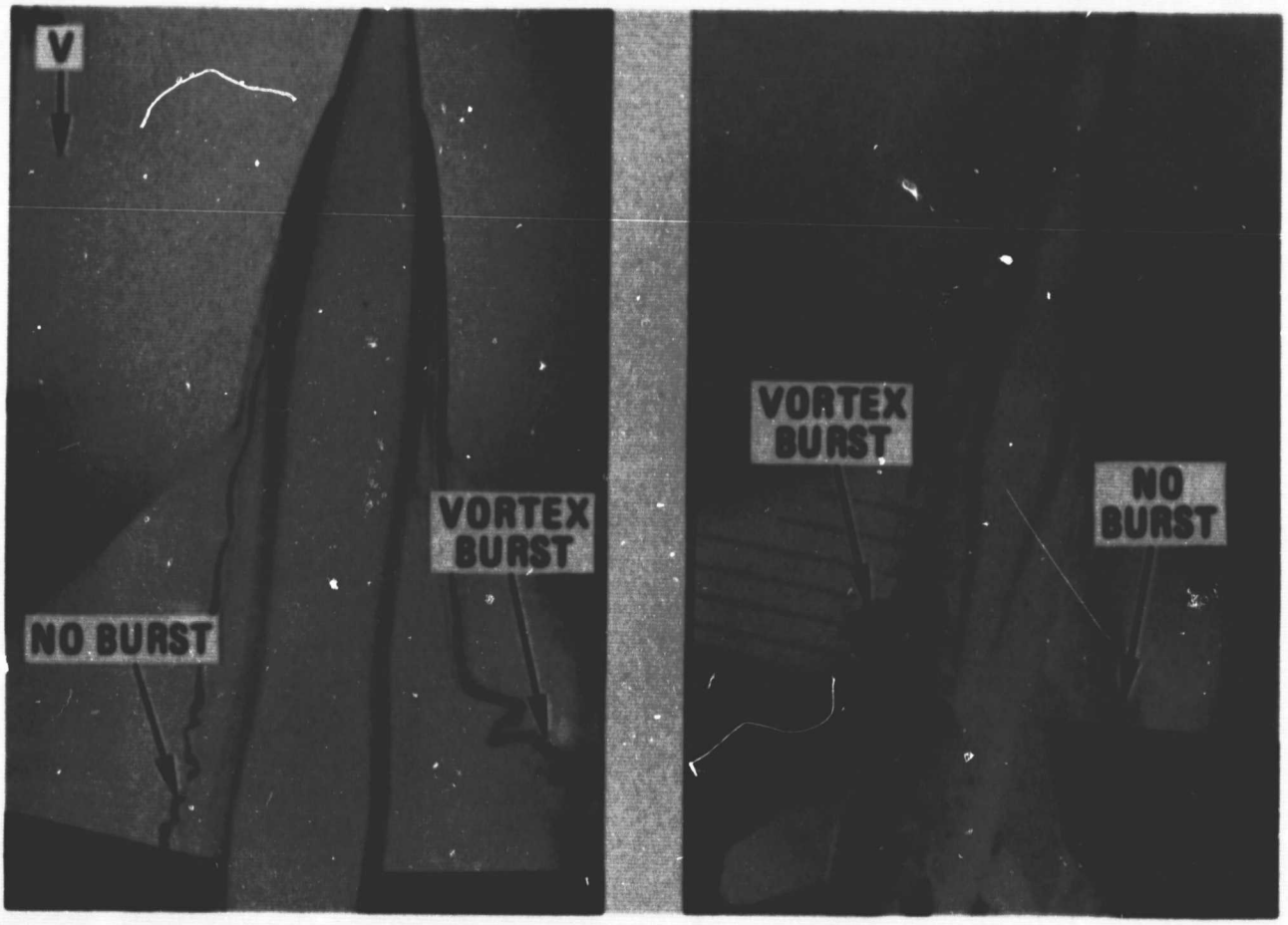

FIGURE 10. ASYMMETRIC VORTEX BURST ON AIRCRAFT CONFIGURATIONS IN SIDESLIP (FROM REF. 5)

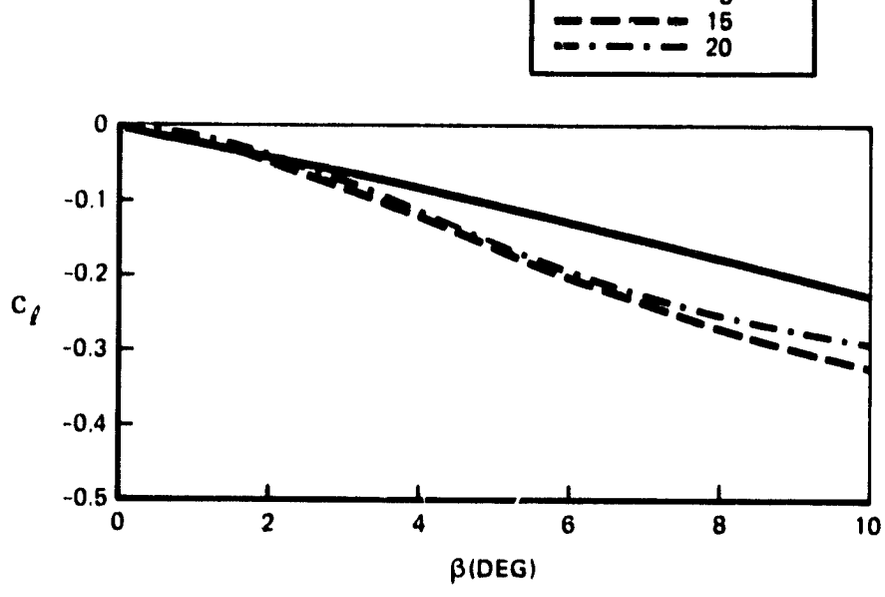

FIGURE 11. VARIATION OF ROLLING MOMENT WITH SIDESLIP OF THE ORBITER

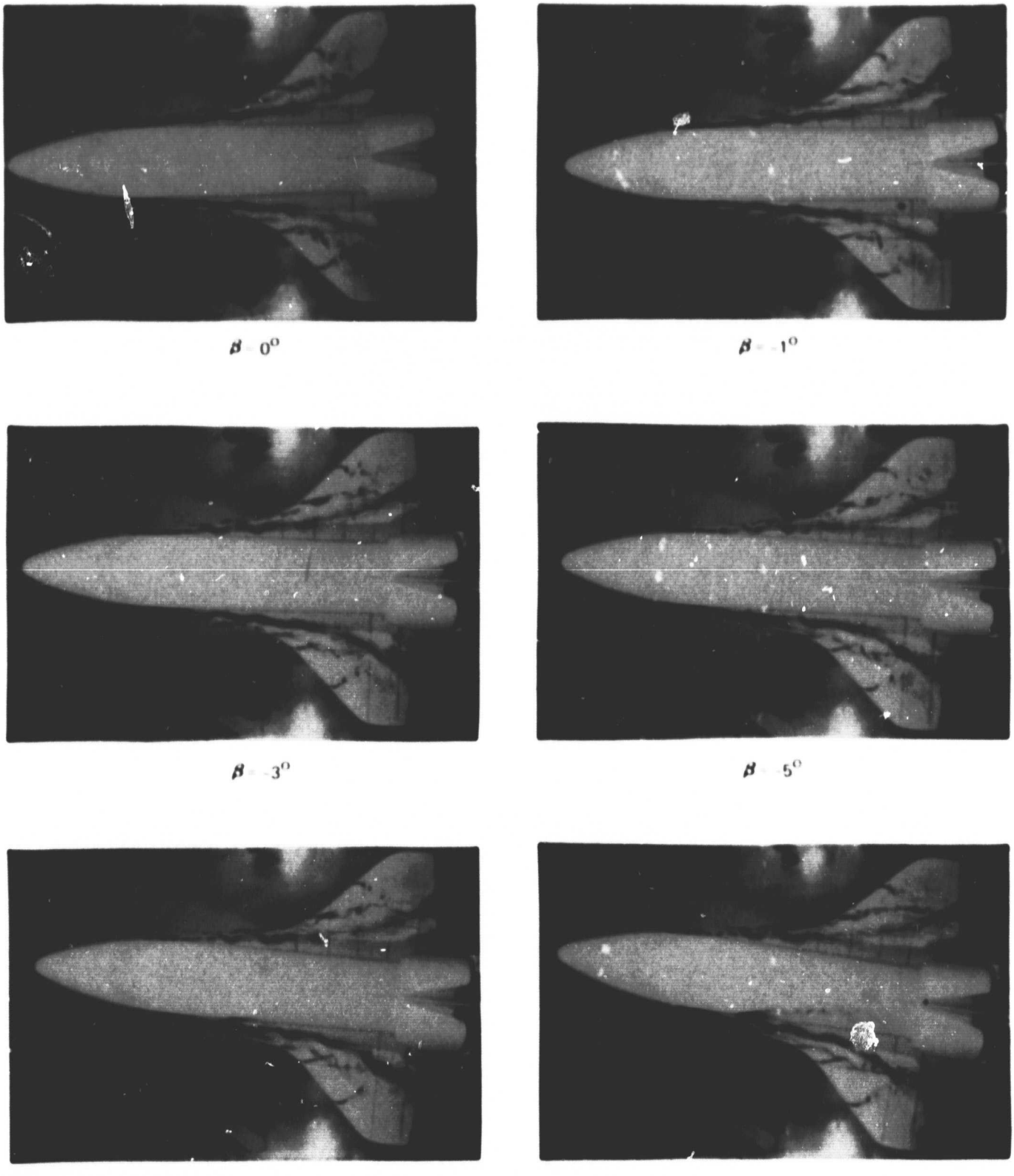

$\beta = 0^{o}$

$\beta = -1^{o}$

$\beta = -3^{o}$

$\beta = -5^{o}$

$\beta = -7^{o}$

$\beta = -10^{o}$

(A) PLAN VIEW

FIGURE 12. WING-GLOVE FLOW FIELD IN SIDESLIP FOR $\alpha = 20^{o}$

ORIGINAL PAGE IS
OF POOR QUALITY

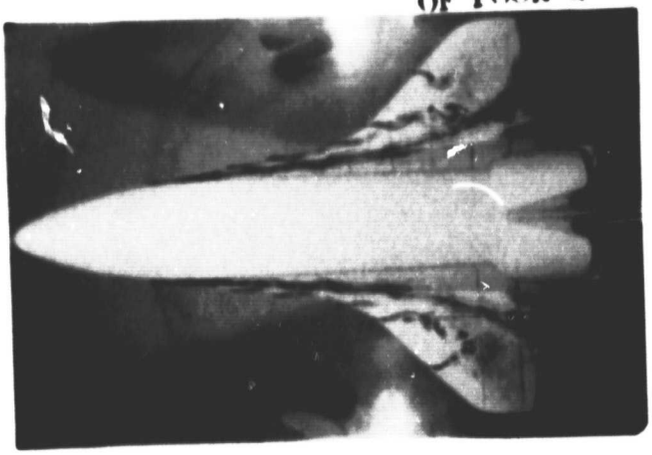

β 0°

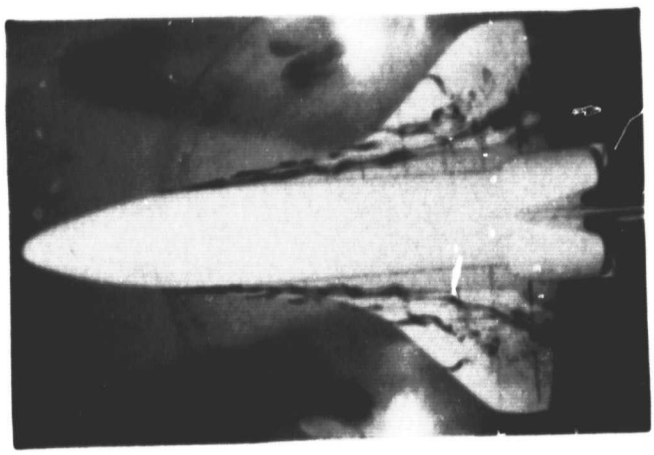

β 1°

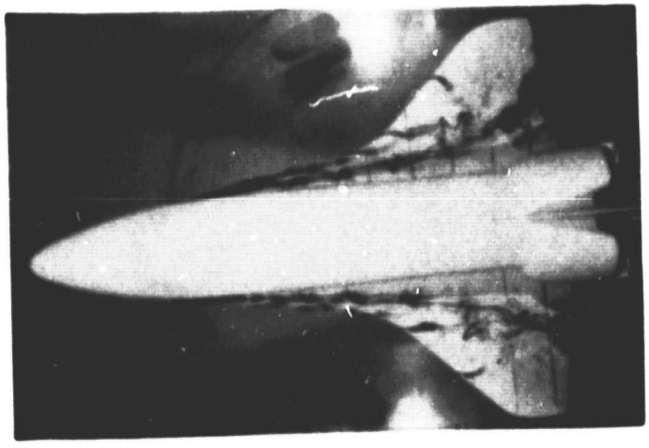

β 3°

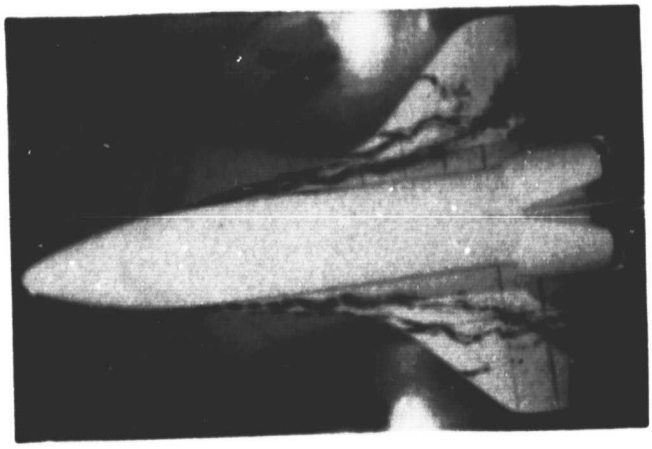

β 5°

β 7°

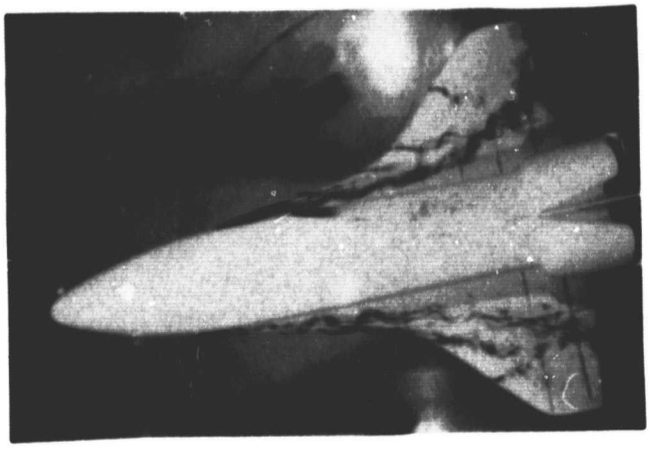

β 10°

(A) PLAN VIEW, α = 20°

FIGURE 12. WING GLOVE FLOW FIELD IN SIDESLIP FOR α = 20° (Continued)

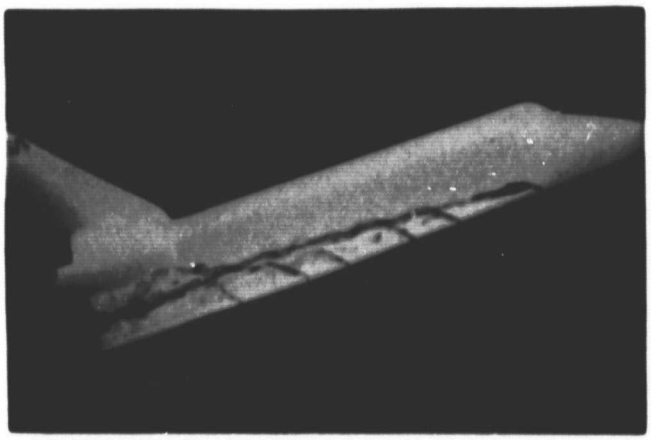

$\beta = 0^{o}$

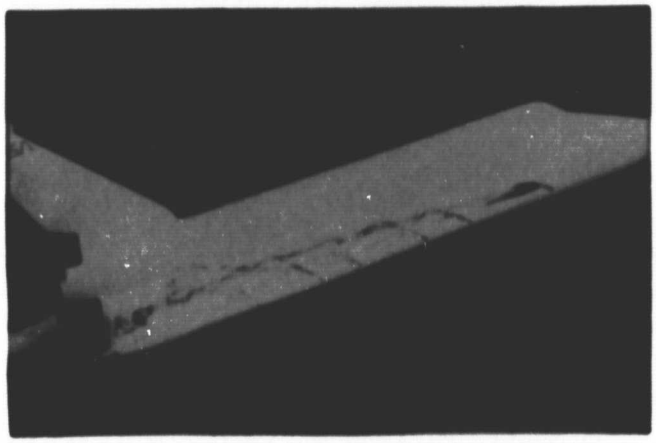

$\beta = 3^{o}$

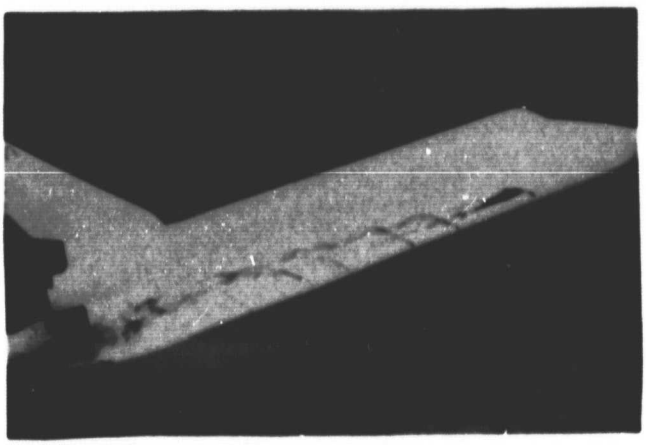

$\beta = 5^{o}$

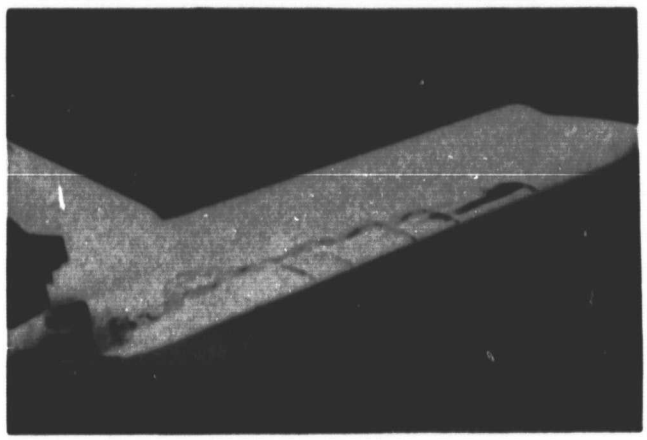

$\beta = 7^{o}$

(B) WINDWARD PROFILE VIEW, $\alpha = 20^{o}$

FIGURE 12. WING-GLOVE FLOW FIELD IN SIDESLIP FOR $\alpha = 20^{\circ}$ (Continued)

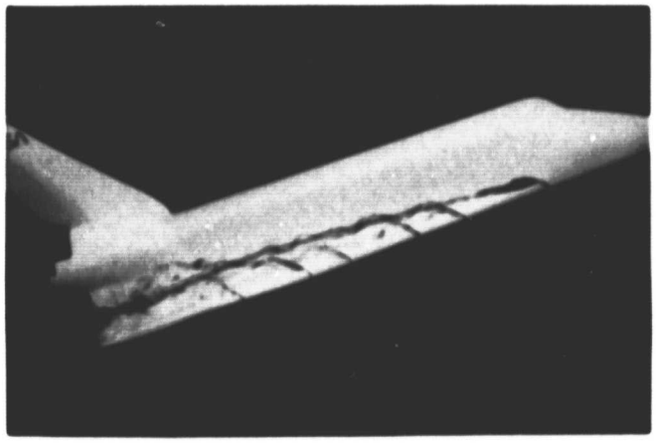

$\beta = 0^{\circ}$

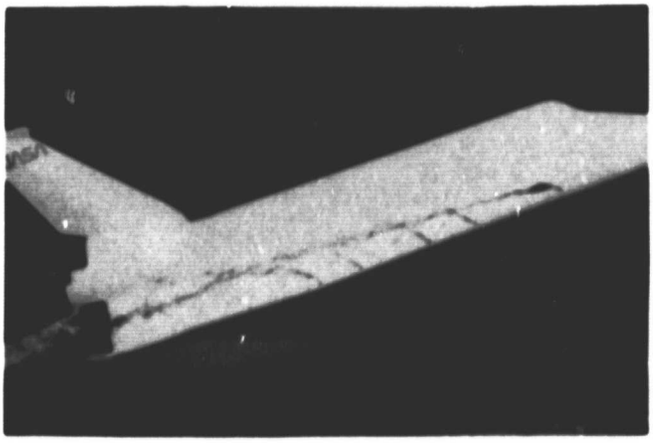

$\beta = 3^{\circ}$

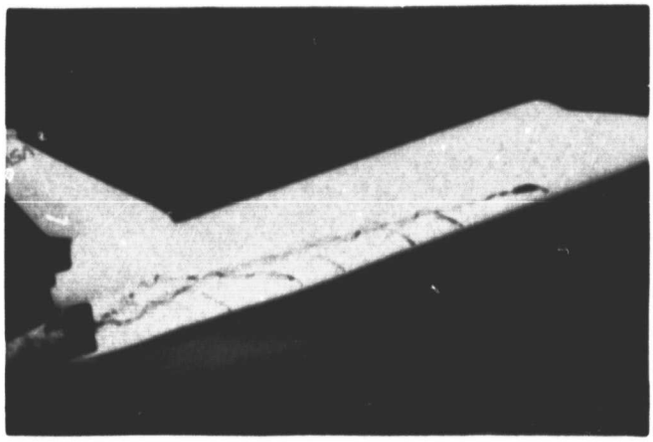

$\beta = 5^{\circ}$

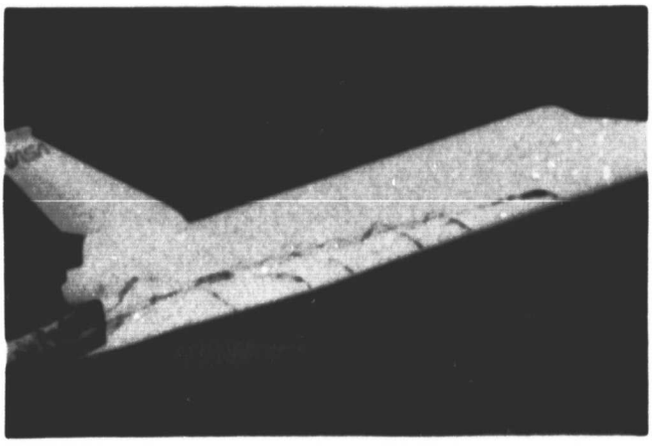

$\beta = 7^{\circ}$

(C) LEEWARD PROFILE VIEW, $\alpha = 20^{\circ}$

FIGURE 12. WING GLOVE FLOW FIELD IN SIDESLIP FOR $\alpha = 20^{\circ}$ (Concluded)

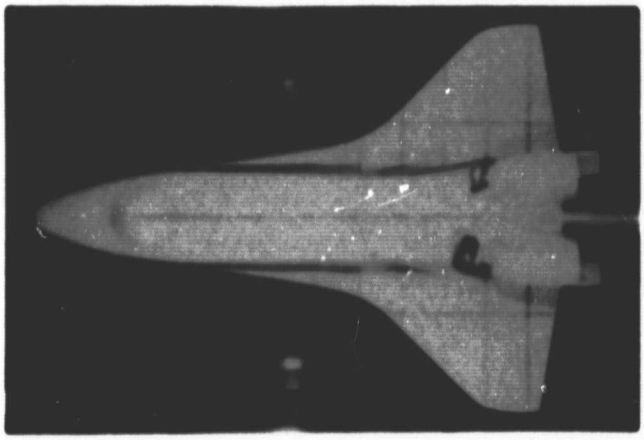

$\alpha = -2^{o}$

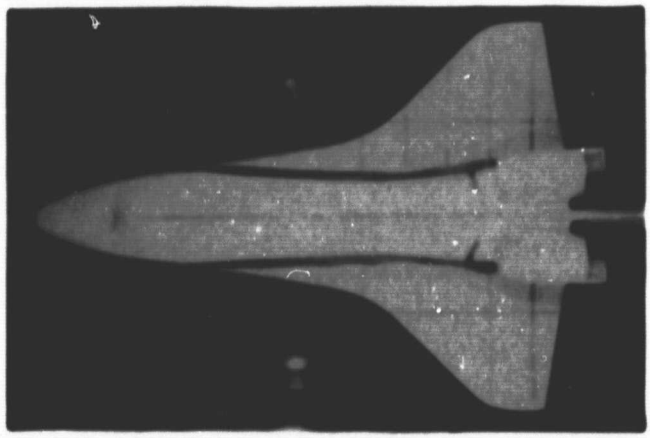

$\alpha = 0^{o}$

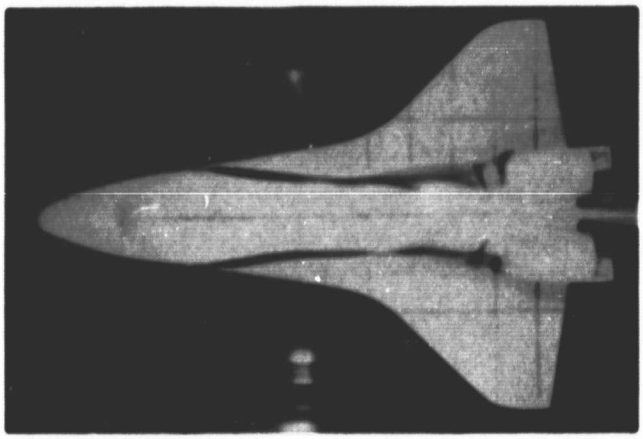

$\alpha = 2^{o}$

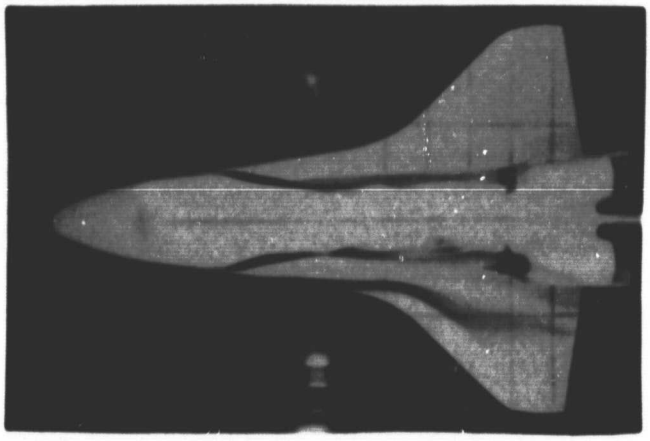

$\alpha = 5^{o}$

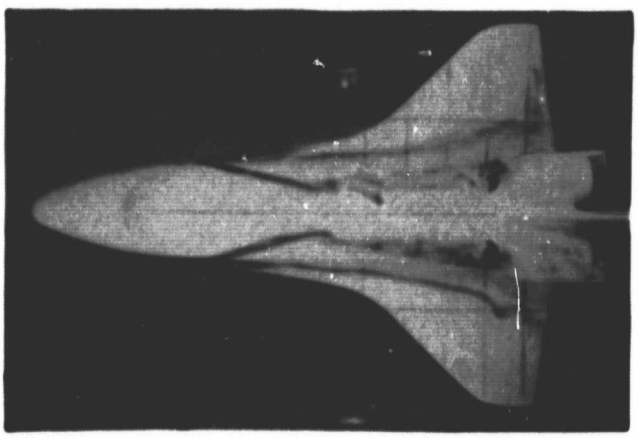

$\alpha = 10^{o}$

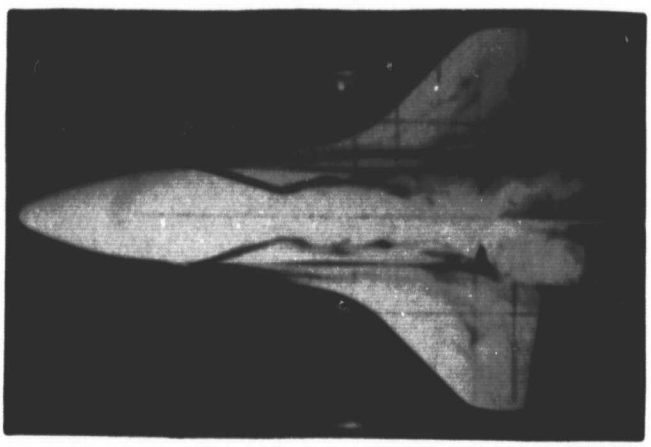

$\alpha = 12^{o}$

(A) PLAN VIEW

FIGURE 13. FUSELAGE FLOW FIELD FOR $\beta = 0^{o}$

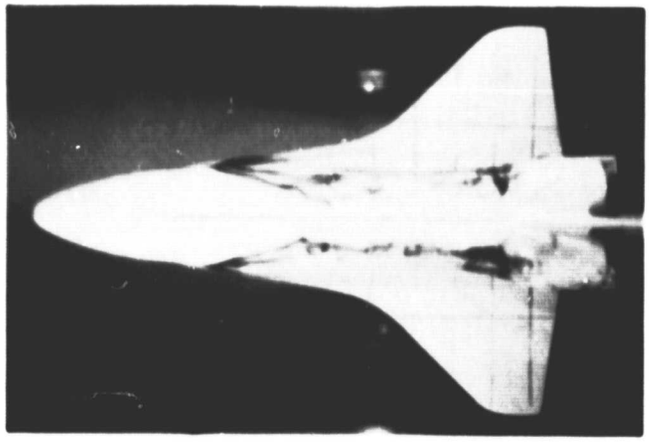

$\alpha = 15°$

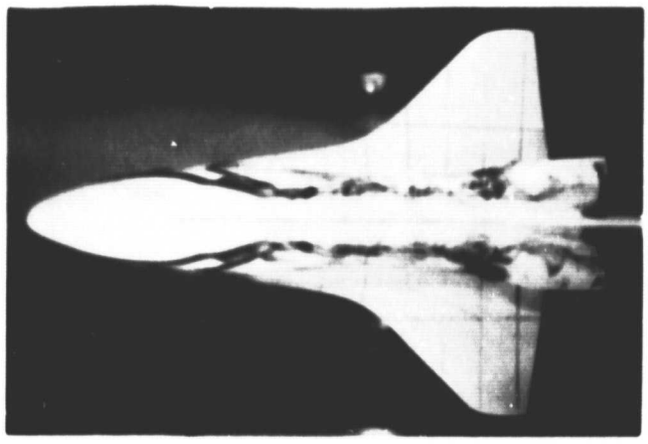

$\alpha = 20°$

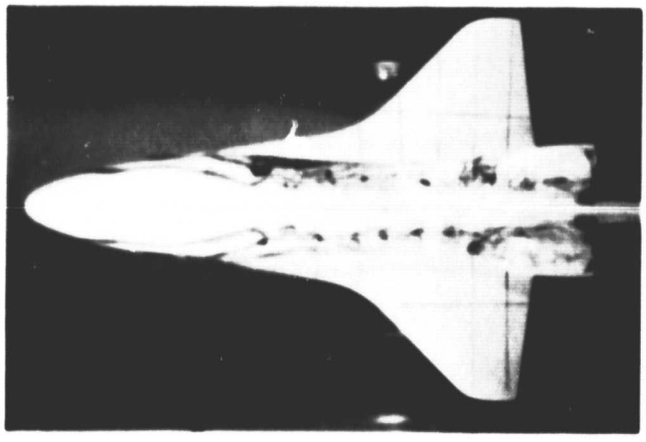

$\alpha = 25°$

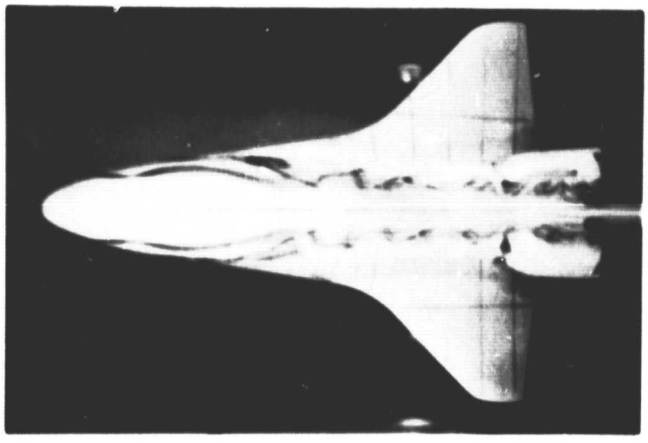

$\alpha = 30°$

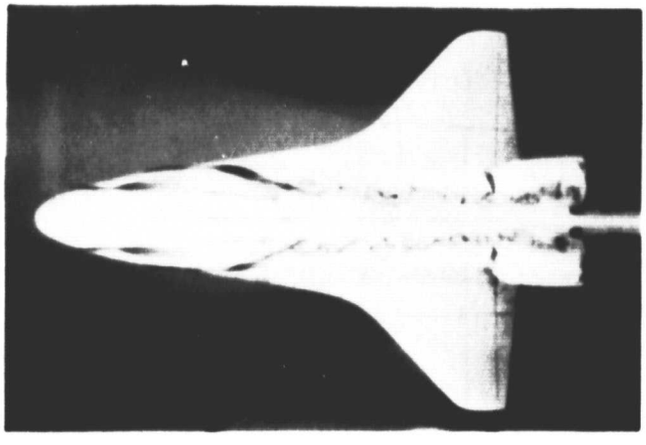

$\alpha = 35°$

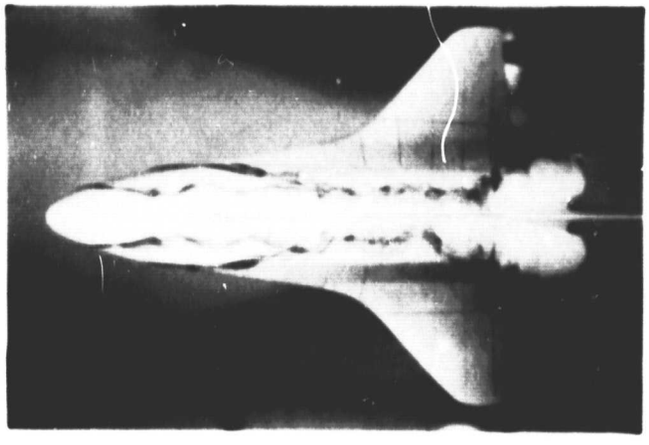

$\alpha = 40°$

(a) PLAN VIEW, $\beta = 0°$

FIGURE 12. LEESIDE FLOW FIELD FOR $\beta = 0°$ (CONCLUDED)

ORIGINAL PAGE IS
OF POOR QUALITY

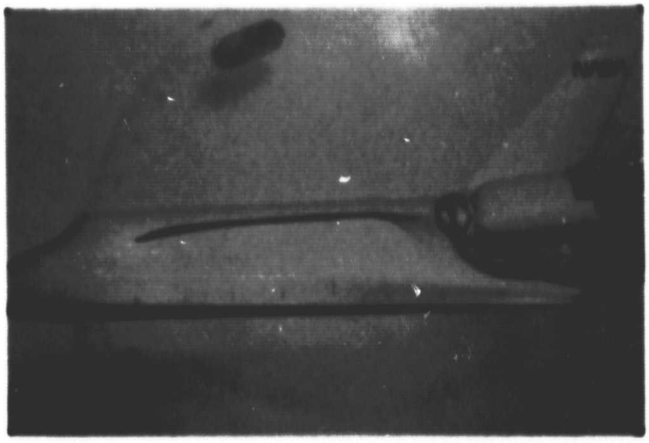

$\alpha = -2^{o}$

$\alpha = 0^{o}$

$\alpha = 2^{o}$

$\alpha = 5^{o}$

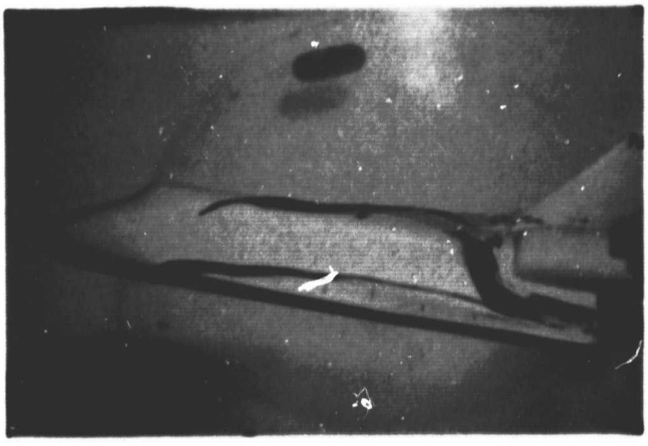

$\alpha = 10^{o}$

$\alpha = 12^{o}$

(B) PROFILE VIEW, $\beta = 0^{o}$

FIGURE 13. FUSELAGE FLOW FIELD FOR $\beta = 0^{o}$ (Continued)

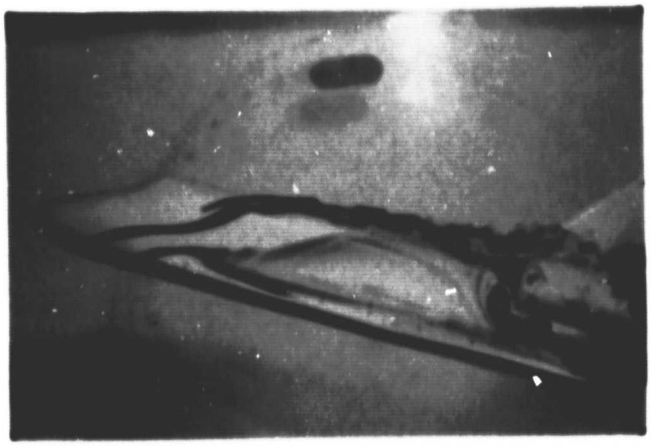

$\alpha = 15^{\circ}$

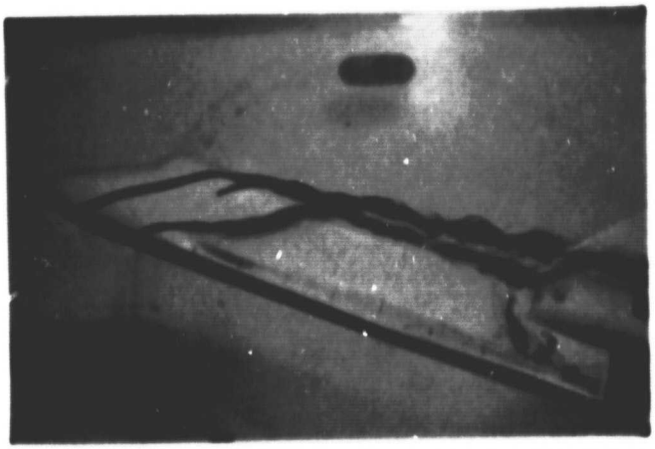

$\alpha = 20^{\circ}$

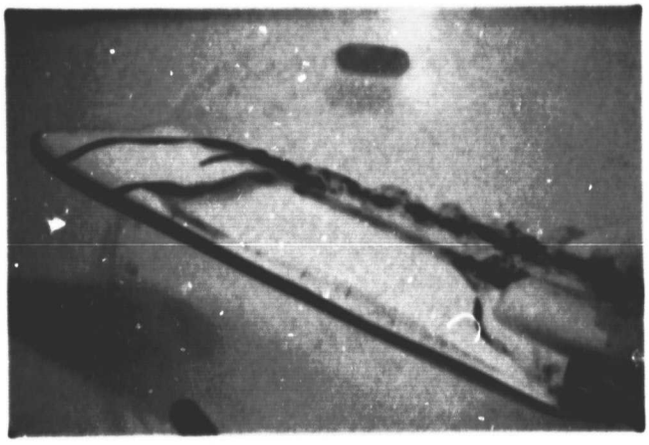

$\alpha = 25^{\circ}$

$\alpha = 30^{\circ}$

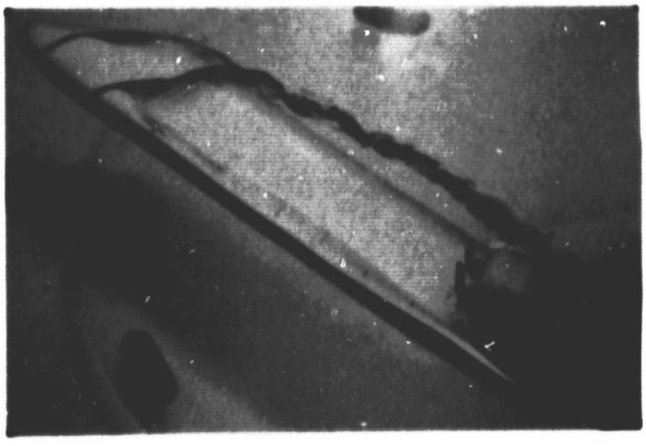

$\alpha = 35^{\circ}$

$\alpha = 40^{\circ}$

(B) PROFILE VIEW, $\beta = 0^{\circ}$

FIGURE 13. FUSELAGE FLOW FIELD FOR $\beta = 0^{\circ}$ (Concluded)

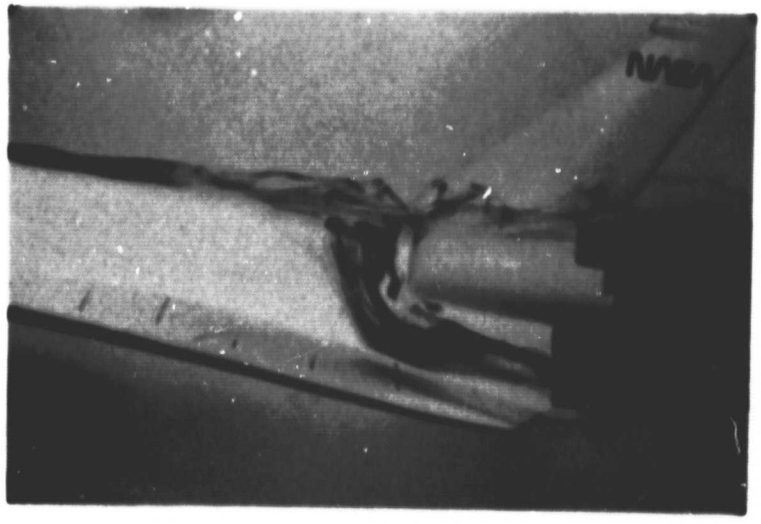

$\alpha = 10^{\circ}$

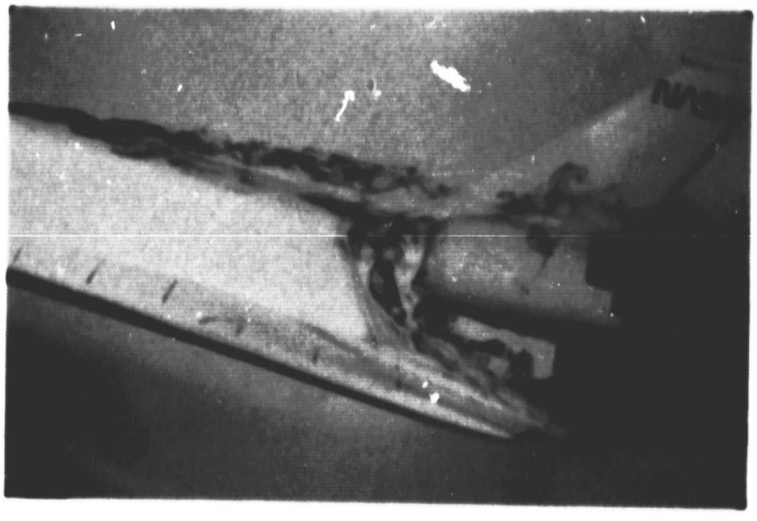

$\alpha = 15^{\circ}$

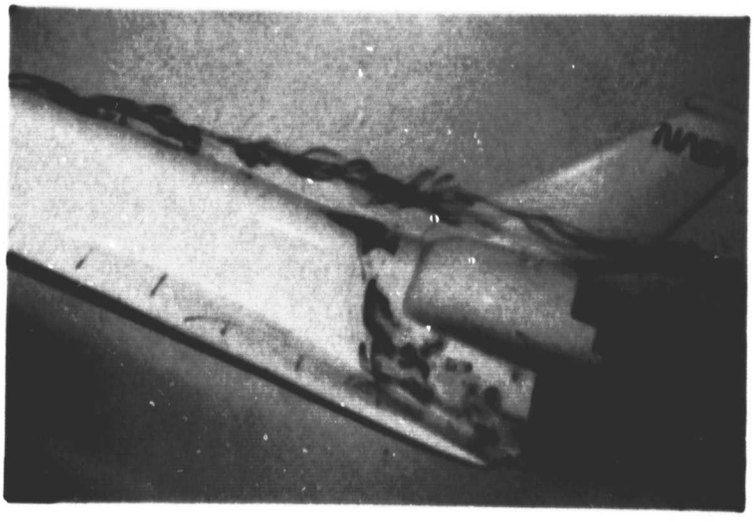

$\alpha = 20^{\circ}$

FIGURE 14. AFT FUSELAGE FLOW FIELD FOR $\beta = 0^{\circ}$

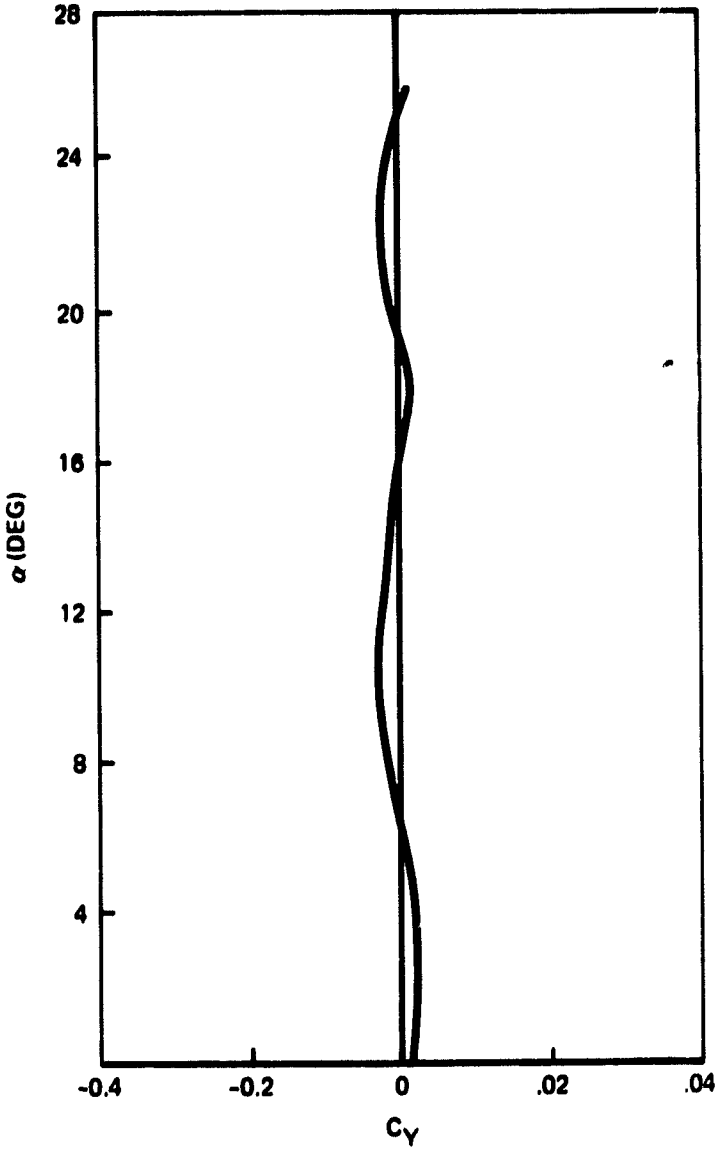

FIGURE 15. SIDE FORCE ON ORBITER AT ZERO SIDESLIP

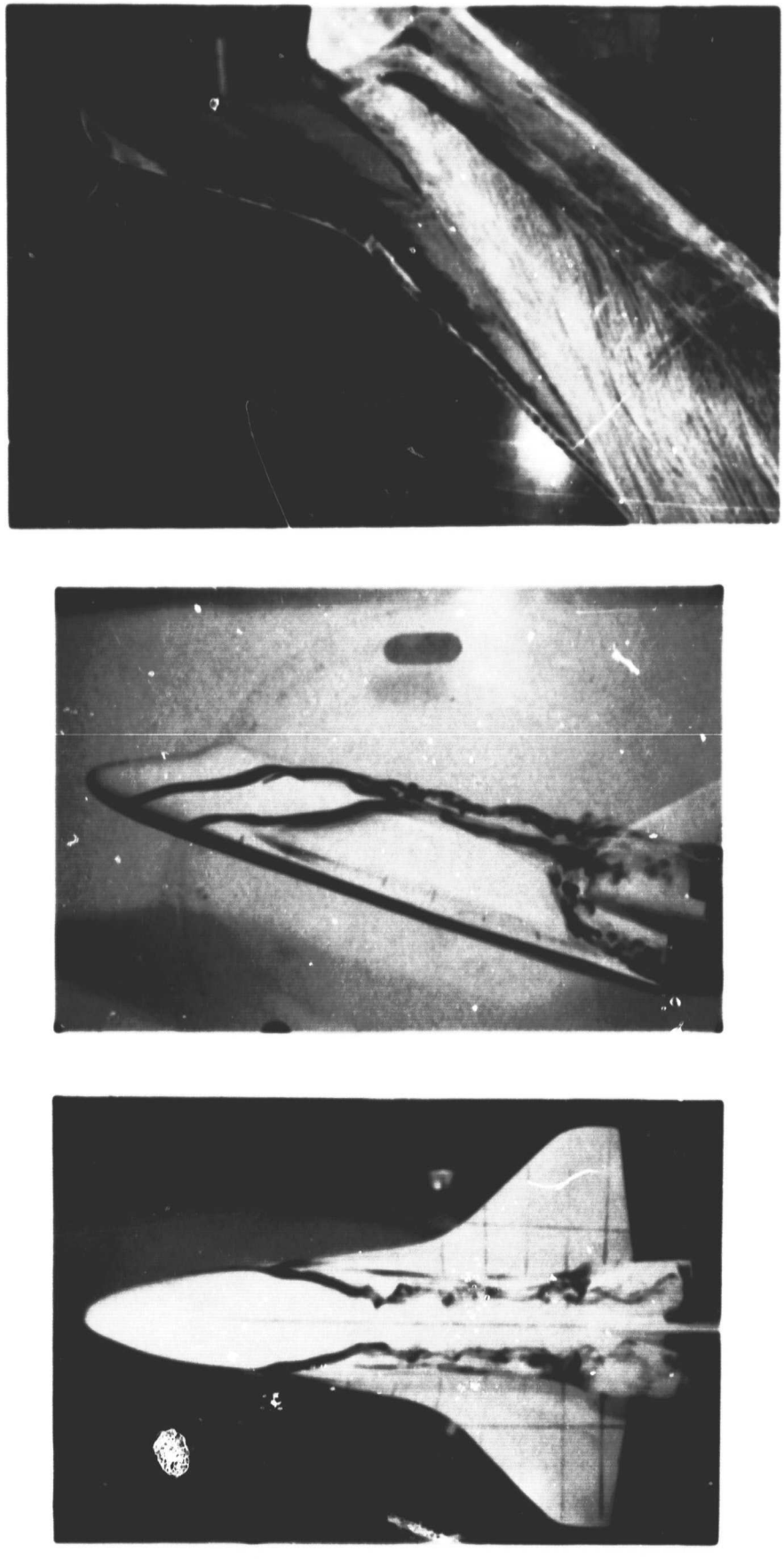

FIGURE 16. COMPARISON OF WIND TUNNEL OIL FLOW VISUALIZATION WITH WATER TUNNEL FLOW VISUALIZATION, $\alpha = 18°$, $\beta = 0°$

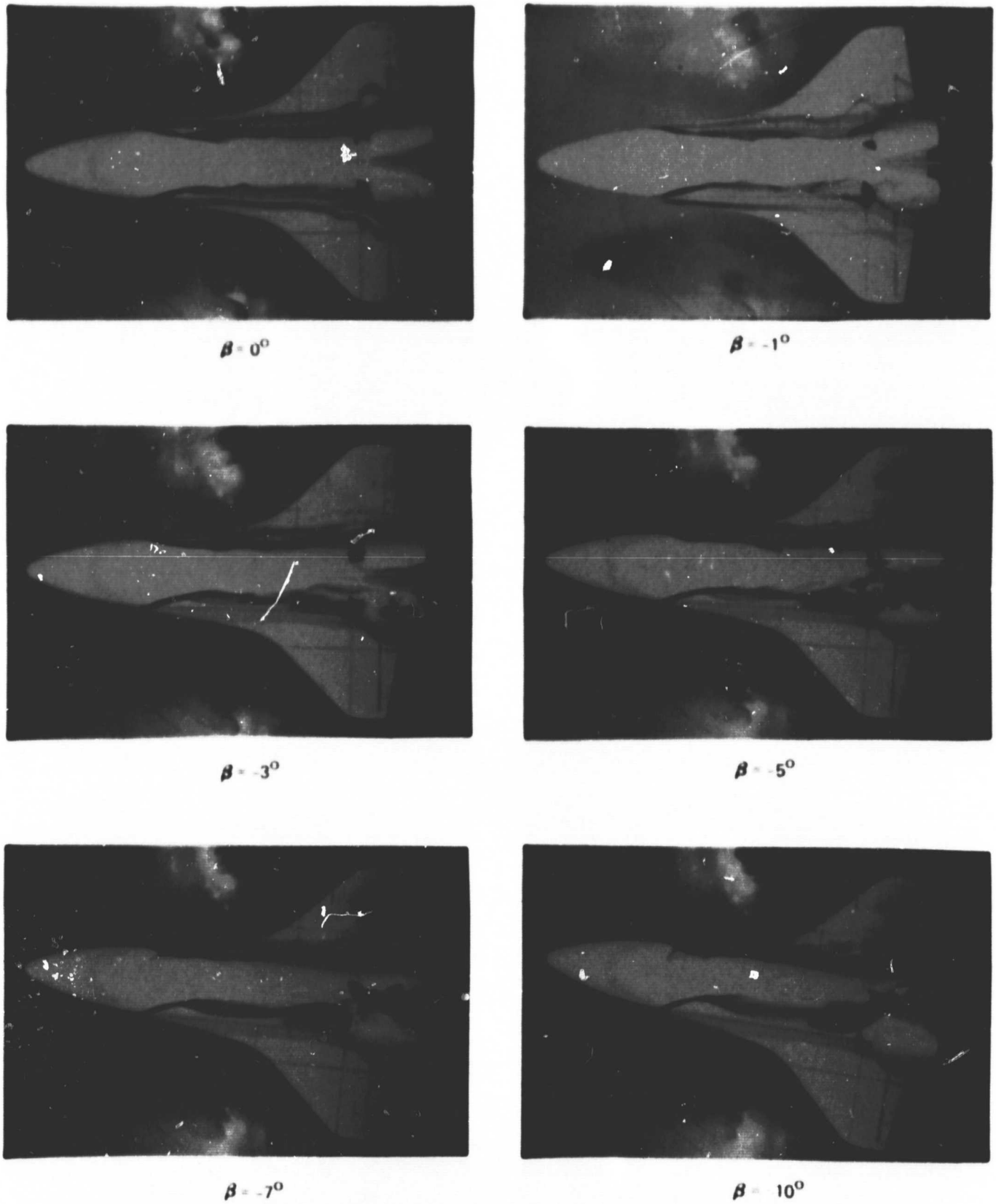

(A) PLAN VIEW

FIGURE 17. FUSELAGE FLOW FIELD IN SIDESLIP FOR $\alpha = 8°$

ORIGINAL PAGE IS
OF POOR QUALITY

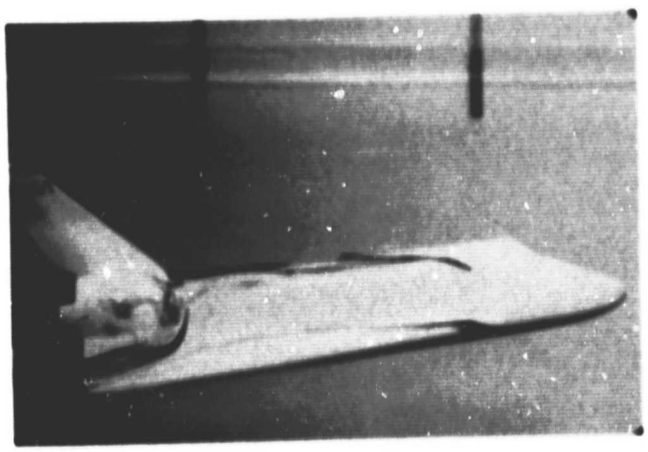

$\beta = 0^{\circ}$

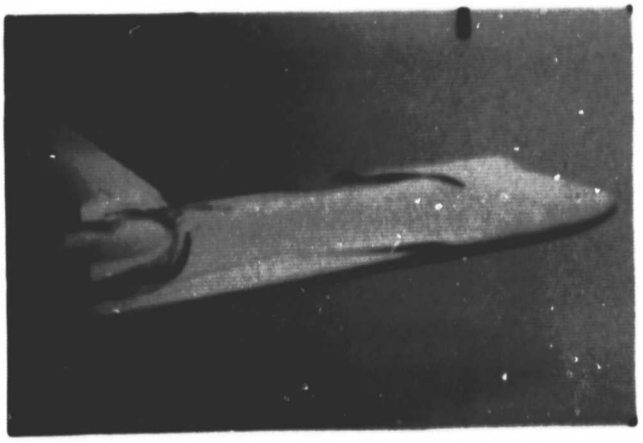

$\beta = 1^{\circ}$

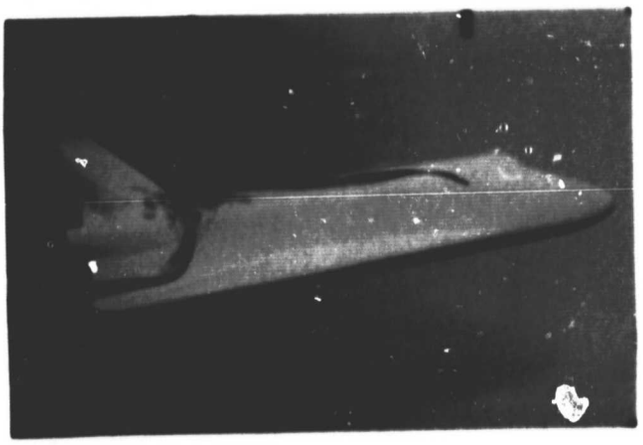

$\beta = 3^{\circ}$

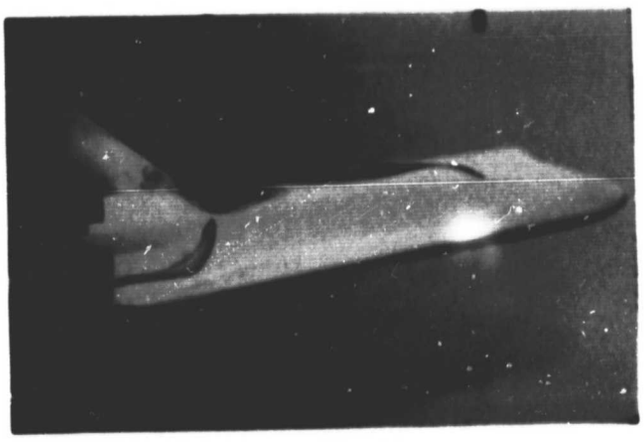

$\beta = 5^{\circ}$

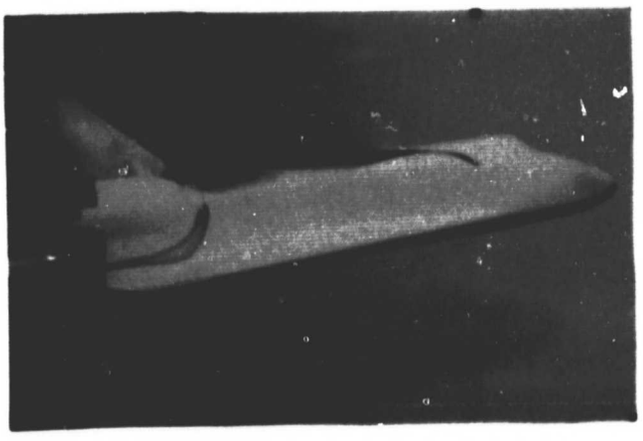

$\beta = 7^{\circ}$

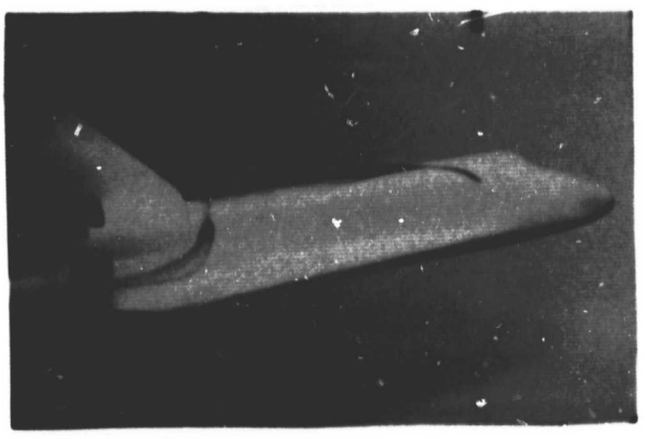

$\beta = 10^{\circ}$

(B) WINDWARD PROFILE VIEW, $\alpha = 8^{\circ}$

FIGURE 17. FUSELAGE FLOW FIELD IN SIDESLIP FOR $\alpha = 8^{\circ}$ (Continued)

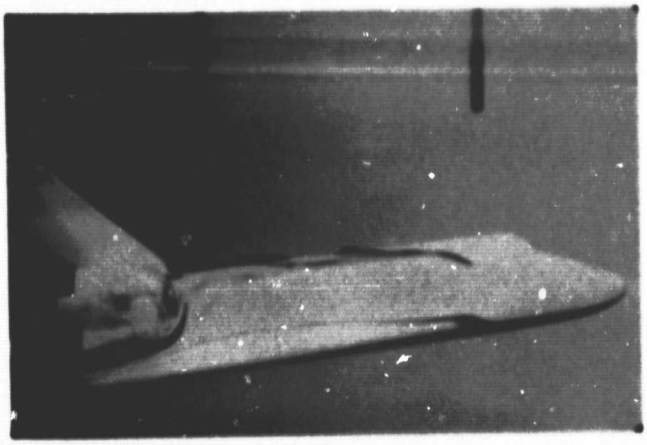

$\beta = 0^{\circ}$

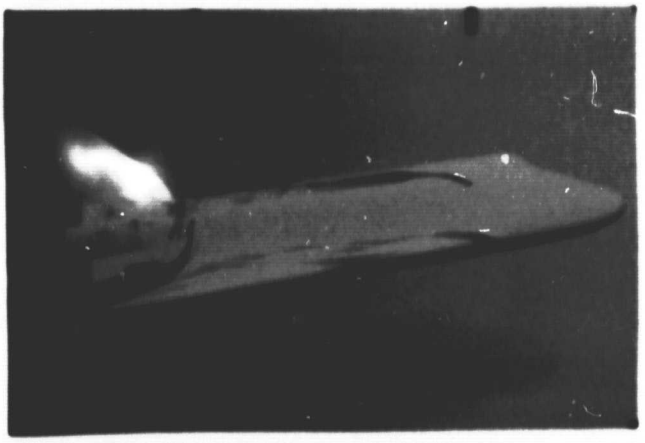

$\beta = -1^{\circ}$

$\beta = -3^{\circ}$

$\beta = -5^{\circ}$

$\beta = -7^{\circ}$

$\beta = -10^{\circ}$

(C) LEEWARD PROFILE VIEW, $\alpha = 8^{\circ}$

FIGURE 17. FUSELAGE FLOW FIELD IN SIDESLIP FOR $\alpha = 8^{\circ}$ (Concluded)

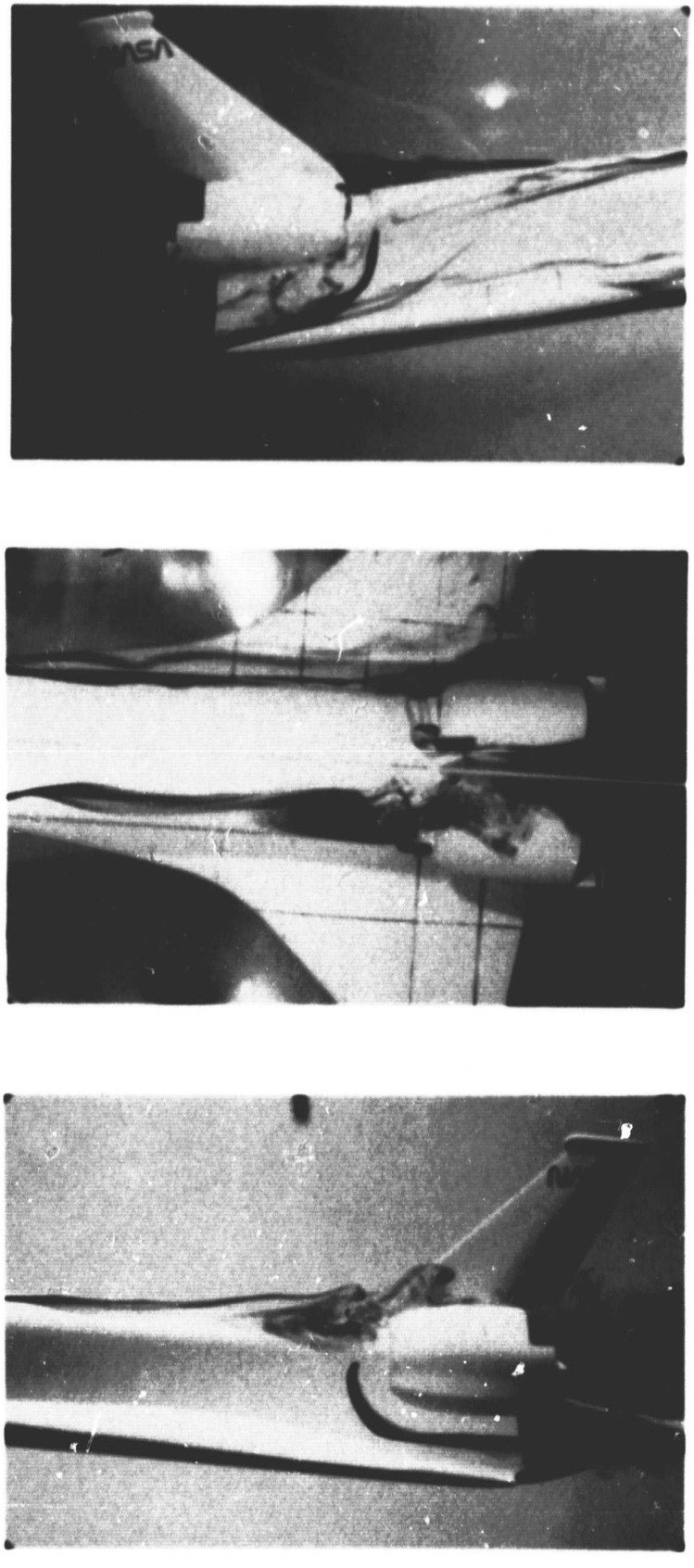

ORIGINAL PAGE IS
OF POOR QUALITY

FIGURE 18. AFT FUSELAGE FLOW FIELD IN SIDESLIP FOR $\alpha = 8°$, $\beta = 5°$

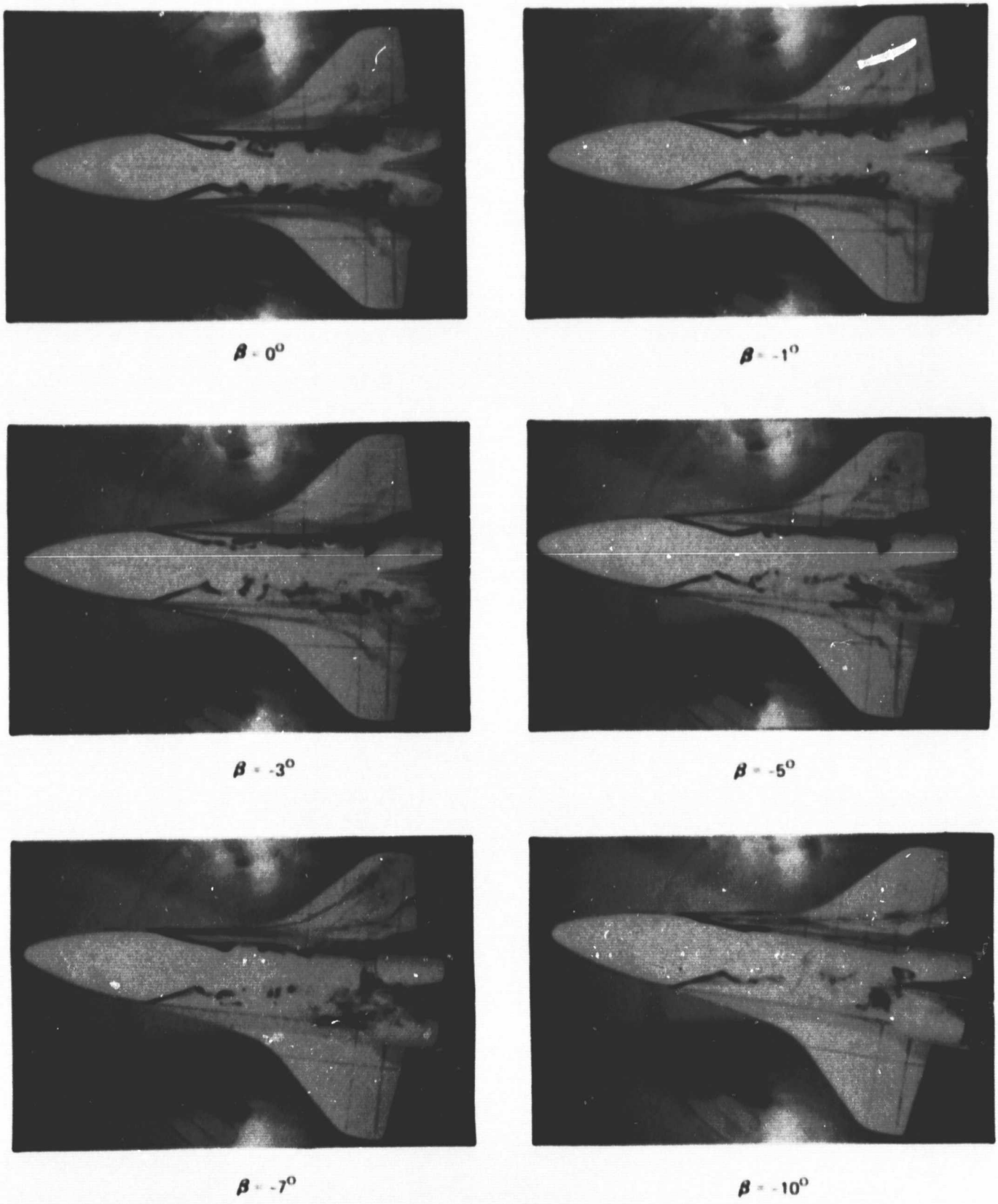

(A) PLAN VIEW

FIGURE 19. FUSELAGE FLOW FIELD IN SIDESLIP FOR $\alpha = 15°$

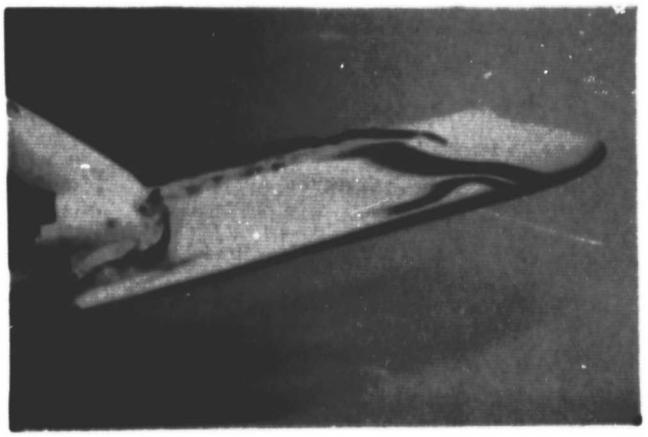

$\beta = 0^{o}$

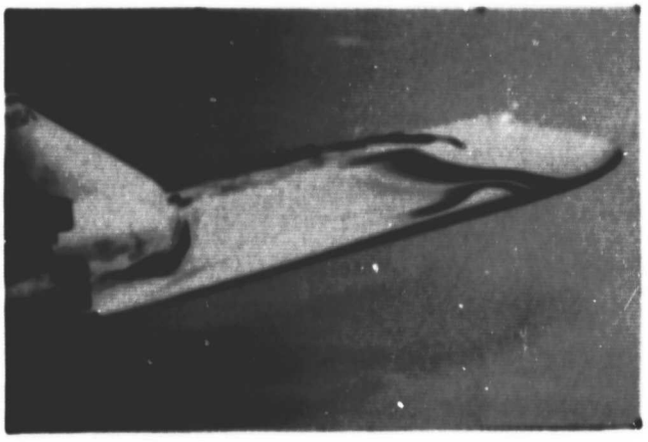

$\beta = 1^{o}$

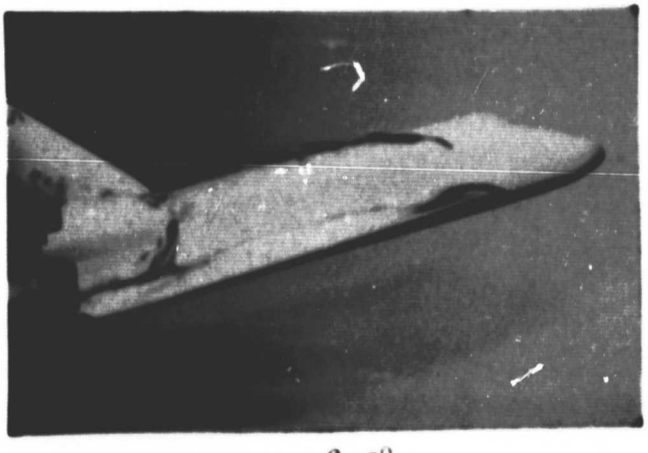

$\beta = 3^{o}$

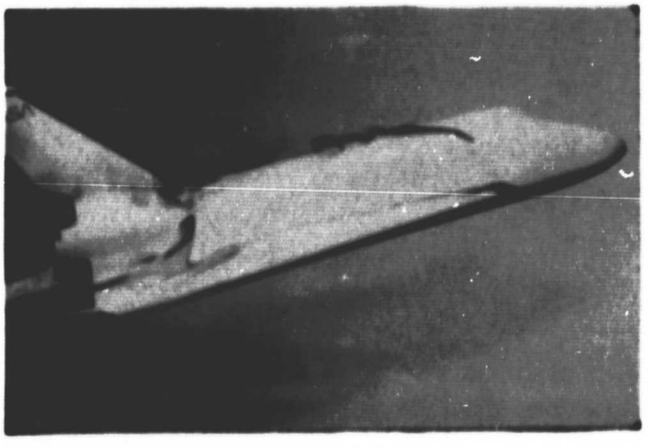

$\beta = 5^{o}$

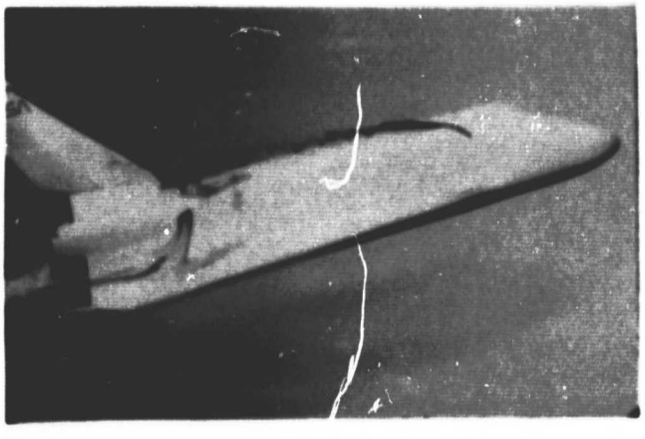

$\beta = 7^{o}$

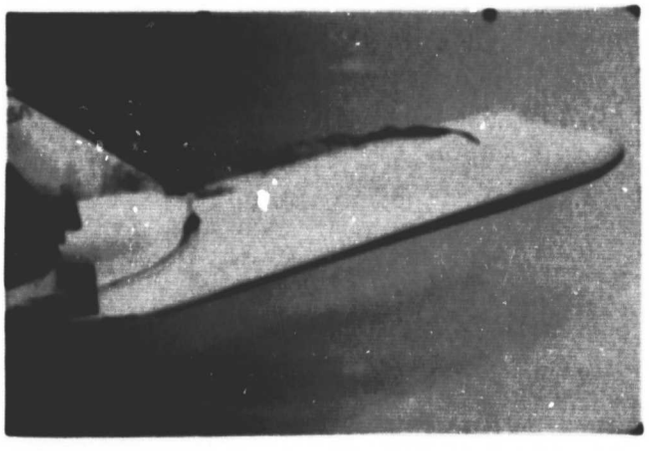

$\beta = 10^{o}$

(B) WINDWARD PROFILE VIEW, $\alpha = 15^{o}$

FIGURE 19. FUSELAGE FLOW FIELD IN SIDESLIP FOR $\alpha = 15^{o}$ (Continued)

ORIGINAL PAGE IS
OF POOR QUALITY

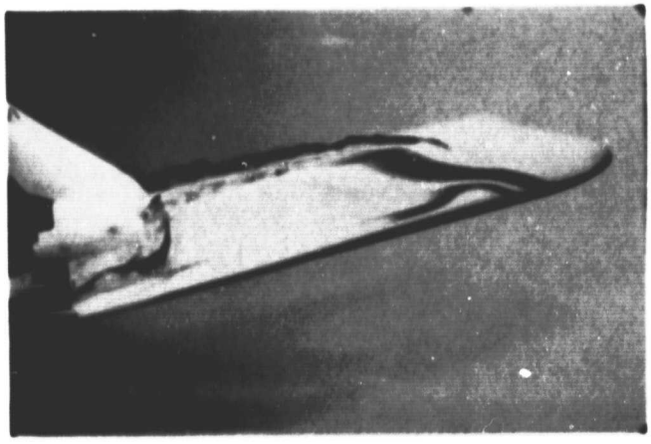

β 0°

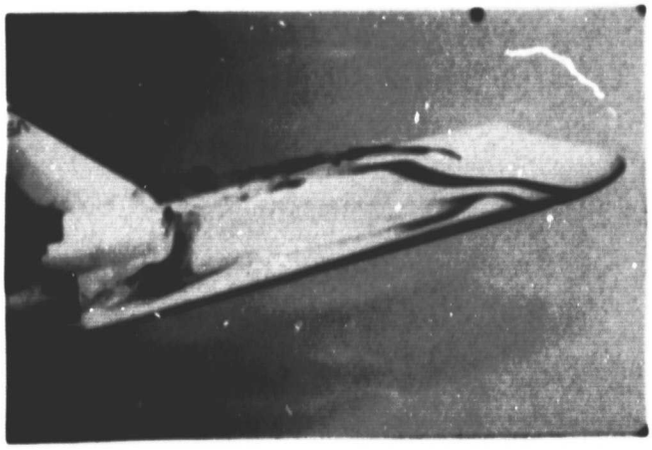

β -1°

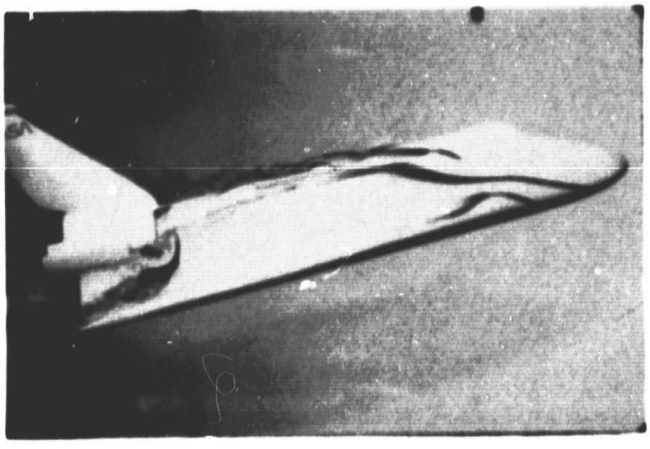

β -3°

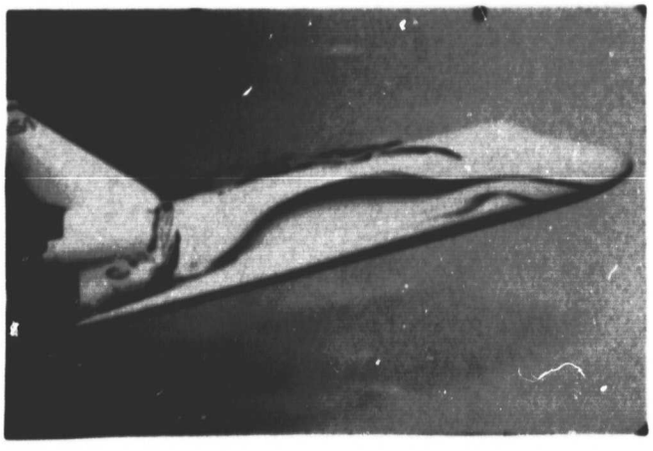

β -5°

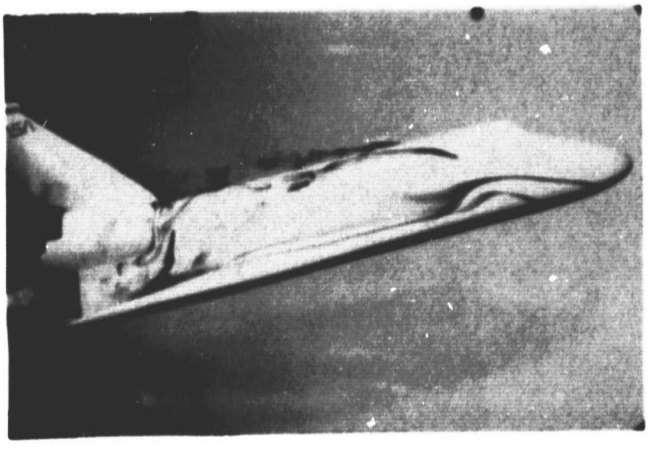

β -7°

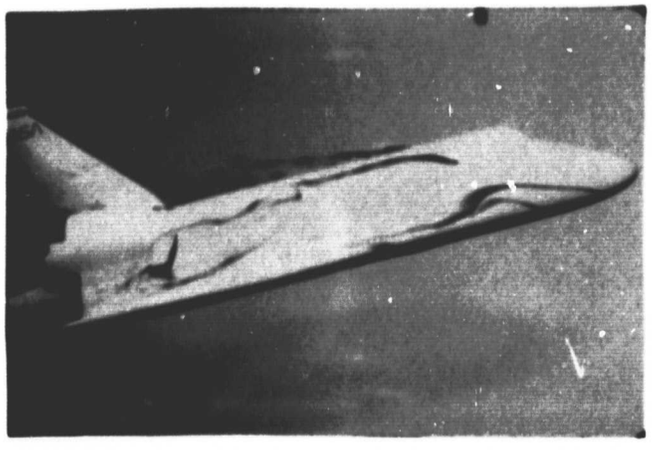

β -10°

(c) LEEWARD PROFILE VIEW, $\alpha = 15°$

FIGURE 19. FUSELAGE FLOW FIELD IN SIDESLIP FOR $\alpha = 15°$ (Concluded)

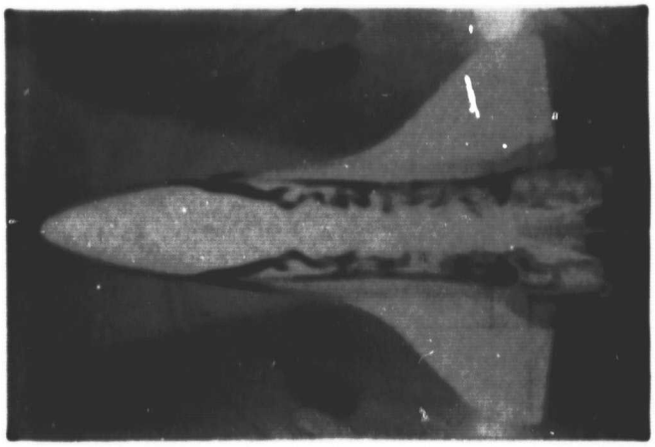

$\beta = 0^{o}$

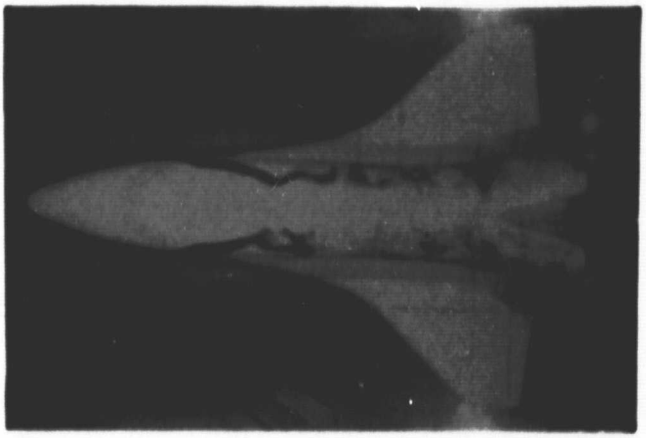

$\beta = -1^{o}$

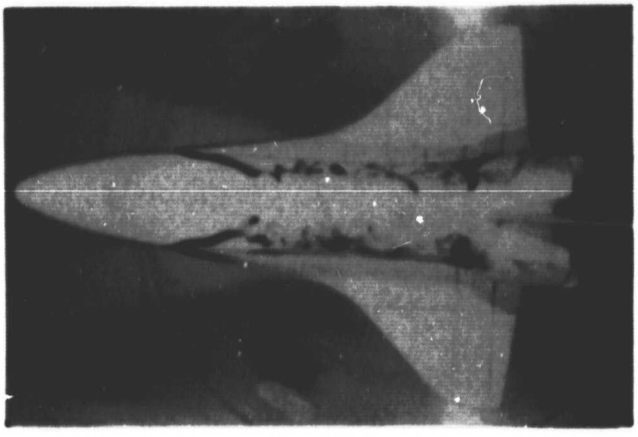

$\beta = -3^{o}$

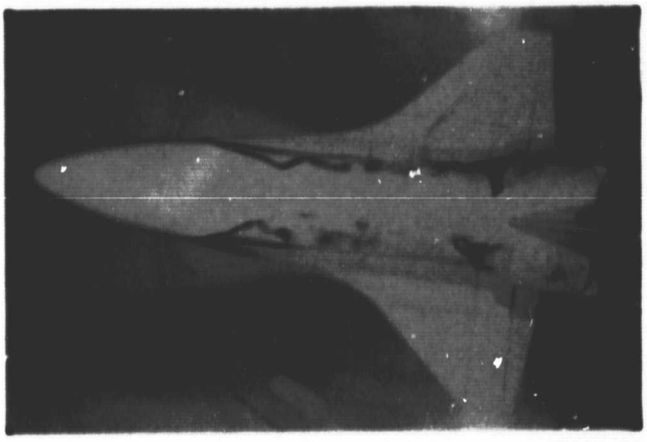

$\beta = -5^{o}$

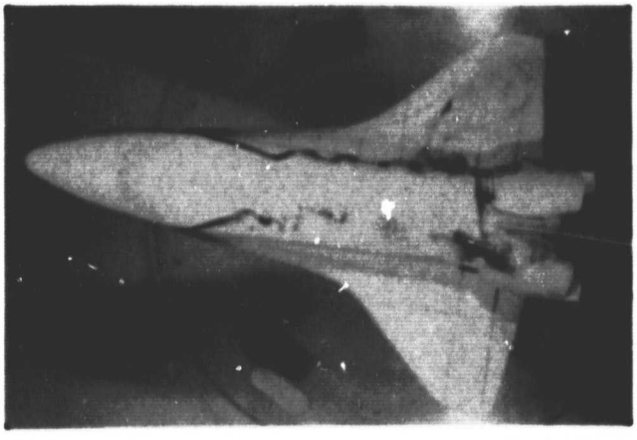

$\beta = -7^{o}$

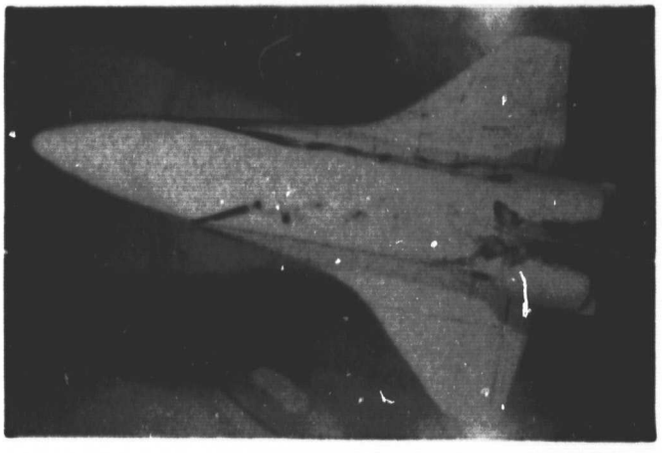

$\beta = -10^{o}$

(A) PLAN VIEW

FIGURE 20. FUSELAGE FLOW FIELD IN SIDESLIP FOR $\alpha = 20^{o}$

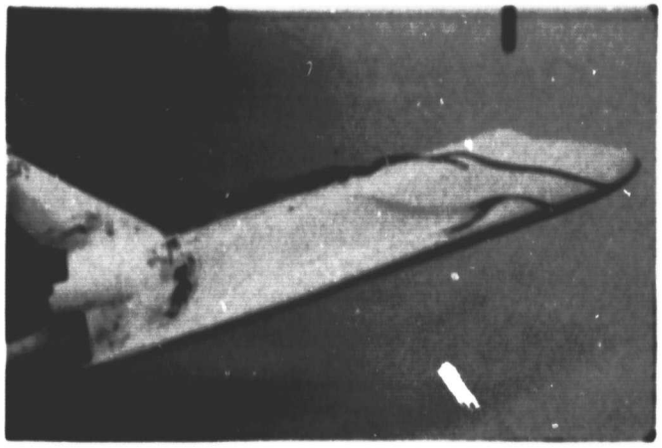

$\beta = 0^{\circ}$

$\beta = 1^{\circ}$

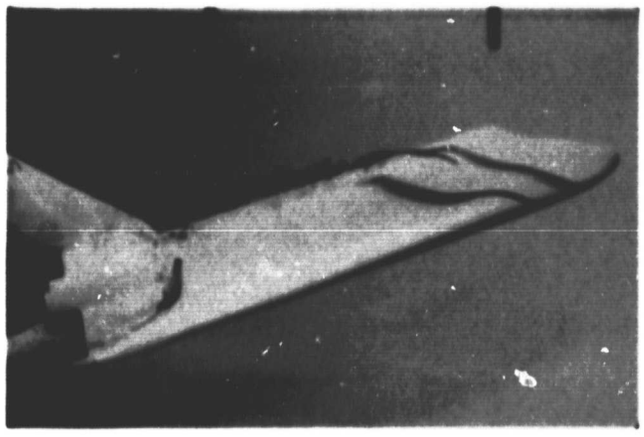

$\beta = 3^{\circ}$

$\beta = 5^{\circ}$

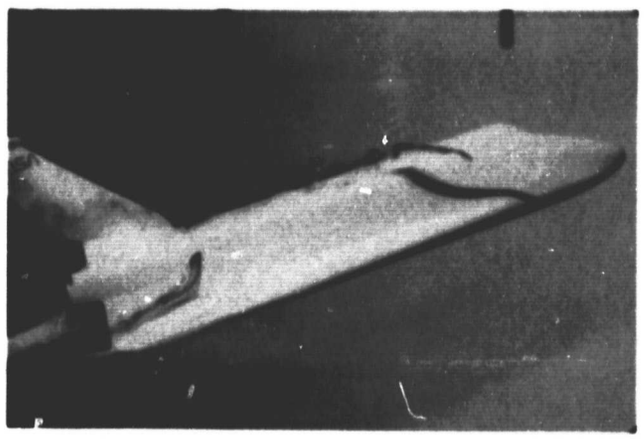

$\beta = 7^{\circ}$

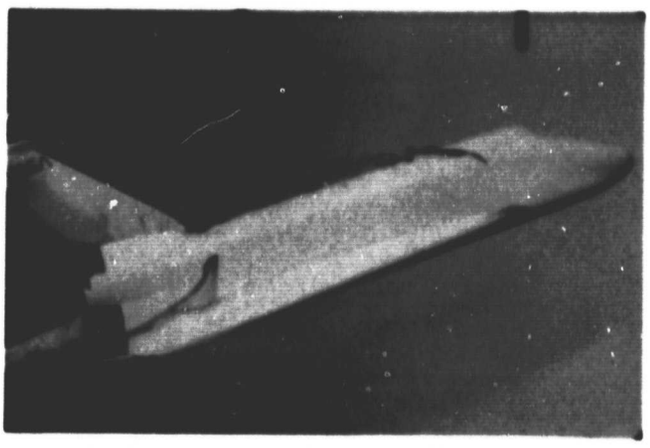

$\beta = 10^{\circ}$

(B) WINDWARD PROFILE VIEW, $\alpha = 20^{\circ}$

FIGURE 20. FUSELAGE FLOW FIELD IN SIDESLIP FOR $\alpha = 20^{\circ}$ (Continued)

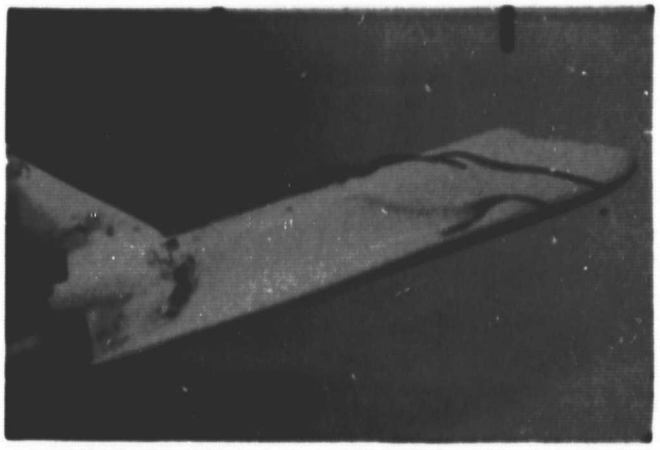

$\beta = 0^{o}$

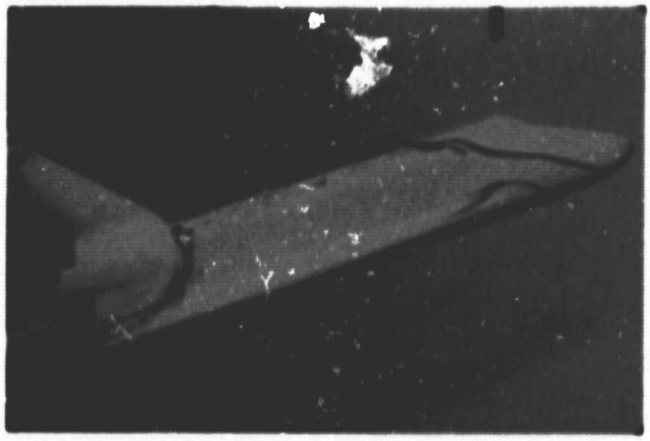

$\beta = -1^{o}$

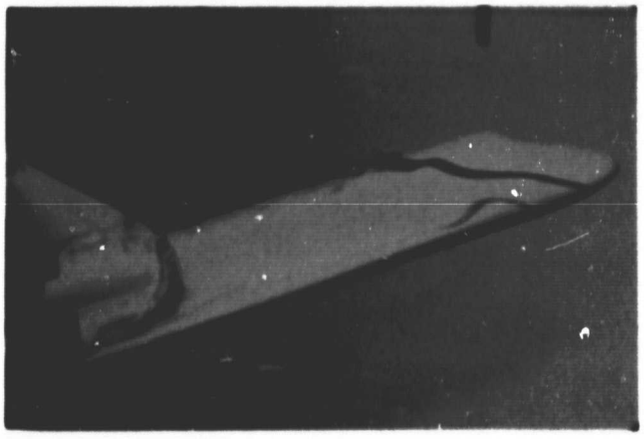

$\beta = -3^{o}$

$\beta = -5^{o}$

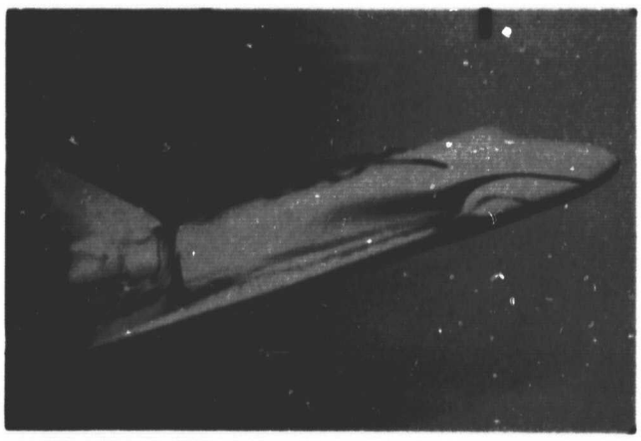

$\beta = -7^{o}$

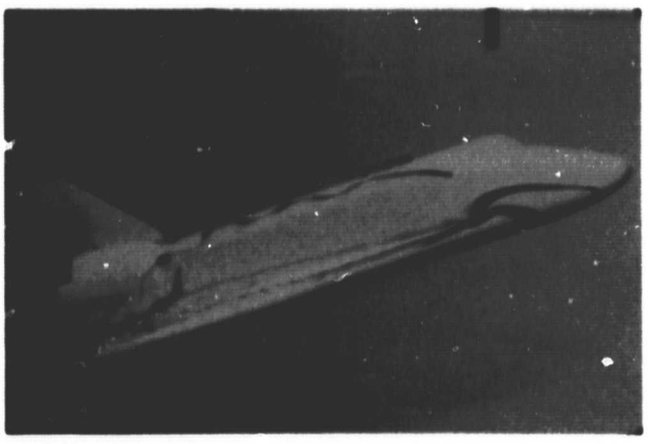

$\beta = -10^{o}$

(C) LEEWARD PROFILE VIEW, $\alpha = 20^{o}$

FIGURE 20. FUSELAGE FLOW FIELD IN SIDESLIP FOR $\alpha = 20^{o}$ (Concluded)

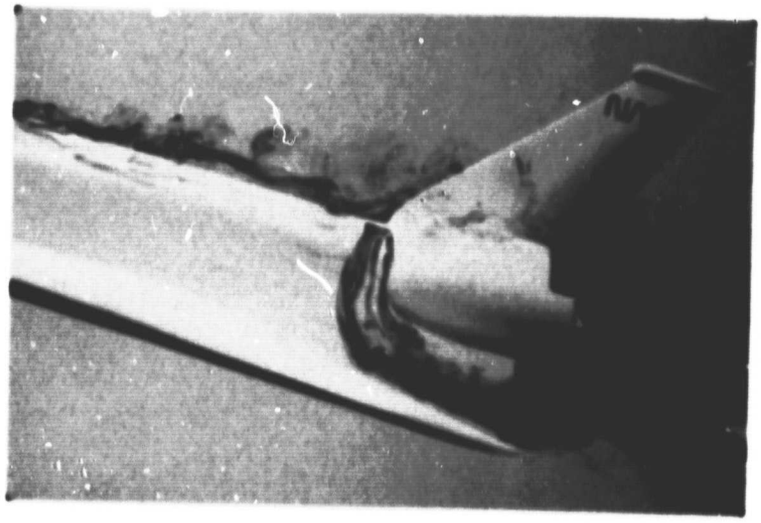

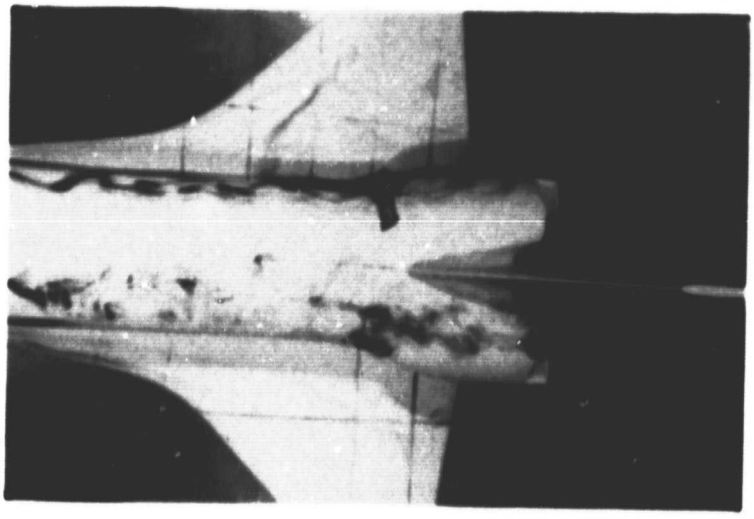

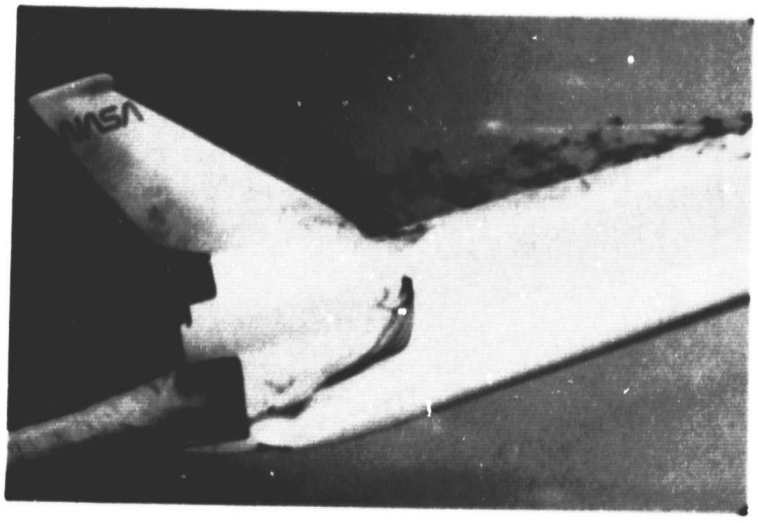

ORIGINAL PAGE IS
OF POOR QUALITY

FIGURE 21. AFT FUSELAGE FLOW FIELD IN SIDESLIP FOR $\alpha = 20°$, $\beta = 5°$

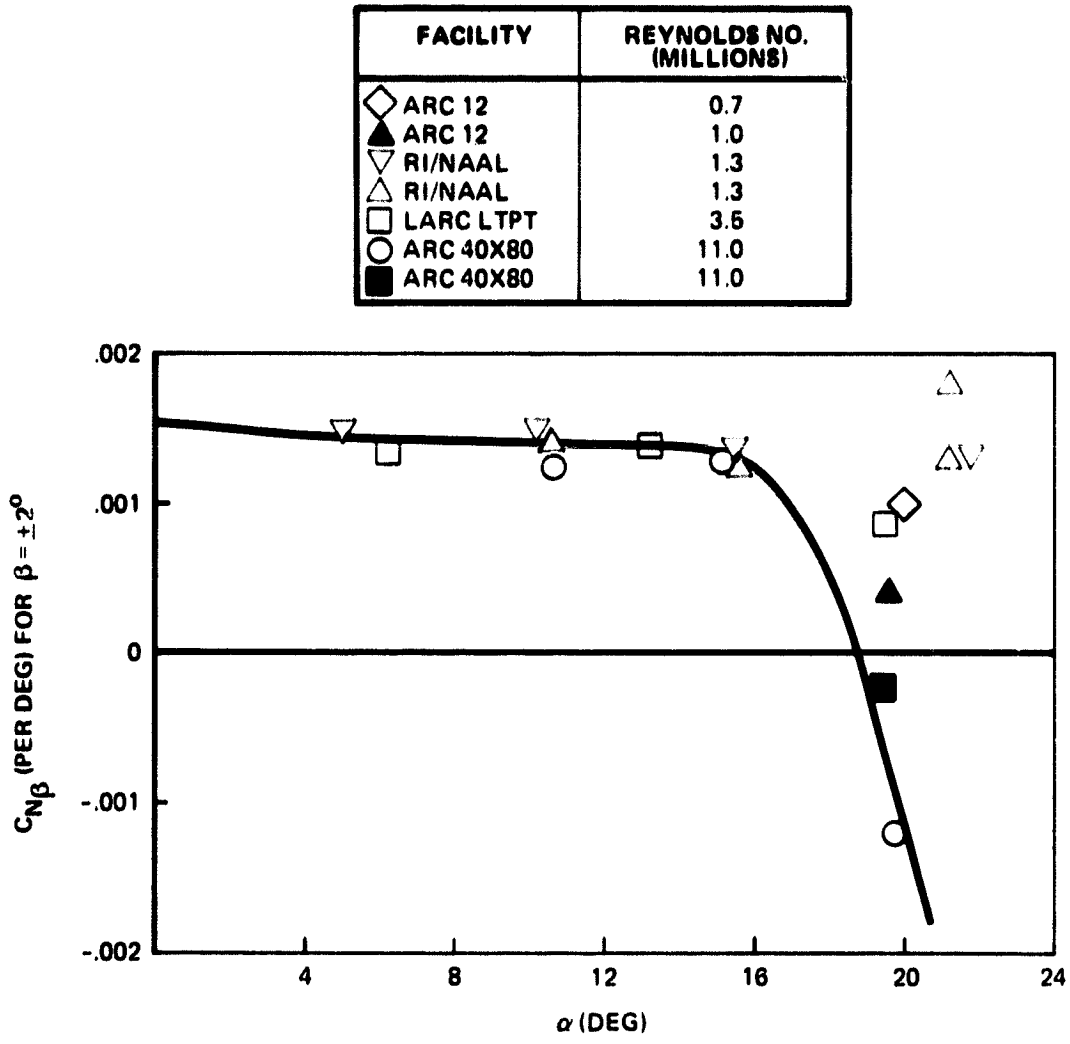

FIGURE 22. EFFECT OF REYNOLDS NUMBER AND DIFFERENT FACILITIES ON DIRECTIONAL STABILITY (REYNOLDS NUMBER BASED ON FUSELAGE WIDTH OF THE ORBITER)